



저작자표시-비영리-동일조건변경허락 2.0 대한민국

이용자는 아래의 조건을 따르는 경우에 한하여 자유롭게

- 이 저작물을 복제, 배포, 전송, 전시, 공연 및 방송할 수 있습니다.
- 이차적 저작물을 작성할 수 있습니다.

다음과 같은 조건을 따라야 합니다:



저작자표시. 귀하는 원저작자를 표시하여야 합니다.



비영리. 귀하는 이 저작물을 영리 목적으로 이용할 수 없습니다.



동일조건변경허락. 귀하가 이 저작물을 개작, 변형 또는 가공했을 경우에는, 이 저작물과 동일한 이용허락조건하에서만 배포할 수 있습니다.

- 귀하는, 이 저작물의 재이용이나 배포의 경우, 이 저작물에 적용된 이용허락조건을 명확하게 나타내어야 합니다.
- 저작권자로부터 별도의 허가를 받으면 이러한 조건들은 적용되지 않습니다.

저작권법에 따른 이용자의 권리는 위의 내용에 의하여 영향을 받지 않습니다.

이것은 [이용허락규약\(Legal Code\)](#)을 이해하기 쉽게 요약한 것입니다.

[Disclaimer](#)

이학박사학위논문

Spectroscopic and Microscopic Studies on Biomolecules and Optoelectronic Devices

분광학과 현미경을 이용한 생분자 및 광전소자 연구

2018 년 2 월

서울대학교 대학원
화학부 물리화학 전공
강 주 연

Ph.D. Dissertation

Spectroscopic and Microscopic Studies on Biomolecules and Optoelectronic Devices

Jooyoun Kang

Research Advisor: Professor Seong Keun Kim

Department of Chemistry
Seoul National University

Abstract

Jooyoun Kang

Major in Physical Chemistry

Department Chemistry

Seoul National University

The interaction of electromagnetic radiation and matter arouses a variety of scientific interests. Spectroscopy, the study of detecting and analyzing changes in light by light-matter interaction, has played a central role in the development of quantum mechanics and is still being used for physical and chemical analysis. Optical microscopy that spatially visualizes signals from light-matter interaction provides direct information on the structure and chemical composition of objects. We can observe living species *in situ* noninvasively using an optical spectrometer or microscope. During my Ph.D. course, I tried to solve some biological and optoelectronic questions using optical techniques.

A far-field optical microscope cannot distinguish two objects in close proximity because of the inherent diffraction limit of light. Recent developments of super-resolution microscopy that overcome the diffraction limit by using the photophysical properties of fluorophores enable us to observe small objects such as organelles, proteins, and DNA in living cells. The precise location of intracellular proteins was confirmed using a stimulated emission depletion (STED) microscope, one of the super-resolution microscopes. Leucyl-tRNA synthetase (LRS) plays a major role in providing leucine-tRNA and activating the mechanistic target of rapamycin complex 1 (mTORC1) through intracellular leucine

sensing. mTORC1 influences physiological functions including cell proliferation, protein synthesis, and autophagy. Using a STED microscope, we verified the hypothesis that LRS is translocated to the lysosome membrane by the addition of leucine. This direct visualization proves the function of LRS as an intracellular leucine sensor and positive regulator of amino-acid signaling to mTORC1.

Since biomolecules exist in heterogeneous environments, it is necessary to observe the state of each molecule. Single-molecule spectroscopy enables us to observe single molecules without ensemble averaging. Here, we demonstrate that single-molecule fluorescence resonance energy transfer (FRET) spectroscopy can be used to probe the flexibility of a single-stranded DNA (ssDNA). ssDNA is crucial for understanding the biological machinery in a cell nucleus but understanding its characterization has been difficult because of the dynamically changing structure of ssDNA in nanometer scale. We designed a double-stranded DNA system with various lengths of single-strand overhang and determined the flexibility of the single-stranded segment by measuring the FRET value. We found that three of our ssDNAs with lengths shorter than the persistence length were long enough to undergo folding. We also found that there is no significant effect of charge screening by metal ion when the ssDNA is less than 9 bases in length.

Even in single-molecule detection based on a confocal microscope, the concentration should be lower than 50 pM to observe single molecules due to the diffraction limit. Intracellular biomolecules such as enzymes work at levels 100 times higher (5 nM). With the combination of STED microscopy and single-molecule FRET spectroscopy, we break the concentration barrier in diffusion-based single molecule spectroscopy. We were able to detect single molecules diffusing in a tightly confined volume 100 times smaller than the diffraction-limited confocal volume. The feasibility of this new technique was demonstrated

using the dual-labelled dsDNA molecule. With this new technique, we showed that single-molecule detection is possible at concentrations up to 5 nM.

We applied the spectroscopic techniques to optoelectronic devices as well as biomolecules. In particular, the degradation mechanism of organic light emitting diodes (OLEDs) was investigated by time-resolved spectroscopy. It is important to understand the detailed mechanism of the degradation of OLEDs to improve device stability and performance. During the degradation, charge carriers are confined in chemical defect sites called charge traps. The charge traps, which degrade device performance, are difficult to experimentally observe. Transient electroluminescence (TREL) is capable of observing the charge traps and elucidating the effect of the charge traps on OLED luminescence. Onset time (t_0), the time between the first application of operating voltage and light emission, decreases as the device undergoes degradation. The charge carriers trapped inside the organic layer encounter each other earlier than the charge carriers generated from the electrodes. Decay time (t_d), the luminescence lifetime, increases during degradation, which can be explained by the delayed recombination of the charge traps. The decrease of t_0 and the increase of t_d confirms the presence of the charge traps and their effect on luminescence. Spectroscopic TREL measurement enables the investigation of the charge traps *in situ* and is universally use for studying the device degradation mechanism and understanding its properties.

Chemical analysis of the degraded OLED device is needed to examine which specific layer in the OLED device is degraded. Unlike other chemical analysis techniques, optical spectroscopy enables non-invasive analysis of the photochemical properties through luminescence intensity and lifetime analysis. However, the thickness of each layer is about tens of nanometers and therefore cannot be optically resolved because of the diffraction limit. A specially de-

signed device consisting of layers with different bandgaps was used so that each layer emitted light of a different wavelength. The layers could not be resolved spatially but could be resolved spectrally. We observed spectroscopically the behavior of three materials in the device during the degradation process. This simple optical technique for layer selective characterization will be very useful in the study of various multi-layer devices.

Keywords: Photophysics, Super-resolution STED microscopy, Single-molecule FRET spectroscopy, Time-resolved spectroscopy, Aminoacyl tRNA synthetase, Single-stranded DNA, Organic light emitting diode

Student Number: 2011-23213

Contents

Abstract	i
I Super-resolution Microscopy and Single-molecule Spectroscopy	
1	
1 Introduction to Fluorescence	3
1.1 Electromagnetic Radiation and its Interaction with Molecules . . .	3
1.2 Jablonski Diagram	7
1.3 Absorption	10
1.4 Lifetime and Quantum Yield	11
1.5 Fluorescence Spectroscopy	14
1.5.1 Time-correlated Single-photon Counting (TCSPC)	14
1.5.2 Fluorescence Resonance Energy Transfer (FRET)	18
1.5.3 Fluorescence Correlation Spectroscopy (FCS)	23
2 Precise Intracellular Location Analysis of Leucyl-tRNA Synthetase by STED Microscopy	29
2.1 Introduction	29
2.2 Materials and Methods	32

2.2.1	HeLa Cell Preparation	32
2.2.2	Principle of STED Microscopy	33
2.2.3	Experimental Setup for Confocal and STED Microscope .	38
2.2.4	Data Analysis Method: Effective Co-local Factor (ECF) .	42
2.3	Results and Discussion	43
2.3.1	Leucine Dependent Co-localization of LRS and LAMP2 in Confocal Images	43
2.3.2	LRS Translocation to the Lysosomal Membrane in STED Images	45
2.4	Conclusion	48
3	Flexibility of Single-stranded DNA Measured by Single-molecule ALEX-FRET	49
3.1	Introduction	49
3.2	Materials and Methods	52
3.2.1	ssDNA Preparation	52
3.2.2	Experimental Setup for ALEX-FRET	54
3.2.3	ALEX-FRET Data Analysis	56
3.3	Results and Discussion	59
3.3.1	Flexibility of ssDNA with 3-nucleotides	59
3.3.2	ssDNA in Various Ion Concentration	61
3.4	Conclusion	63
4	Detection of Single Diffusing Molecule in Sub-diffraction-limit Volume by ALEX-FRET and STED Microscopy	65
4.1	Introduction	65
4.2	Materials and Methods	67
4.2.1	DNA Sample Preparation	67

4.2.2	Experimental Setup for ALFRED	68
4.3	Results and Discussion	71
4.3.1	Observing Single-molecules in Reduced Focal Volume	71
4.3.2	<i>E-S</i> Histogram with ALEX-FRET and ALFRED	75
4.4	Conclusion	79
	Bibliography	81

II Time-resolved Spectroscopy about Degradation Process of Organic Light Emitting Diode **91**

1 Introduction to Organic Light Emitting Diode (OLED) **93**

1.1	History and Working Principle of OLED	93
1.2	Degradation Problem	97

2 Study for Luminescence Properties of the Charge Traps in OLED using Transient Electroluminescence **101**

2.1	Introduction	101
2.2	Materials and Methods	103
2.2.1	OLED Fabrication	103
2.2.2	Transient Electro- and Photo-luminescence Measurements	104
2.2.3	Measuring Electronic Properties of OLED	105
2.3	Results and Discussion	106
2.3.1	Analysis of TREL Curves	106
2.3.2	The Charge Traps in Degraded Device	108
2.3.3	Luminescence Properties of the Charge Trap	113
2.4	Conclusion	118

3	Non-invasive and Layer-selective Analysis of OLED Degradation Process	121
3.1	Introduction	121
3.2	Materials and Methods	122
3.2.1	OLED Fabrication	122
3.2.2	Luminescence Intensity and Lifetime Measurements . . .	123
3.3	Results and Discussion	124
3.3.1	Experimental Concept for Layer Selective Degradation Analysis	124
3.3.2	Determining Which Layer is Degraded	125
3.4	Conclusion	129
	Bibliography	131
A	Molar Concentration Measurement and Bio-imaging Application of ZAIS/ZnS Core/Shell Nanocrystals	139
A.1	Introduction	139
A.2	Materials and Methods	141
A.2.1	Synthesis of ZAIS and ZAIS/ZnS NCs	141
A.2.2	Quantum Yield and Fluorescence Lifetime Measurements	142
A.2.3	Molar Concentration Measurements Using FCS	142
A.2.4	Imaging of HeLa Cell and Cell Viability Assay	144
A.3	Results and Discussion	145
A.3.1	Synthesis of ZAIS and ZAIS/ZnS NCs and Their Optical Properties	145
A.3.2	Determining the Molar Concentration and Extinction Coefficient of ZAIS/ZnS NCs	148

A.3.3	Application of ZAIS and ZAIS/ZnS NCs as an <i>in vivo</i> Imaging Probe	150
A.4	Conclusion	152
B	Generation of Highly Luminescent Micro Rings by Optical Ir- radiation	155
B.1	Introduction	155
B.2	Materials and Methods	156
B.2.1	Sample Preparation	156
B.2.2	Optical Microscopy and Spectroscopy	158
B.3	Results and Discussion	163
B.3.1	LMR Phenomenon	163
B.3.2	Characterization of the LMR	165
B.4	Conclusion	170
	Bibliography	173
	초록	179

List of Figures

I Super-resolution Microscopy and Single-molecule Spectroscopy

1.1	Plain-polarized electromagnetic radiation travelling along x axis .	3
1.2	Schematic representations of absorption, spontaneous emission, and stimulated emission processes in a two-level system	5
1.3	Jablonski diagram for absorption, fluorescence, and phosphores- cence	8
1.4	Principle of TCSPC	13
1.5	Electronic scheme for TCSPC	15
1.6	An example of the intensity decay curve for a fluorophore with two radiative states	17
1.7	Principle of FRET	19
1.8	FRET efficiency as a spectroscopic ruler	21
1.9	Fluorescence fluctuation	24
1.10	Schematic autocorrelation function changes for diffusion coeffi- cients and concentrations	26
1.11	Time scales of various dynamic processes monitored by autocor- relation analysis	28
2.1	Roles of leucyl-tRNA synthetase (LRS)	30

2.2	The intensity profiles of two adjacent particles.	33
2.3	Photophysics of STED microscopy	35
2.4	Excitation, STED, and effective PSF	36
2.5	Experimental setup for STED microscope	39
2.6	Location of intracellular LRS in absence or presence of leucine (-Leu, +Leu)	44
2.7	Confocal and STED images of LRS and LAMP2 in sufficient leucine condition (+Leu)	46
2.8	Intensity line profile of confocal and STED images	47
3.1	Sample design for studying the flexibility of ssDNA	52
3.2	Poisson distribution of the number of molecules according to con- centrations	53
3.3	Experimental setup for ALEX-FRET	55
3.4	Molecular sorting based on <i>E-S</i> histogram	56
3.5	Absorption and emission spectra of Cy3 and Cy5 and their crosstalk	58
3.6	Experimental <i>E-S</i> histograms of ssDNA overhang	60
3.7	Average FRET efficiency values for ssDNA ($N = 0-14$) in various metal ion concentrations	62
4.1	Experimental setup for ALFRED	69
4.2	Conceptual illustration of ALEX-FRET-STED (ALFRED) . . .	72
4.3	Focal volume reduction and subsequent change of Poisson distri- bution	73
4.4	FCS curves for dsDNA and their fitted autocorrelation function .	74
4.5	Fluorescence time trace of ALEX-FRET and ALFRED	75
4.6	2-D <i>E-S</i> histogram of donor-only and acceptor-only samples . . .	76
4.7	ALEX-FRET and ALFRED results of 5 nM dsDNA	77

II Time-resolved Spectroscopy about Degradation Process of Organic Light Emitting Diode

1.1	Evolution of OLED device structures	97
1.2	Energy level scheme of a typical heterojunction OLED	99
1.3	Reduced OLED brightness with operation time	100
2.1	Fabricated red phosphorescent OLED device and its luminescence properties	105
2.2	Experimental setup of TREL and TRPL	107
2.3	Schematic diagram of TREL experiments	109
2.4	TREL results of OLED devices during degradation process . . .	111
2.5	EIS and LSV results of OLED devices during degradation process	113
2.6	Decay curve analysis of OLED devices	116
2.7	t_0 , t_r , t_d , and a_2 versus degradation ratio graph according to off-time	118
2.8	Schematic diagram of TREL experiments when the charge traps inside the OLED device	119
3.1	Fabricated red phosphorescent OLED device and its luminescence properties	124
3.2	Device design that allows layer selective observation	126
3.3	Change in EL intensity during degradation	127
3.4	Change in PL intensity and lifetime during degradation	128

A.1	Synthesis process of ZAIS NCs using ultrasound technique	143
A.2	TEM images and spectria of ZAIS and ZAIS/ZnS NCs	148
A.3	Quantum yields and photoluminescence decay curves	149
A.4	Determining the molar oncentration of MPA-coated ZAIS/ZnS NCs with fluorescence autocorrelation curve	151
A.5	Confocal images of HeLa cells incubated with MPA-coated ZAIS and ZAIS/ZnS NCs	153
A.6	MTS cell viability assay	153
B.1	Experimental setup for optical microscope	161
B.2	Images of the luminescent micro ring (LMR)	164
B.3	Photophysical properties of the LMR	166
B.4	Control the diameter of the LMR	170
B.5	Simulated temperature at the interface between the glass cover- slip and the light-absorbing medium	171
B.6	LMR generated with 2 mM Atto540Q solution	172
B.7	Lifetimes of nanoparticle absorbers QD, FND, and those of the LMRs	173

Part I

Super-resolution Microscopy and Single-molecule Spectroscopy

Chapter 1

Introduction to Fluorescence

1.1 Electromagnetic Radiation and its Interaction with Molecules

Electromagnetic Radiation

Electromagnetic radiation can be described as a wave phenomenon formed by the combination of electric (E) and magnetic (H) fields, which oscillate in

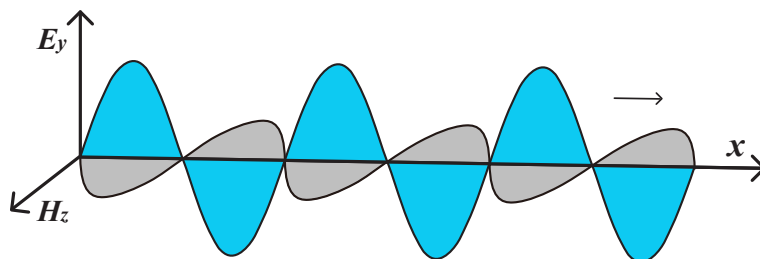


Figure 1.1 Plain-polarized electromagnetic radiation travelling along x axis. E_y is the electric component; H_z is the magnetic component.

phase orthogonal to each other and orthogonal to the direction of propagation as well [1, 2]. Figure 1.1 shows a plane-polarized (also known as linearly polarized) electromagnetic radiation. For a plane-polarized wave traveling in the x direction, the electric component of the radiation is in the form of an oscillating electric field of strength E in y axis, and the magnetic component is in the form of an oscillating magnetic field of strength H in z axis. The electric and magnetic fields of the electromagnetic radiation are given by

$$\begin{cases} E_y = A_E \sin(2\pi\nu t - kx) \\ H_z = A_H \sin(2\pi\nu t - kx) \end{cases} \quad (1.1)$$

where A is the amplitude, and $2\pi\nu$ is a frequency of the sinusoidally oscillating fields. The same k in two equations means that E_y and H_z are in-phase.

Interaction of Radiation with Matter

In figure 1.2, the i and j states of a molecule are stationary states. This pair of states may be, for example, electronic, vibrational or rotational states. Three processes are expected to occur when such a two-state system is irradiated with radiation of frequency ν , or wavenumber $\tilde{\nu}$, corresponding to the energy gap (ΔE) where

$$\Delta E = E_j - E_i = h\nu = hc\tilde{\nu}$$

The processes are including absorption, spontaneous emission, and stimulated emission.

Absorption: A molecule (X) absorbs a resonant radiation and is excited from the ground state (i) into the excited state (j).

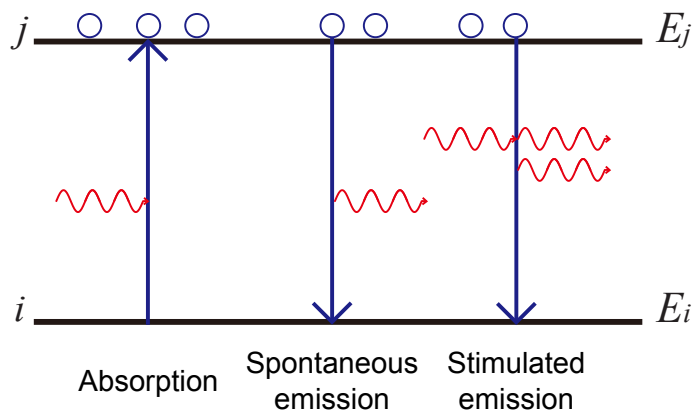
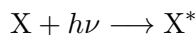
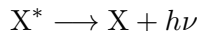


Figure 1.2 Schematic representations of absorption (left), spontaneous emission (middle), and stimulated emission (right) processes in a two-level system. i is a ground state which has an energy of E_i ; and j is an excited state which has an energy of E_j .



Spontaneous Emission: An excited molecule (X^*) spontaneously emits a radiation while it decays to the ground state.



Light emission that we usually encounter is the spontaneous emission, which is also called luminescence. It is called photoluminescence, in which molecules are excited by absorption of radiation spontaneously emit light. Photoluminescence is classified into fluorescence and phosphorescence depending on the electronic spin states involved in the transition.

Stimulated Emission: This is a different type of emission from the spontaneous emission. When the molecule is initially in the excited state, resonant light will de-excite the molecule to the ground state, and induce an emission of another photon with the same frequency. A radiation of frequency (ν) is

required to induce, or stimulate, the excited molecule to decay from j to i .



The generated photon is totally identical (coherent) to the incident photon in terms of a phase, frequency, polarization, and direction of travel. This is in contrast to spontaneous emission that occurs a random radiation regardless of the surrounding electromagnetic field. Stimulated emission is identical in form to the absorption but produces the opposite transition.

The name of electromagnetic radiation is defined according to its frequency (or wavelength) of oscillation. (In order of increasing frequency: radio wave, microwave, infrared radiation, visible light, ultraviolet radiation, X-rays and gamma ray) When electromagnetic radiation interacts with matter, its behavior is frequency dependent. Microwaves and infrared radiations cause the transition between the molecular rotational states and vibrational states, respectively. As the frequency increases to the visible range, photons have enough energy to change the bond structure of individual molecules and to cause the transition between molecular electronic states. X-rays and gamma rays ionize the molecule with energies above keV.

Fluorescence is a kind of phenomenon of the interaction of light and matter. Fluorescence begins when the UV-visible frequency light excites a molecule to a higher electronic state in an excited vibrational state. After excitation, the molecule in condensed phase undergoes vibrational relaxation and then emits a photon with a very small time delay and with a lower frequency than the incident light. Sometimes the molecule has a metastable state and retains its emission for a long time after the excitation radiation is turned off, that is called phosphorescence [1–6].

1.2 Jablonski Diagram

A life of an excited fluorophore is usually illustrated by the Jablonski diagram [7, 8]. In the first step, a fluorophore in the electronic ground state (S_0) is excited to a higher electronic state (S_n) by absorption of a photon of a particular wavelength. The Jablonski diagram shows how the excited fluorophore dissipates its energy.

The molecular energy levels are schematically described in the Jablonski diagram (Figure 1.3). Bold horizontal lines represent the electronic energy states. Within each electronic state, there are a number of vibrational states coupled with the electronic states. Rotational energy states are ignored in the Jablonski diagram. In a singlet state, all electron spins are paired according to ‘Pauli exclusion principle’ [9]. The spin of the excited electron is still paired with the ground state electron (opposite spin). Otherwise, in a triplet state, the excited electron is no longer paired with the ground state electron; they are parallel (same spin).

Absorption

The transitions from S_0 to S_1 or S_n is induced when the energy of the photon is transferred to the particular electron. Transitions occur in a short time about 10^{-15} s, which is too short for nuclei motion. This is the ‘Franck-Condon principle’, which is the approximation that an electronic transition is most likely to occur without changes in the positions of the nuclei [10, 11].

Vibrational Relaxation

Once a fluorophore is excited, several molecular processes can occur. The first step is a non-radiative process through vibrational relaxation. Fluorophores are

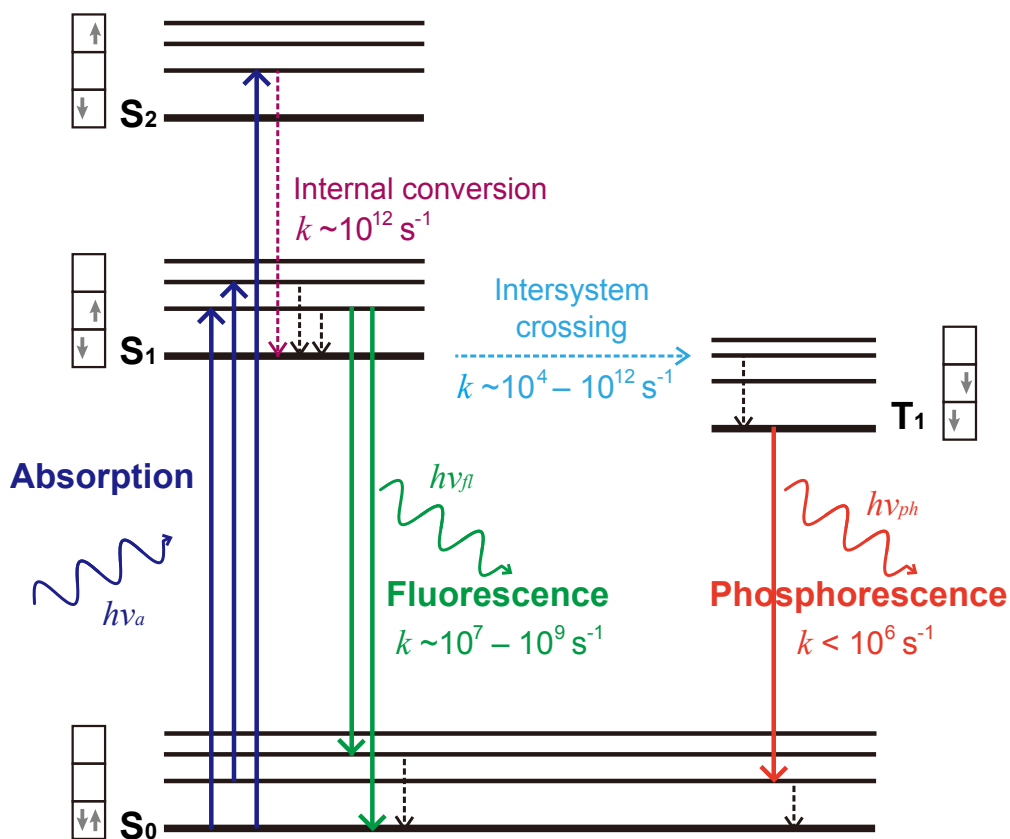


Figure 1.3 Jablonski diagram for absorption, fluorescence, and phosphorescence. It includes absorption (blue), fluorescence (green), phosphorescence (red) and the dotted lines represent non-radiative processes (internal conversion (purple), intersystem crossing (sky blue), and vibrational relaxation (black)).

usually excited to some higher vibrational levels of S_n . Molecules in condensed phases rapidly relax to the lowest vibrational level of S_1 . This process is called ‘internal conversion’ that occurs within 10^{-12} s or less.

According to ‘Kasha’s rule’ [12], the emission generally occurs only from the bottom of S_1 or T_1 no matter which electronic state is initially excited. Because higher excited states have larger density of states and shorter lifetime, vibrational relaxation and internal conversion ($S_n \rightarrow S_1$) is much faster than fluorescence from S_n . This fact explains the independence of the emission spectrum from the excitation wavelength.

Fluorescence

After vibrational relaxation of the excited fluorophore, it decays to the vibrational excited state of S_0 from the vibrational ground state of S_1 . Fluorescence refers to the luminescence generated during this process, which takes typically about 10^{-8} s.

The energy of fluorescence ($h\nu_{fl}$) is typically smaller than that of absorption ($h\nu_a$), which is called the ‘Stokes shift’ [13]. The fluorophore is predominantly in the lowest vibrational level of the ground electronic state at room temperature, depending on the Boltzmann’s distribution. On the other hand, the fluorophore is excited to a high vibrational state of S_n . Vibrational relaxation and internal conversion of the excited fluorophore are the cause of the energy loss. Another reason is that fluorophores mostly decay to higher vibrational levels of S_0 and then lose the excess vibrational energy.

Since the spacing between vibrational energy levels of S_0 and S_1 is usually similar, the emission and absorption spectra (plotted in energy units such as ν) are approximately mirror images. This similarity is because the nuclei geometries are not altered by the electronic excitation.

Intersystem Crossing

Molecules in the S_1 can undergo a spin conversion to the first triplet state (T_1) and it is called ‘intersystem crossing’. In most organic dyes intersystem crossing is fairly inefficient as a spin forbidden process, even though T_1 has lower energy than S_1 . As the spin conversion is more favourable in molecules with significant spin-orbital coupling, ‘intersystem crossing’ is most common in heavy-atom molecules (e.g., those containing iodine or bromine). Triplet emission (phosphorescence) is generally lower in energy compared to singlet emission (fluorescence). Transition from T_1 to the S_0 is, of course, forbidden and the phosphorescence lifetime is consequently several orders of magnitude longer than that of fluorescence lifetime.

1.3 Absorption

Fluorescence begins after the a fluorophore absorbs light. Beer-Lambert law states how light is absorbed by matter [14]. The absorption of light is directly proportional to the concentration of the attenuating species. The general Beer-Lambert law is usually written as:

$$A = -\log(I/I_0) = \varepsilon(\lambda) \cdot b \cdot C \quad (1.2)$$

Here, A is the measured absorbance and dimensionless because it is the ratio of incident light intensity (I_0) to the light intensity after passing through the sample (I). $\varepsilon(\lambda)$ is the wavelength-dependent extinction coefficient with units of $M^{-1}cm^{-1}$, typically in the range of $10^4 - 10^5 M^{-1}cm^{-1}$. The ε value is generally used to determine the concentration of the solution. b is the path length in cm unit, and C is the molar concentration.

The absorption discussed above does not take into account the polarization of light because the fluorophores in solution are randomly oriented. Fluorophores primarily absorb photons whose electric vectors (polarization) are aligned parallel to the transition dipole moment (μ) of the fluorophore. In other words, fluorophores can be excited only when the electric field of light pushes an electron in the right direction (the direction of the transition dipole moment). When the polarization of the excitation light is parallel to transition dipole moment of the fluorophore, the fluorophore totally absorbs the light. If two vectors (polarization and transition dipole moment) are perpendicular, the fluorophore does not absorb the light.

1.4 Lifetime and Quantum Yield

The lifetime and quantum yield are important characteristics of a fluorophore. Quantum yield is the number of emitted photons relative to the number of absorbed photons. Fluorophores with large quantum yields exhibit bright emission. The lifetime is also important, as it determines the time available for the fluorophore to interact with or diffuse in its environment, hence the information available from its emission [2, 5].

The lifetime is related to the rate at which excited fluorophores are de-excited. Recalling the two-state model in Figure 1.2, a time-dependent population change of excited fluorophores is described by:

$$\begin{aligned}\frac{dN_j(t)}{dt} &= -k_{ji} N_j(t) \\ N_j(t) &= N_j(0) \exp(-k_{ji} t)\end{aligned}\tag{1.3}$$

where $N_j(t)$ is the number of excited fluorophores at time t , k_{ji} is the rate constant of all de-excitation processes. The dimension of k is s^{-1} (transitions

per molecule per unit time). The lifetime of fluorophore (τ) is the reciprocal of k_{ji} .

$$\tau = \frac{1}{k_{ji}} = \frac{1}{k_r + \Sigma k_{nr}} \quad (1.4)$$

The de-excitation process can be divided into radiative and non-radiative pathways. k_r is the radiative rate constant and Σk_{nr} is the sum of rate constants of non-radiative pathways including intersystem crossing, inter-molecular energy transfer, excited state reaction and interaction with molecular environments. The lifetime is a statistical value when the number of excited molecules is reduced to 37% [15].

The quantum yield which is the number of emitted photons divided by the number of absorbed photons is given by

$$\text{QY} = \frac{k_r[\text{N}_j]}{k_r[\text{N}_j] + \Sigma k_{nr}[\text{N}_j]} = \frac{k_r}{k_r + \Sigma k_{nr}} = \frac{k_r}{k_{ji}} = \frac{\tau}{\tau_r} \quad (1.5)$$

where $\tau_r = 1/k_r$. Quantum yield is proportional to the lifetime.

If k_{nr} is much smaller than k_r , the quantum yield is close to unity. Additional non-radiative pathway increases Σk_{nr} , and consequently reduces τ and quantum yield. Such decreases in fluorescence intensity are called quenching processes, which include excited state reactions, energy transfer, complex-formation and collisional quenching. Collisional quenching occurs when the excited fluorophore contacts with an atom or a molecule that can facilitate non-radiative transitions to the ground state.

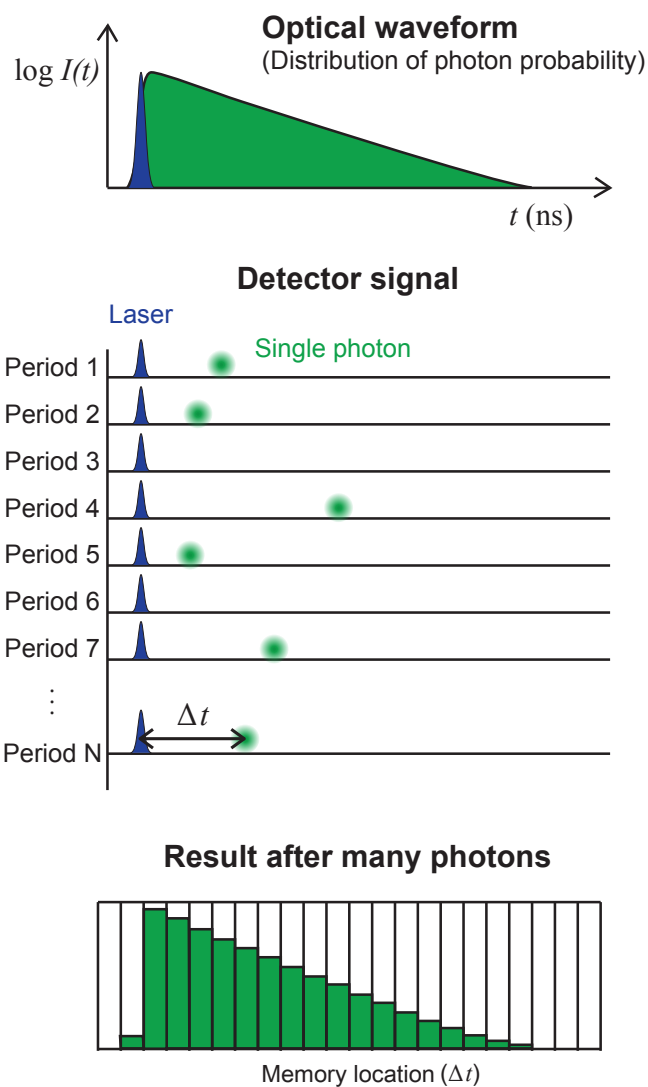


Figure 1.4 Principle of TCSPC. (a) shows an optical waveform for single exponential decay in a two-state model. (b) Repeated measurements of the time delay (Δt) between laser and fluorescence develop the histogram.

1.5 Fluorescence Spectroscopy

1.5.1 Time-correlated Single-photon Counting (TCSPC)

Principle

Time-correlated single-photon counting (TCSPC) is one of the most commonly used techniques for measuring lifetime. It is a simple and sensitive technique for recording low-level light signals with ps time resolution and high precision. After fluorophore is excited by pulsed light, the time-dependent intensity is measured following the excitation pulse [16,17].

The lifetime can be obtained by the time-dependent intensity profile. The excited state population $N_j(t)$ is proportional to fluorescence intensity. Hence, Equation 1.3 can also be written in terms of the time-dependent intensity $I(t)$.

$$I(t) = I_0 \exp(-t/\tau) \quad (1.6)$$

Figure 1.4a schematically shows the fluorescence intensity profile that decreases exponentially with time. The lifetime can be determined from the slope of a plot of $\log I(t)$ versus t , but it is more commonly determined by fitting the data to assumed decay models.

Figure 1.4b illustrates how the histogram is formed over multiple cycles. The sample is excited with a pulse of light, resulting in the waveform shown in Figure 1.4b. In TCSPC, we measure the time delay (Δt) between the excitation pulse and the observed photon and repeat this several thousand times to get a statistical histogram.

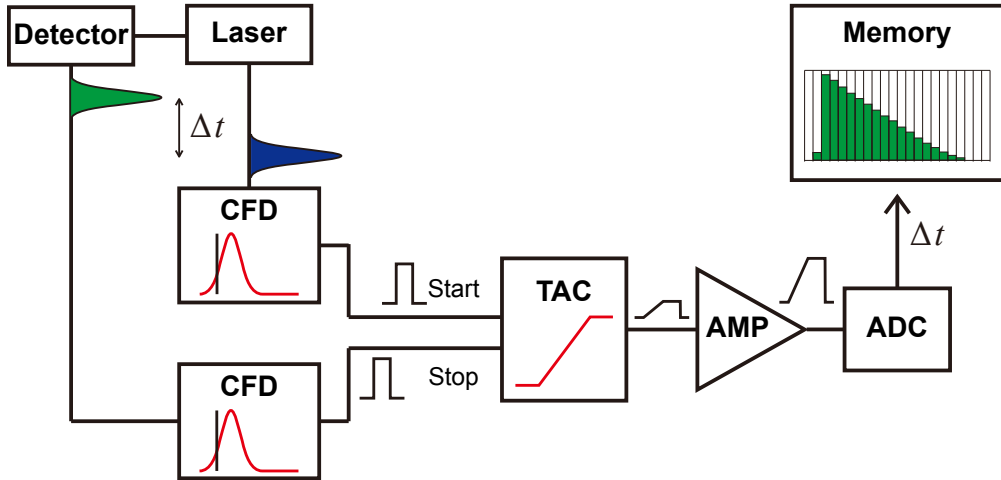


Figure 1.5 Electronic scheme for TCSPC. Laser signal starts the stopwatch of TAC, and detector signal stops the stopwatch. (CFD: constant fraction discriminator, TAC: time-to-amplitude converter, AMP: amplifier, ADC: analog-to-digital converter)

Measurement

To measure the dynamics of ns time scale, high repetition rate ps or fs laser light sources and high-speed photodetectors are needed. Figure 1.5 shows the electronics to measure the time interval [5, 18]. The excitation pulse from laser and the emission from detector send signals to the electronics. These signals are passed through a constant function discriminator (CFD), which accurately measures the arrival time of the signal. A time-to-amplitude converter (TAC) is the key electronics that acts like a stopwatch. It generates a voltage ramp increasing linearly over time on the ns time-scale. The first signal starts the voltage ramp and the second signal stops the voltage ramp, where the voltage value corresponds the time delay (Δt) between the two signals. Δt is accurately determined because TAC generates a voltage proportional to Δt . The voltage is amplified by amplifier and converted to a numerical value by the analog-

to-digital converter (ADC). The voltage is converted to a digital value that is stored as a single event with the measured time delay. A histogram of the decay is measured by repeating this process numerous times with a pulsed light source.

Time resolution of TCSPC is about tens of ps, which is an enough to measure fluorescence lifetime. To achieve better time resolution, it is important to use electronics with good time resolution but the most important factor is the ability of the detector. There is an alternative method of measuring the fluorescence lifetime using phase-modulation method, called frequency-domain lifetime measurements [19]. (TCSPC is a kind of time-domain measurement.) A sample is excited with intensity-modulated light varied at a high frequency typically near 100 MHz. Δt is measured as a phase shift, which can be used to calculate the decay time. Lifetimes as short as 10 ps can be measured by the frequency-domain method.

According to Figure 1.5, only one photon per laser pulse can be detected. If the sample emits more than two photons per pulse, the signal of the first photon stops the voltage ramp of the TAC, so the second arriving photon can not be considered. Therefore, the lifetime is measured to be shorter than the actual lifetime. We need to adjust the amount of detected photon so that less than one photon is generated per pulse. The detection rate is typically less than 1 photon per 100 excitation pulses. The photon counts should be less than 100 kHz when we use a 10 MHz laser.

The instrument response function (IRF) is the shortest time profile that can be measured by the instruments and usually obtained using scattering of glass without emission filters (Figure 1.6 dotted line). The full width at the half maximum (FWHM) of IRF is typically about a hundred ps and is determined by pulse-width of the laser (which is negligible small for a fs laser), the specification

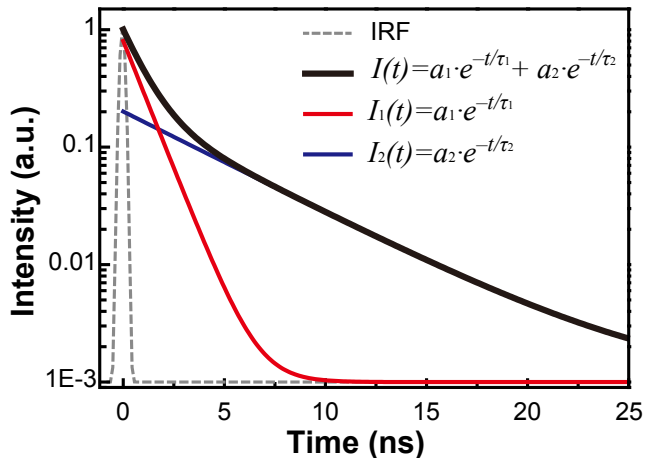


Figure 1.6 An example of the intensity decay curve for a fluorophore with two radiative states. Black line (τ_1 , τ_2) is the sum of red (τ_1) and blue (τ_2) lines. ($\tau_1 = 1$ ns, $\tau_2 = 5$ ns, $a_1 = 0.8$, and $a_2 = 0.2$)

of the detector, and the electronic time resolution of the electronics. IRF makes it difficult to observe the fast dynamics below 1 ns.

The lifetime of the fluorophore (τ) is obtained by fitting the TCSPC data to the exponential function (Equation 1.6). It is recommended to use a histogram with a maximum peak of 10^3 – 10^4 photons. Figure 1.6 shows an example of TCSPC results with a fluorophore having two different radiative decay paths (τ_1 and τ_2). TCSPC results appear as the sum of two exponential functions ($a_1 \cdot e^{-t/\tau_1} + a_2 \cdot e^{-t/\tau_2}$). The values of τ_n and their ratios (a_n) can be obtained by fitting the TCSPC data to the sum of exponential decay functions. The exponential fitting method is valid if the width of the IRF is relatively short compared to the width of the decay time. For the TCSPC data with a short lifetime, the measured intensity follows a mathematical convolution of the model function ($F(t)$) and IRF ($R(t)$), $I(t) = R(t) \otimes F(t)$.

As the lifetime does not depend on excitation power, detection efficiency, and photo-bleaching, it is more robust than fluorescence intensity. At the same time, lifetime is sensitive to changes of surrounding environments of fluorophores so that it is useful for detecting the environment including ion concentrations, refractive index, solvent polarity, local viscosity, pH of solvent, and the presence of quenchers. TCSPC is widely used in fluorescence spectroscopy, particularly for studies of biological macromolecules and cellular imaging.

Combination of TCSPC and confocal imaging technique enables fluorescence-lifetime imaging microscopy (FLIM). The lifetime of the fluorophore, rather than its intensity, is used to create an image in FLIM [20–22]. The lifetime is used to distinguish between different states of the same fluorophores depending on their environments [23–27]. FLIM is a simple way to know local environmental changes, which is widely used in biological research.

1.5.2 Fluorescence Resonance Energy Transfer (FRET)

Principle

Förster published his first account of non-radiative energy transfer and theoretically described a mechanism of energy transfer between two light-sensitive molecules [28–30]. The energy of an excited molecule (donor, D) can be transferred to another molecule (acceptor, A) through non-radiative dipole-dipole interaction (Figure 1.7).



After vibrational relaxation, the excited donor usually makes fluorescence. However, if there is an acceptor whose absorption spectrum overlaps the emission spectrum of the donor, the donor does not emit fluorescence. The acceptor absorbs the corresponding energy and makes the acceptor's fluorescence when

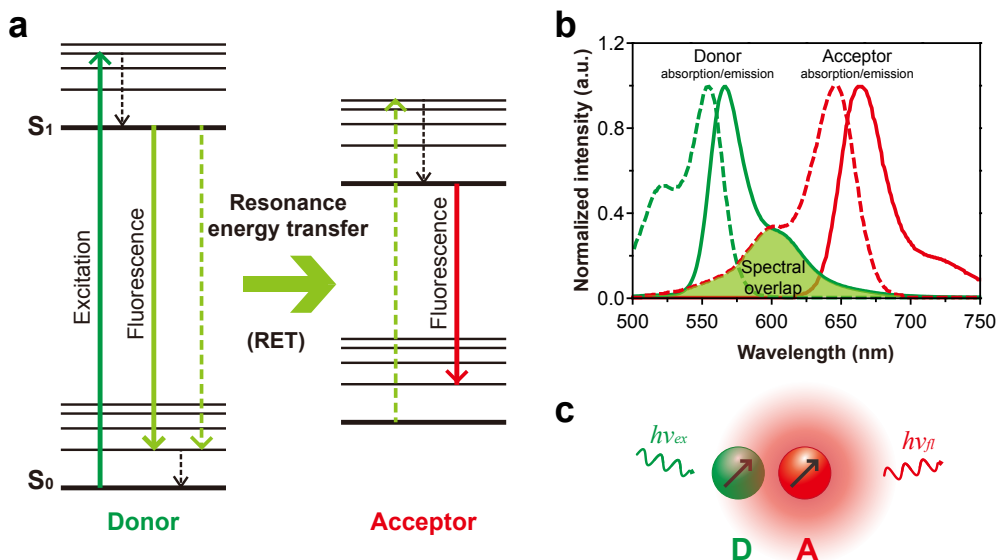


Figure 1.7 Principle of FRET. (a) Jablonski diagram of donor and acceptor molecules. In order for the energy of the donor to be transferred to the acceptor, the following three conditions are necessary: i) The emission energy of the donor overlaps with the excitation energy of the acceptor. ii) The distance between the donor and the acceptor is close enough. iii) The orientation of the donor and acceptor dipoles are aligned. (b) Absorption and emission spectra of Cy3 and Cy5 pair, a typical donor and acceptor pair. (c) shows the energy transfer between donor and acceptor when the above three conditions are all satisfied.

the two molecules are close to each other and their dipoles are aligned. The FRET efficiency is strongly dependent on the distance between two molecules, and thus it is often used to measure the intermolecular distance less than 10 nm [31].

Resonance energy transfer between a separate donor and acceptor pair of molecules occurs through a dipole-dipole interaction at a close distance. The rate constant of the energy transfer (k_{ET}) between two molecule pairs is inversely proportional to the sixth power of their distance [29].

$$k_{ET} = k_D \left(\frac{R_0}{R} \right)^6 \quad (1.7)$$

Here, k_D is $1/\tau_D$, where τ_D is the lifetime of the donor without acceptor, that is $k_D = k_{D,r} + \Sigma k_{D,nr}$. R is a distance between two dipoles. The value of R_0 for a singular pair of donor and acceptor molecules is:

$$R_0^6 = (8.789 \cdot 10^{-25}) \Phi_D \kappa^2 n^{-4} J(\nu) \text{ cm}^6 \quad (1.8)$$

where Φ_D is the quantum yield of the donor, κ is the orientation factor of the dipole coupling, $J(\nu)$ is the spectral overlap integral, and n is the refractive index of the medium. In Equation 1.8, we can find the conditions for FRET phenomenon between two fluorophores. i) The spectral overlap (J) between the emission spectrum of the donor and the absorption spectrum of the acceptor is required. ii) The donor and the acceptor should be close to each other (R), typically in the range of 1–10 nm. iii) It is also important to match the orientations (κ) of the two dipoles because the energy is transferred through dipole-dipole interaction. The orientation factor κ can be considered as 2/3 if the fluorophores are isotropically oriented [32].

Since FRET efficiency (E) is quantum efficiency of energy transfer, it can be expressed as follows.

$$E = \frac{k_{ET}}{k_r + k_{ET} + \Sigma k_{nr}} = \frac{k_{ET}}{k_D + k_{ET}} \quad (1.9)$$

where k_r and k_{nr} are the rate constants of radiative decay and any other de-excitation pathways, respectively, and constitute k_D . FRET competes kinetically with all the other possible de-excitation processes of the excited donor.

The FRET efficiency (E) is related with the distance between donor and acceptor (R), because k_{ET} is a function of R . The result of substituting Equation

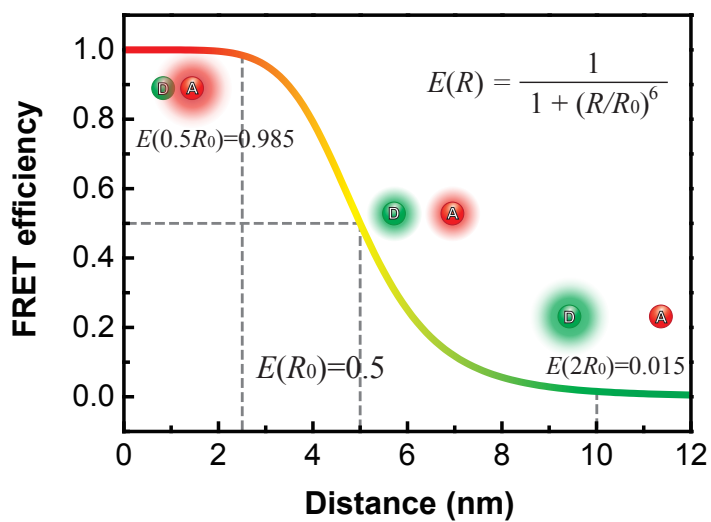


Figure 1.8 FRET efficiency as a spectroscopic ruler when $R_0 = 5$ nm. FRET efficiency depends on the distance between the donor and the acceptor as a relation of $E = [1 + (R/R_0)^6]^{-1}$. FRET efficiency changes sensitively near R_0 .

1.7 into Equation 1.9 is as follows.

$$E = \frac{k_D(R_0/R)^6}{k_D + k_D(R_0/R)^6} = \frac{1}{1 + (R/R_0)^6} \quad (1.10)$$

The equation implies that FRET efficiency are determined by the distance between two fluorophores. The change of FRET efficiency is very sensitive to the distance near R_0 (Figure 1.8). We can determine the distance between two fluorophores within 10 nm by measuring FRET efficiency.

Measurement

Experimental parameters such as fluorescence intensity or lifetime are used to measure the FRET efficiency. The transfer efficiency is calculated as:

$$E = 1 - \frac{F_{DA}}{F_D} = 1 - \frac{\tau_{DA}}{\tau_D} \quad (1.11)$$

We can find the FRET efficiency by measuring the fluorescence intensities of donor molecule with (F_{DA}) and without (F_D) acceptor, or lifetimes of a donor molecule with (τ_{DA}) and without acceptor (τ_D).

Some excitation energy of the donor is transferred to the acceptor, resulting in decreasing the donor fluorescence and increasing the acceptor fluorescence. The value of FRET efficiency is also calculated by detecting the fluorescence emissions from both the donor and acceptor:

$$E = \frac{F^A}{F^A + \gamma F^D} \quad (1.12)$$

where F^A and F^D are the fluorescence of the acceptor and donor when donor is excited, respectively. γ is a normalizing factor considering the difference in quantum yields and the detection efficiencies for donor and acceptor molecules.

$$\gamma = \frac{\Phi_A \eta_A}{\Phi_D \eta_D} \quad (1.13)$$

where Φ_A and Φ_D are the quantum yields of acceptor and donor, respectively, and η_A and η_D are the detection efficiencies at each emission range. The photophysical properties of fluorophores and instrumental detection efficiencies are corrected to obtaining the exact FRET efficiency.

The FRET pairs consisting of typical organic fluorophores have R_0 values in the range of < 10 nm, thus the FRET efficiency significantly changes in distances from 1 to 10 nm. The distance range of their interaction is comparable to the diameter of many proteins and to the thickness of membranes. The FRET is a very powerful tool for the biological sciences as a ‘spectroscopic ruler’ and has become widely used in all applications of fluorescence, including medical diagnostics, DNA analysis, and optical imaging. Specific examples of application are covered in chapters 3 and 4.

1.5.3 Fluorescence Correlation Spectroscopy (FCS)

Principle

Fluorescence correlation spectroscopy (FCS) is a technique that measures the change of fluorescence intensities through the observation volume. A laser usually focused on the diffraction limited detection volume and excites the luminescent molecules. Time-dependent change of fluorescence intensity, which is called fluorescence fluctuation, is caused by various reasons (Figure 1.9). Correlation analysis of fluorescence fluctuation gives us the molecular dynamic information that causes the change of fluorescence intensity [5, 33, 34]. In addition to translational diffusion, fluorescence fluctuations can occur due to rotational diffusion, intersystem crossing, photobleaching, and other excited-state reactions. FCS has been used to detect protein association reactions, DNA hybridization, immunoassays, binding to membrane receptors, gene expression, and diffusion

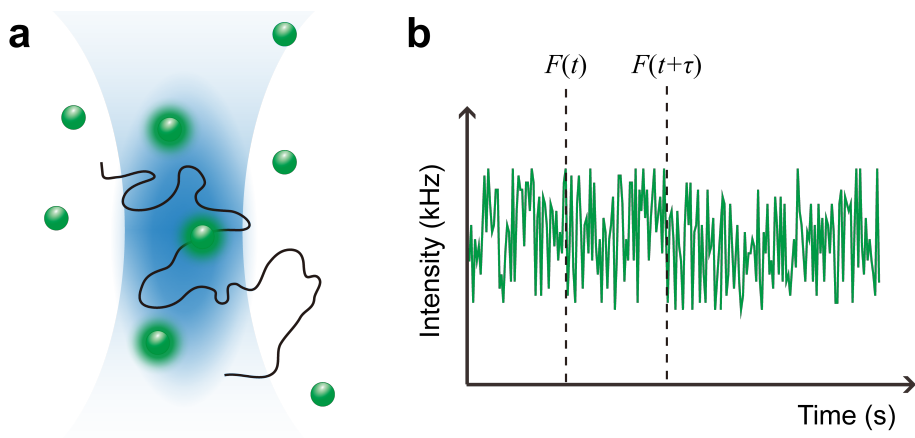


Figure 1.9 Fluorescence fluctuation. (a) Fluorophores in the effective detection volume can emit fluorescence. (b) Fluorescence fluctuation is caused by translational diffusion or other photophysics of fluorophores.

of labeled intracellular proteins [5, 35–37].

The intensity at a given time $F(t)$ is compared to the intensity at a slightly later time $F(t + \tau)$ (Figure 1.9b). The time (t) refers to the measuring time, typically from seconds to minutes. The lag time (τ) is the difference in real time between measurement of $F(t)$ and $F(t + \tau)$, typically in the range from 10^{-6} to 10^{-1} s. Note that the lag time τ in an FCS measurement is not related to the lifetime of the fluorophore. The autocorrelation function of the fluorescence intensity, $G(\tau)$, is averaged over a lot of measurements. The autocorrelation function for the fluorescence intensities, normalized by squared average intensity, is given by [5],

$$\begin{aligned}
 G'(\tau) &= \frac{\langle F(t)F(t+\tau) \rangle}{\langle F \rangle \langle F \rangle} = 1 + \frac{\langle \delta F(0)\delta F(\tau) \rangle}{\langle F \rangle^2} \\
 G(\tau) &= \frac{\langle \delta F(0)\delta F(\tau) \rangle}{\langle F \rangle^2}
 \end{aligned}
 \tag{1.14}$$

where $\delta F(t) = \langle F \rangle - F(t)$. For convenient calculation, we will use the second

equation $G(\tau)$ that is not including constant 1.

In order to interpret the FCS data, we need a theoretical model to describe the fluctuations. The intensity of fluorophore is related to several factors including the brightness of fluorophore ($B = q\sigma\Phi$), with quantum efficiency of detector (q), absorption cross-section (σ), and quantum yield of fluorophore (Φ). B is independent of time and space. In addition, collection efficiency ($CEF(r)$), excitation intensity distribution ($I(r)$), and distribution of fluorophore at time t ($C(r, t)$) affect the intensity. The measured intensity is expressed as:

$$F(t) = B \int CEF(r)I(r)C(r, t)dV \quad (1.15)$$

The integral extends over the entire observed space. $CEF(r)$ and $I(r)$ that depend only on r do not need to be distinguished. The product of $CEF(r)$ and $I(r)$ means the molecular detection efficiency, $p(r)$. Pinholes block the out-of-focus light in confocal setup, so the intensity profile ($p(r)$) of the focused laser is considered to be three-dimensional Gaussian function.

$$CEF(r)I(r) = p(r) = I_0 \exp\left[\frac{-2(x^2 + y^2)}{s^2}\right] \exp\left[\frac{-2z^2}{u^2}\right] \quad (1.16)$$

The radial radius (s) and axial half-length (u) refer to distances at which the profile decreases to e^{-2} of its maximal value I_0 .

In summary, the autocorrelation function for the intensity fluctuation is given by [5]

$$G(\tau) = \frac{B^2 \iint p(r)p(r') \langle \delta C(r, 0)\delta C(r', \tau) \rangle dV dV'}{[BC \int p(r) dV]^2} \quad (1.17)$$

where r is the position of the fluorophore at $t = 0$ and r' is its position at $t = \tau$. The denominator contains only the average intensity that means the average concentration of fluorophores C , while the numerator calculates the intensity

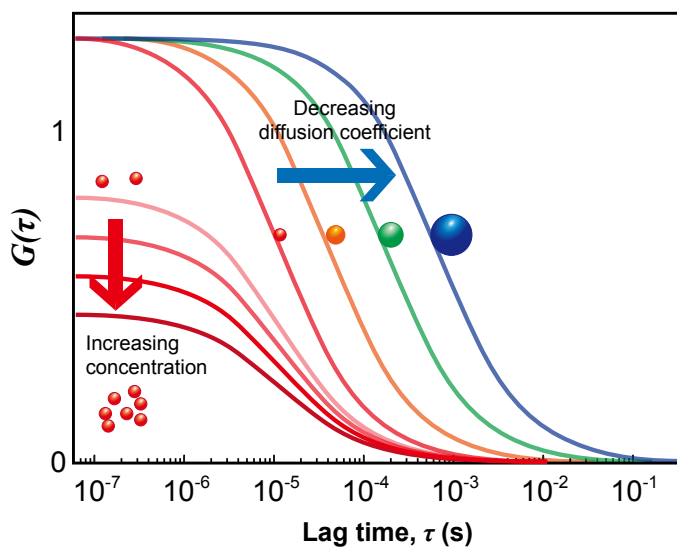


Figure 1.10 Schematic autocorrelation function changes for diffusion coefficients and concentrations. When the diffusion coefficient decreases, the diffusion time becomes longer and $G(\tau)$ appears at longer time. As the concentration of the sample increases, $G(0)$ decreases, therefore, the magnitude of $G(\tau)$ decreases.

fluctuations. This equation shows that we measure the correlation between fluorophore locations that is independent on the brightness of the fluorophore.

Chemical or photochemical processes that change the fluorescence intensity can be studied using the Equation 1.17. By substituting the appropriate model for $C(r, t)$, the expected autocorrelation function can be derived.

Translational Diffusion

Most common application of FCS is to measure translational diffusion in confocal detection volume. We assume that the distribution of fluorophore, $C(r, t)$ depends on the diffusion only, and is described as below [5, 38].

$$\langle \delta C(r, 0) \delta C(r', \tau) \rangle = \bar{C} (4\pi D \tau)^{3/2} \exp \left[\frac{-|r - r'|^2}{4D\tau} \right] \quad (1.18)$$

where D is the diffusion coefficient. Insertion of Equation 1.18 in Equation 1.17 yields the correlation function for three-dimensional diffusion:

$$G(\tau) = G(0) \left(1 + \frac{\tau}{\tau_{\text{Diff}}} \right)^{-1} \left(1 + \frac{s^2}{u^2} \frac{\tau}{\tau_{\text{Diff}}} \right)^{-1/2} \quad (1.19)$$

where $G(0)$ is the amplitude at $\tau = 0$, diffusion time (τ_{Diff}) is defined as $\tau_{\text{Diff}} = s^2/4D$. τ_{Diff} and D are determined by least-squares fitting of the simulated curve with the measured data. As the fluorophores diffuse more slowly into and out of the observed volume, the correlation function shifts to longer τ values, which reflects slower intensity fluctuations (Figure 1.10 horizontal change). On the other hand, the concentration of fluorophores affect the amplitude of the autocorrelation curve $G(0)$ (Figure 1.10 vertical change). The number of molecules (N) is given by the inverse of $G(0)$ ($N = 1/G(0)$). Since C is proportional to N , while δC is proportional to the root of N according to the Poisson distribution.

FCS is a powerful technique based on a statistical analysis of fluorescence fluctuations including various photophysical properties of fluorophore. If we prepare a proper fitting function for corresponding dynamics of $C(r, t)$, we can analyse the fast internal dynamics and photophysical processes as well as the diffusion dynamics using FCS. Figure 1.11 shows a schematic autocorrelation curve for different kinetic processes. In principle, FCS covers a wide temporal range from nanoseconds to several seconds, therefore allowing a simultaneous measurement of processes having different time scales.

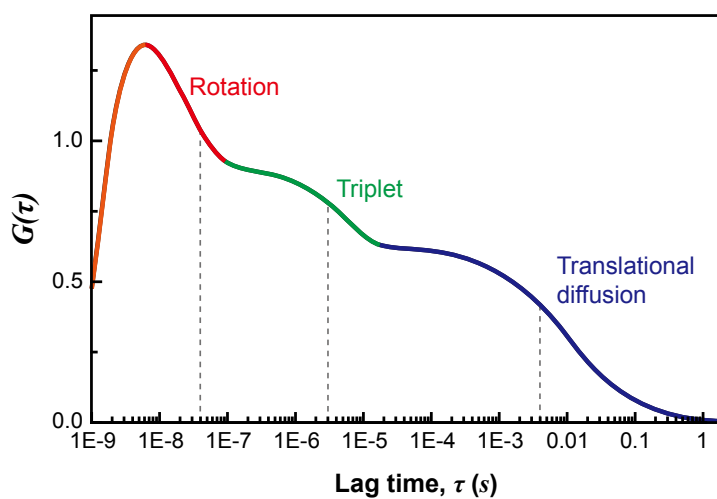


Figure 1.11 Time scales of various dynamic processes monitored by autocorrelation analysis. FCS can simultaneously measure photophysical processes that affect to the fluorescence intensity.

Chapter 2

Precise Intracellular Location Analysis of Leucyl-tRNA Synthetase by STED Microscopy

2.1 Introduction

Leucyl-tRNA Synthetase (LRS), Lysosome, and mTORC1

Lysosomes play a role in catabolism by degrading extracellular and intracellular materials. Specially, mechanistic target of rapamycin complex 1 (mTORC1) localizes in its active form on the surface of lysosomes and regulates energy levels, growth signals, and nutrient along with other functions [39]. The mechanisms for tight crosstalk between mTORC1 activity and lysosomal function have been reported. Multiprotein complexes on the lysosomal surface, including Rag GTPases and a v-ATPase for an amino acid-sensing device, have been shown to influence catabolism at different levels through mTORC1 regulation in lysosomes [40, 41].

Leucyl-tRNA synthetase (LRS) is well-known as one of the aminoacyl-tRNA

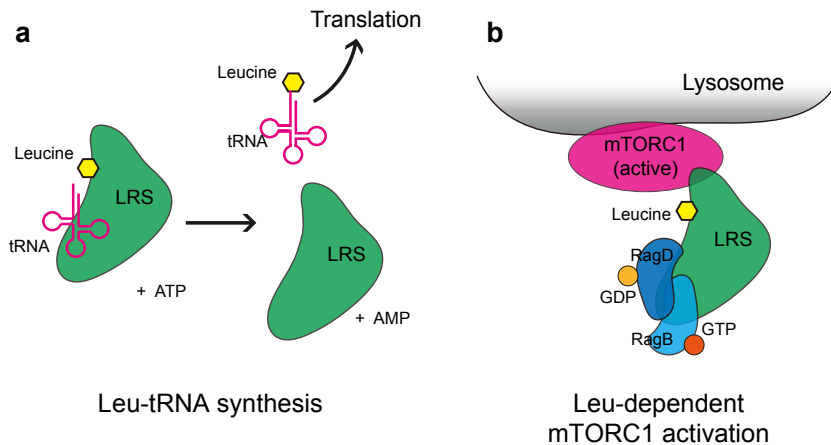


Figure 2.1 Roles of leucyl-tRNA synthetase (LRS). (a) Canonical role; LRS conjugates leucine and cognate tRNA. (b) Non-canonical role; LRS binds to RagD and activates mTORC1 in a leucine dependent manner.

synthetases (ARSs) which charges amino acids to their cognate tRNAs (Figure 2.1a). ARSs also play an important role in humans, interacting with many cancer-related proteins or involve in important signal pathways (Figure 2.1b). In previous studies, it is revealed that LRS plays a critical role in amino acid-induced mTORC1 activation by sensing intracellular leucine concentration and initiating molecular events leading to mTORC1 activation [42, 43]. When the leucine-binding ability of LRS was ablated, the mTORC1 pathway to this amino acid was desensitized [42]. LRS directly binds to Rag GTPase, the mediator of amino acid signaling to mTORC1, in an leucine-dependent manner. Amino acids induce the movement of mTORC1 to the lysosome, where the Rag GTPases reside [44–46].

LRS translocation to the lysosome depending on leucine is involved in mTORC1 activation. We revealed that LRS is in the endomembrane fraction with mTORC1 after adding leucine because mTORC1 translocates to the lyso-

some with amino acids. We used super-resolution fluorescence microscopy to directly visualize that LRS translocates to the lysosome and to determine its location in the lysosome.

The Need for Super-resolution Microscopy

Optical microscopy has the enormous advantages because *in vivo* detection is possible with its non-invasive properties. The technique is especially compared to other microscopy, such as electron microscopy or scanning probe microscopy. The diffraction limit of light, however, gives the optical microscope a resolution limit [47]. One possible way to reduce the excitation spatial extent is to suppress fluorescence outside the excitation region. Stefan W. Hell proposed a new concept of super-resolution microscopy that overcomes the optical diffraction limit utilizing stimulated emission in 1994 [48] and experimentally demonstrated the stimulated emission depletion (STED) microscopy in 1999 [49]. The effective spatial extent is confined when excited fluorophores are de-excited by stimulated emission. The principle of STED is discussed in detail in Section 2.2.2.

STED technique has developed multicolor [50–52], three-dimensional (3D) [50, 53], live cell [54, 55], and video-rate [56, 57] imaging techniques. STED microscopy has been successfully applied to diverse areas such as biochemistry and molecular cell biology [55, 58–63]. We introduced two-color STED microscope to directly observe the intracellular location of LRS and lysosomal associated membrane protein 2 (LAMP2) according to leucine signal. The improved resolution of the STED allows us to observe the subcellular structures of the lysosome. We can confirm that LRS translocates to lysosomal membrane to activate mTORC1, which regulates protein translation, cell size, and autophagy.

2.2 Materials and Methods

2.2.1 HeLa Cell Preparation

HeLa cell lines were cultured according to conventional method. HeLa cells were seeded on coverslips (9 mm x 9 mm, Bellco) with 95% viability and cultured in DMEM medium (Welgene) supplemented with 10% heat inactivated fetal bovine serum and 1% penicillin-streptomycin at 37°C in cell incubator containing sufficient water vapor and 5% CO₂.

For leucine depletion (-Leu sample), cells were rinsed 2 times with leucine free DMEM (Welgene) and incubated in leucine free DMEM for 60 minutes. For leucine stimulation (+ Leu sample), cells were rinsed 2 times with leucine free DMEM and incubated in leucine free DMEM for 50 minutes and incubated in general DMEM for 10 minutes.

After controlling the leucine signal, we prepared the sample for fluorescence imaging. HeLa cells were fixed with 4% paraformaldehyde (PFA) for 15 minutes at room temperature (RT) and incubated with permeabilization solution (PBS:Triton X-100:BSA = 100:0.4:5) for 15 minutes at RT. After this process, HeLa cells were incubated with anti-LAMP2 (ab25631, Abcam) and anti-LRS (A304-315A, Bethly) primary antibody (1/100 for anti-LAMP2, 1/1000 for anti-LRS diluted with PBS containing 5% BSA) at RT for 1 h. Then cells were rinsed 3 times with PBS for 5 minutes and incubated with secondary antibody conjugated with Alexa 488 or STAR 635P (1/1000 diluted with PBS containing 5% BSA) at RT for 1 h. Finally, we rinsed the cells 5 times with PBS for 5 minutes to eliminate the unlabeled fluorophores and mounted with mounting medium (P36930, Invitrogen).

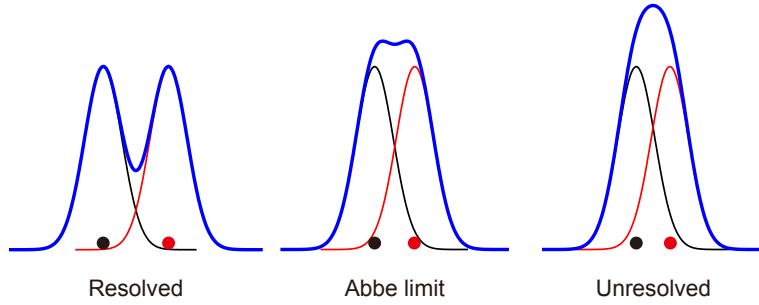


Figure 2.2 The intensity profiles of two optically observed adjacent particles (black and red). Sum of two point spread functions (PSFs) is shown in blue. The particles within the optical diffraction limit can not be optically distinguished.

2.2.2 Principle of STED Microscopy

Basic Photophysics for STED Microscopy

The image of a complex object is seen as a convolution of the true object and the point spread function (PSF) (Figure 2.2. The PSF is the diffraction pattern of light emitted from an infinitely small point source and is shown Airy pattern for confocal microscope. The diffraction pattern is determined by the wave nature of light. Ernst Abbe first discussed the optical diffraction limit in 1873 and formulated it as following [47]:

$$\Delta r \approx \frac{\lambda}{2n \sin \theta} = \frac{\lambda}{2NA} \quad (2.1)$$

where Δr is the resolution, λ is the wavelength of light, n is the refractive index of the medium, θ is the semi-aperture angle of objective lens. Usually, $n \sin \theta$ is expressed as NA, numerical aperture. Due to the diffraction limit of light, optical microscopy has a lateral resolution limit of about half the wavelength (Figure 2.2 Abbe limit). It is not possible to distinguish between two objects that are nearby each other within 200 nm laterally and 500 nm axially with

visible light. One possible way to improve the resolution is to reduce fluorescence from a part of excitation region through stimulated emission.

Once an fluorophore is excited to S_n state, the energy of fluorophore is dissipated by vibrational relaxation or internal conversion (non-radiative relaxations) within 10 ps (Figure 2.3). The excited fluorophore is in vibrational ground state of the first electronic excited state (S_1) and then returns to electronic ground state (S_0) with fluorescence (\sim ns). It is also called the spontaneous emission. However, if an incoming electromagnetic wave of a specific energy comes in before fluorescence occurs, it can induce light emission (stimulated emission). Fluorescence can not occur in the areas where the stimulated emission occurs prior to fluorescence. This trick is used to overcome the diffraction limit.

Obtaining a High Resolution with STED Microscopy

In order to reduce the effective focal volume, we use a phase plate to make the STED beam doughnut-shaped. The circular phase plate shifts the phase of the beam radius (xy section) from 0 to 2π . When the STED beam is focused by the objective lens, the center of the STED beam disappears due to the destructive interference to form a doughnut-shaped beam (Figure 2.4b). Because the doughnut-shaped beam itself is also light, it follows the diffraction limit; therefore, the STED beam that has similar power to excitation beam hardly improves the resolution. As the STED beam intensity increases, the center of the doughnut-shaped beam (the effective PSF) is reduced, thereby improving the resolution (Figure 2.4). The resolution is affected by the intensity of the STED beam, which follows that [66, 67],

$$\Delta r \approx \frac{\lambda}{2n \sin \alpha \sqrt{1 + \frac{I_{\text{STED}}}{I_{\text{sat}}}}} \quad (2.2)$$

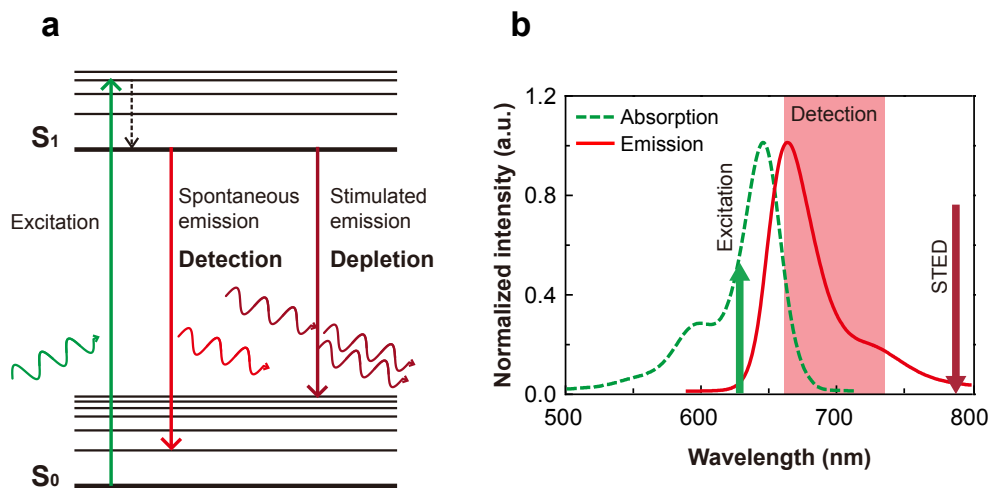


Figure 2.3 Photophysics of STED microscopy. (a) Simple Jablonski diagram of typical fluorophore. The excited fluorophore can emit photon through spontaneous or stimulated emission. (b) Absorption and emission spectra of ATTO647N dye, a typical organic fluorophore. Relation between the excitation, detection and STED wavelengths are shown. The spontaneous emission is detected as signal and stimulated emission is used for depletion of fluorophore in STED microscope. The stimulated emission is efficient at the wavelength with high spontaneous emission intensity, because both spontaneous emission and stimulated emission are correlated with oscillator strength [64,65]. However, we select a long wavelength STED near the red edge of emission spectrum which has less interference in excitation and fluorescence. When we use high power of STED light, it induces the excitation of fluorophore due to crosstalk. Besides, the STED microscope inevitably has a lower intensity per pixel than the conventional confocal microscope. To obtain as much fluorescence as possible, STED at long wavelength is irradiated with high intensity.

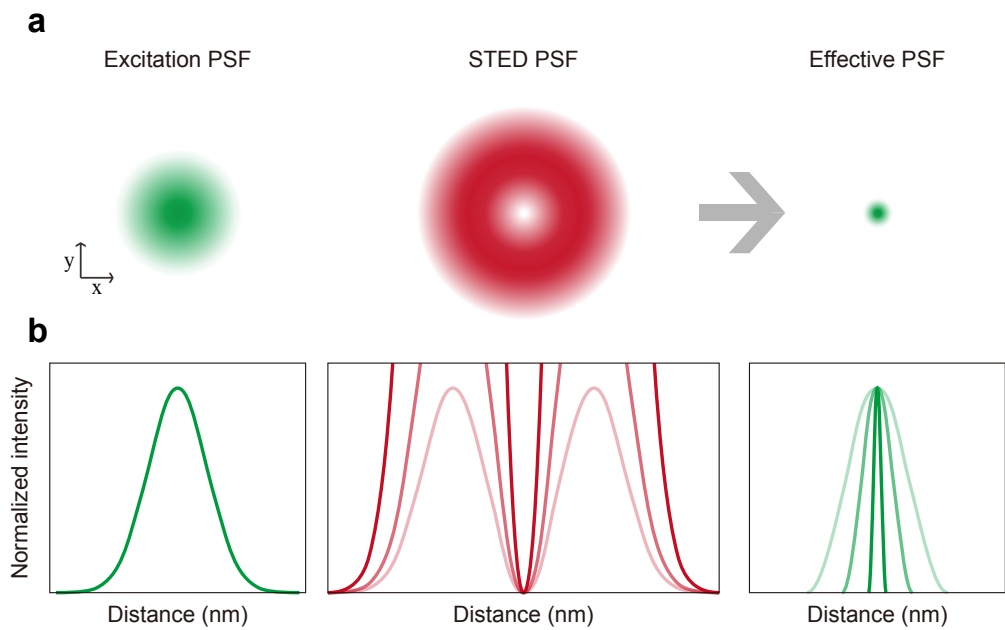


Figure 2.4 (a) xy cross-section images and (b) line profiles of excitation, STED, and PSF. As the STED intensity increases, the effective PSF decreases (light to dark color).

where n is the refractive index of the medium, I_{STED} is the depletion intensity in experiments and I_{sat} is the saturation intensity. The depletion efficiency is mainly affected by $I_{\text{STED}}/I_{\text{sat}}$. Effective sub-diffraction resolution is only achieved when $I_{\text{STED}} \gg I_{\text{sat}}$. I_{sat} , at which a half of the fluorescence is suppressed by STED, is given by $I_{\text{sat}} = h\nu/\sigma\tau$, where $h\nu$ is the photon energy; σ is stimulated emission cross section; τ is the lifetime [68–70]. The higher STED power, the higher the resolution will be, but there is a limit due to the optical stability of the fluorophores and the damage of the sample. The lateral resolution is typically between 30 and 80 nm, and 2.4 nm resolution have been reported [71]. Efficient stimulated emission results in improved resolution.

To achieve effective depletion an excitation beam and a STED beam should be finely aligned in spatial position. In pulsed STED, two beams should be also aligned in time. A STED beam that has hundreds of ps pulse duration usually follows a excitation beam after ~ 150 ps delay. During the delay time, the most of the excited molecules undergo vibrational relaxation to the vibrational ground state of the S_1 . The pulse-CW STED scheme has low depletion efficiency due to the unintended temporal overlap of the two beams. A strong intensity of the CW STED beam is typically needed to achieve a similar performance to the pulse-pulse scheme.

Compared to conventional confocal microscopy with hundreds of nm resolution, STED microscopy has improved resolution by 10–20 times. This resolution is particularly suitable for viewing the structure of intracellular organelles. STED microscopy with improved resolution is capable of observing the detailed structure of the organelles. HeLa cells, a typical mammalian cell, are 15–30 μm in diameter and the lysosomes in HeLa cell is about 0.1 to 1.2 μm . With confocal microscopy, it is difficult to observe the detailed structure of the organelles, which is possible with STED microscopy.

2.2.3 Experimental Setup for Confocal and STED Microscope

Home-built confocal and STED (continuous wave and pulsed) microscopes are schematically shown in Figure 2.5. Both microscopes share the same setup based on scanning microscope. The confocal microscope is to observe the fluorescence with excitation beam only, and the STED microscope is to observe fluorescence with the addition of the STED beam to the excitation beam.

We used Ti-sapphire laser (< 100 fs, 80 MHz, MaiTai HP, Spectra-Physics) for pulse-pulse STED microscope. Faraday isolator (FI-780-5SV, Linos), in front of laser, prevents the reflected laser light from re-entering to the laser. Ti-sapphire laser beam is separated into two paths by polarizing beam splitter (PBS) and half-waveplate for excitation (visible, 488–635 nm) and STED (800 nm).

Excitation Paths

First, for the excitation beam, a super-continuum light (470–1600 nm) is generated by photonic crystal fiber (FemtoWhite800, NKT Photonics) and two plano-convex lenses with short focal length. The super-continuum light is divided in three wavelengths (488, 532, and 635 nm) mainly by long pass dichroic filter which highly reflective below the cutoff wavelength and highly transmissive above it at a 45° angle of incidence. Three colored excitation beams are focused into a polarization maintaining single mode fibers (P1-488PM-FC) using plano-convex lens (Vis, achromat, $f=10$) for beam cleanup. 488 nm and 635 nm are respectively selected for 2-color imaging of Alexa 488 and STAR 635P dyes using excitation filters (L488-10, Thorlabs for 488 nm and z635/10x, CHROMA for 635 nm). After the fiber, an achromatic plano-convex lens with focal length of 40 mm enlarges the beam to a diameter of ~ 1 cm. The colli-

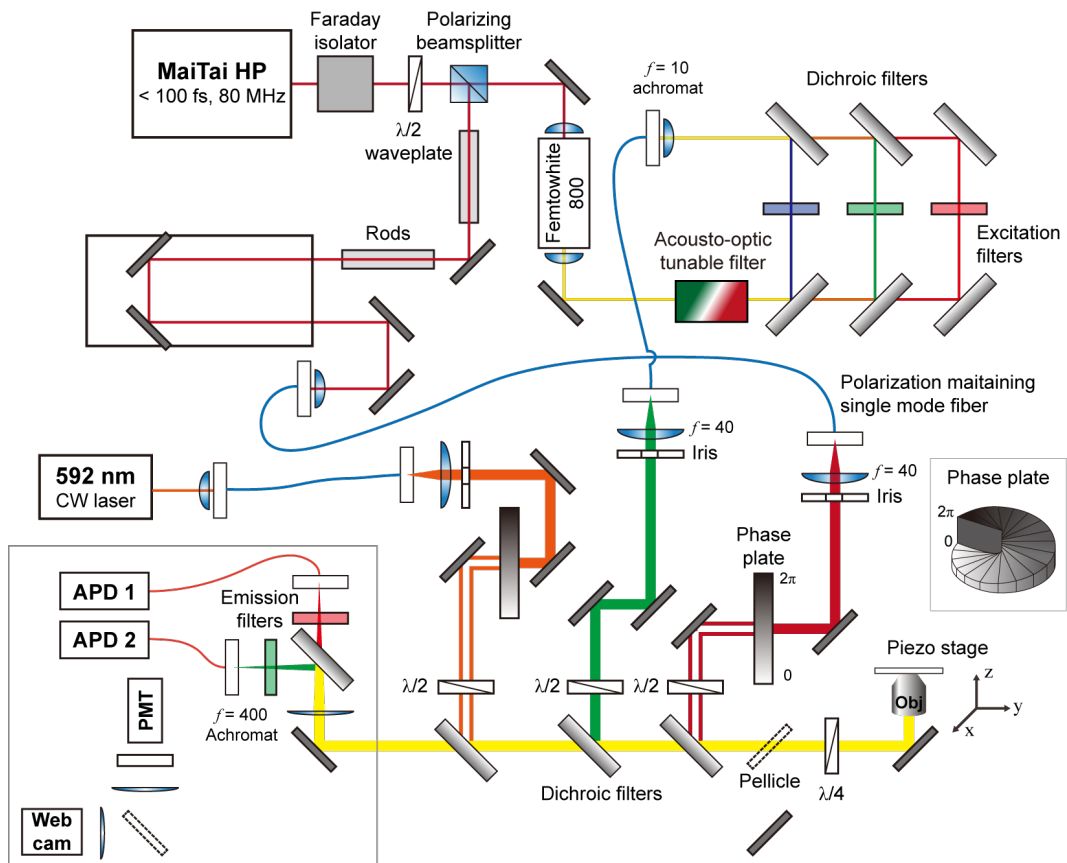


Figure 2.5 Experimental setup for STED microscope. It includes one excitation and two STED sources. Two APDs measure the fluorescence of two different fluorophores separately. (APD: avalanche photodiode, PMT: photomultiplier tubes)

mated beam is achieved by adjusting the length between lens and fiber end. The shear plate is usually used to test the collimation of beam. The shearing interferometer works only with continuous wave (CW) laser because it observes the interference of reflected beam. The collimation of the pulsed laser is adjusted based on the collimated CW laser. We also use an iris to adjust the beam size to the objective back aperture size. The excitation beams reflected on the dichroic mirror (Di01-R405/488/561/635-25x36, Semrock) enter the objective lens. In this process, an achromatic half-wave plate and an achromatic quarter-wave plate (RAC 3.2.15, RAC 3.4.15, B. Halle) are used to make circular polarized beam so that the dyes are excited regardless of their transition dipoles.

STED Paths

The 800 nm pulsed STED beam has a very high peak intensity because the Ti-sapphire laser generates very short pulse duration, less than 100 fs. The pulse width is stretched to ~ 5 ps to prevent spectral broadening using rods (ROD-12-12-200-FDS90-600-900, CVI). An 100 m-long polarization maintaining single mode fiber (PMJ-A3HPC,3S-633-4/125-3-100-1-SP, 100m, OZ Optics) further stretches the beam to ~ 280 ps. When the pulse duration time of STED is elongated to hundreds ps, the photo-damage to the sample and fiber is reduced as the peak intensity is decreased. Duration of stimulated emission is prolonged, thereby depletion efficiency increased. 592 nm STED laser (2RU-VFL-P-1500-592, MPB Communications) generates CW, so additional time expansion is not required.

Two STED beams (592 nm, 800 nm) follow a similar path to the excitation beam described above (polarization maintaining single mode fibers, half-wave plate and quarter-wave plate, and dichroic mirror (ZT594dcrb, Chroma for 592 nm and FF756-Sdi01-25x36, Semrock for 800 nm). The difference from the

excitation beam path is that STED beams pass through the phase plate (VPP-1a, RPC Photonics) to make a doughnut-shape beam at focal plane. Due to the sequential phase shifting from 0 to 2π , destructive interference occurs on the center of the STED beam. The central part is vanished after being focused by an objective lens, which results in the doughnut-shape. If we use π -phase plate, we can make z -doughnut, which results 3D STED images.

Beam Alignment

Two excitation beams (488, 635 nm) and two STED beams (592, 800 nm) are combined through dichroic mirrors and focused to the sample by an oil immersion objective (HCX PL APO 100X, 1.4 NA, Leica). The beams are aligned in exactly same position at focal plane, while imaging the scattering of 80 nm Au beads with photomultiplier tubes (MP962, PerkinElmer) in non-confocal mode. In the case of pulsed STED, excitation and STED beam should be related temporally as well as matched their locations. We adjust the interval between excitation and STED pulses to 160 ps using Daedal (linear positioner, step motor: ZETA57-83-MO, Parker, driver: ZETA6104, Parker, moving 300 mm with 2 μm step size) to increase depletion efficiency. The optimal time interval depends on the fluorophore. Avalanche photodiode detectors (APD) (PFCCTC-FCAPC, MPD) with a short instrumental response function and time-correlated single photon counting (TCSPC) module (SPC-150, Becker & Hickl) are used for detecting the timing of lasers.

Acquiring Images

After alignment, we can obtain a confocal and STED image by scanning the sample using piezo stage (NanoMax-TS, Thorlabs). In this study, pixel sizes were 20 nm in the 800 nm STED and approximately 51 nm in the 592 nm

STED and confocal images, and dwell time per pixel was 200 μ s. The fluorescence signals from two different dyes passes the multimode fiber (62.5 μ m diameter, M31L01, Thorlabs) through plano-convex lens (f=400) to eliminate the backgrounds. Two signals are divided by dichroic filter (ZT633drc, Chroma) and detected by two different APDs (SPCM-AQR-14-FC, Perkin Elmer). Some emission filters and notch filters (ET525/50m (Chroma) and ZT594dcrb-UF1 (Chroma) for Alexa 488, ET700/75m (Chroma), FF01-720/SP (Semrock), and NF03-785E (Semrock) for STAR 635P) are used to detect only each fluorescent signal. A multi-channel analyzer (MCA) (P77782, FAST ComTec) performs further processes to make images. The piezo stage is controlled by an analog output board (PCI-6731, National Instrument). Imaging and post-imaging processes are performed with the software programs Inspector and ImageJ. Inspector program is kindly supported by the Max-Planck Institute.

The bright field images are acquired using CCD of webcam. For confocal images, a laser power of several μ W is used for the excitation power; For the STED images, hundreds of mW STED is added. The high power of STED beam may cause the photo-bleaching of dyes.

2.2.4 Data Analysis Method: Effective Co-local Factor (ECF)

To quantify the co-localization between two fluorescence channels (LRS and LAMP2), we examine how many pixels are co-localized in the image. However, it is not enough to count how many pixels overlap between the channels because the co-localization is also related to the absolute number of pixels of each channel. The co-localization depends on the density of pixels, resulting in wrong statistical analysis and large standard deviation.

In this study, we introduced an effective co-localization factor (ECF), which considers the co-localization that spontaneously happens between theoretically

random-arranged pixels. ECF is calculated using the following formula:

$$\text{ECF} = \frac{\text{The experimental co-localization}}{\text{Monte Carlo simulation co-localization}}$$

The experimental co-localization means how many pixels overlap between two channels and Monte Carlo simulation co-localization means how many pixels overlap between random-arrange channels. To calculate the theoretically random-arranged pixels, we count the total number of pixels of each channel (experimentally obtained) and scatter these pixels to their respective channel using Monte Carlo simulation. Then we count the number of the co-localized pixels in the simulated images.

The ECF evaluates only the interaction between two channels. The ECF larger than 1 means the effective interaction between two channels. We analyzed the co-localization using ECF.

2.3 Results and Discussion

2.3.1 Leucine Dependent Co-localization of LRS and LAMP2 in Confocal Images

To observe LRS translocation to the lysosome, LRS and lysosomes were labeled with anti-LRS–Alexa 488 and anti-LAMP2–STAR 635P. LRS (green) and LAMP2 (white) in HeLa cells incubated in the absence of leucine (–Leu) and the presence of leucine (+Leu) were observed using confocal microscopy (Figure 2.6a). The co-localized pixels where LRS and LAMP2 overlap are shown in blue for easy identification. Co-localization demonstrates that LRS transfers directly to the lysosome in the presence of leucine.

To quantify the co-localization of LRS and LAMP2, the ECF was used, which can determine the degree of overlap between the two signals regardless of the absolute amount of the signal. The ECF that obtained as described in

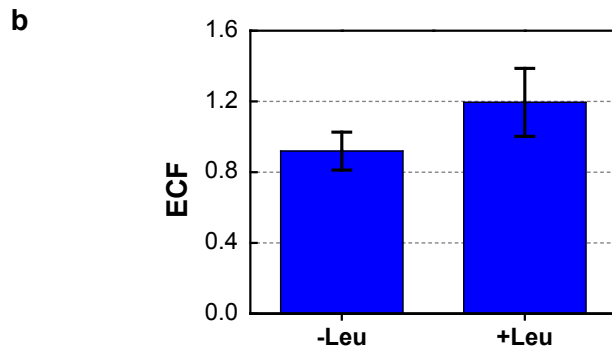
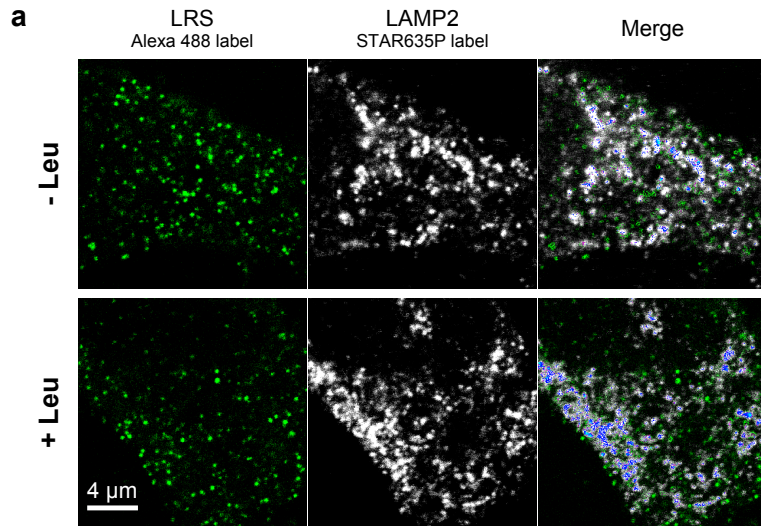


Figure 2.6 Location of intracellular LRS in absence or presence of leucine (-Leu, +Leu). (a) LRS (green) and LAMP2 (white) are labeled with Alexa 488-conjugated and STAR633P-conjugated secondary antibodies, respectively. Co-localization of the two proteins results in a blue color in the merged image. (b) Quantification of the co-localization between LRS and LAMP2 was performed with the ECF value (-Leu, +Leu). The error bar means the standard deviation for 12 images. LRS translocates to the lysosome in the presence of leucine.

Section 2.2.4 were 0.9190 ± 0.107 (mean \pm SD) in leucine-deficient media and 1.193 ± 0.193 in leucine-sufficient media (Figure 2.6b). Standard deviation was from measurements with 12 images. The results demonstrated a significantly higher ECF in leucine-sufficient group than that in leucine-deficient group. The ECF larger than 1 means that there is effective interaction between LRS and lysosome in leucine-sufficient media.

The results clearly showed that LRS translocates to the lysosome after the addition of leucine. These results are consistent with previous reports that LRS binds to Rag GTPase in the lysosome and activates mTORC1 in the presence of leucine [42].

2.3.2 LRS Translocation to the Lysosomal Membrane in STED Images

Confocal images only provide approximate location information of LRS and lysosome due to their diffraction limit. In order to investigate the detailed position of the intracellular LRS in the lysosome, an improvement in resolution is required. We used the STED microscopy for observing LRS and LAMP2 in the presence of leucine (Figure 2.7). In the enlarged images in Figure 2.7b white, the hollow membrane structure of the lysosome that cannot be resolved in confocal images is observed [58]. Because LAMP2 was stained in the lysosomal membrane, the membrane could be distinguished from the interior of the lysosome.

We observed that LRS is located on the lysosomal membrane and not inside the lysosome. The co-localized pixels (blue) in the confocal image is large and fuzzy, so that it provides only co-localization information, not exact locational information; On the other hand, STED image provides accurate locational information with a better resolution.

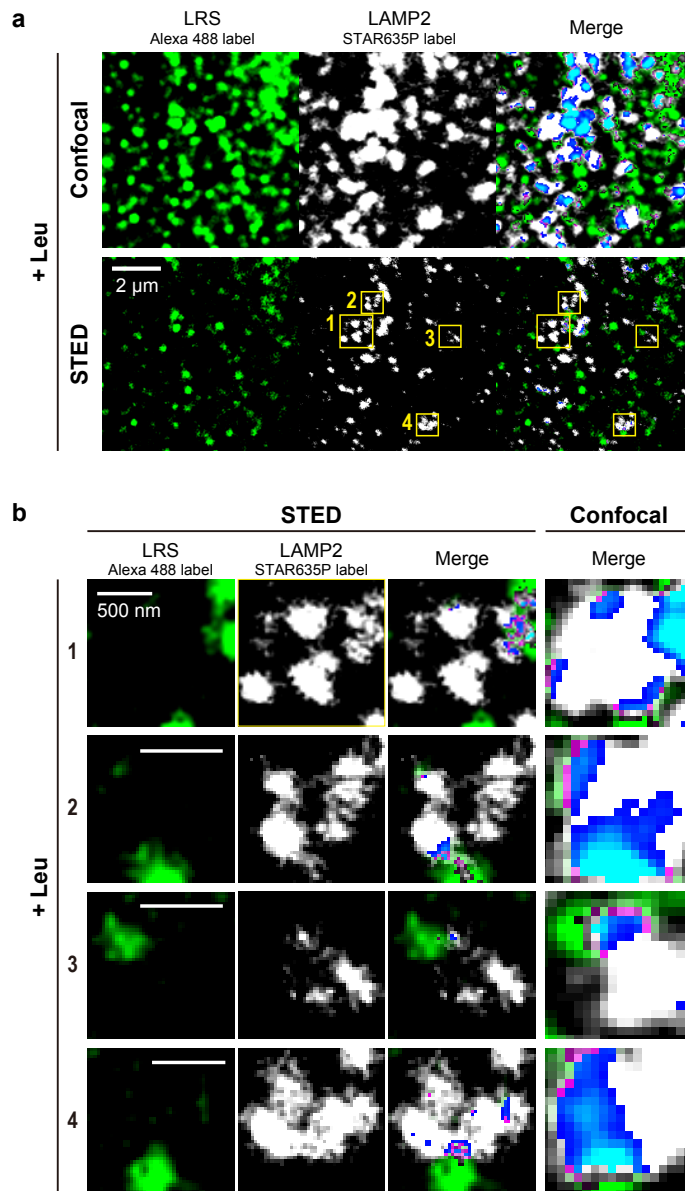


Figure 2.7 Confocal and STED images of LRS (green) and LAMP2 (white) in sufficient leucine condition (+Leu). (a) Confocal and STED images of the same region of HeLa cells were obtained. The yellow squares (1-4) are enlarged in (b). In STED images, hollow structures of the lysosome are resolved and LRS locates on the lysosomal membrane.

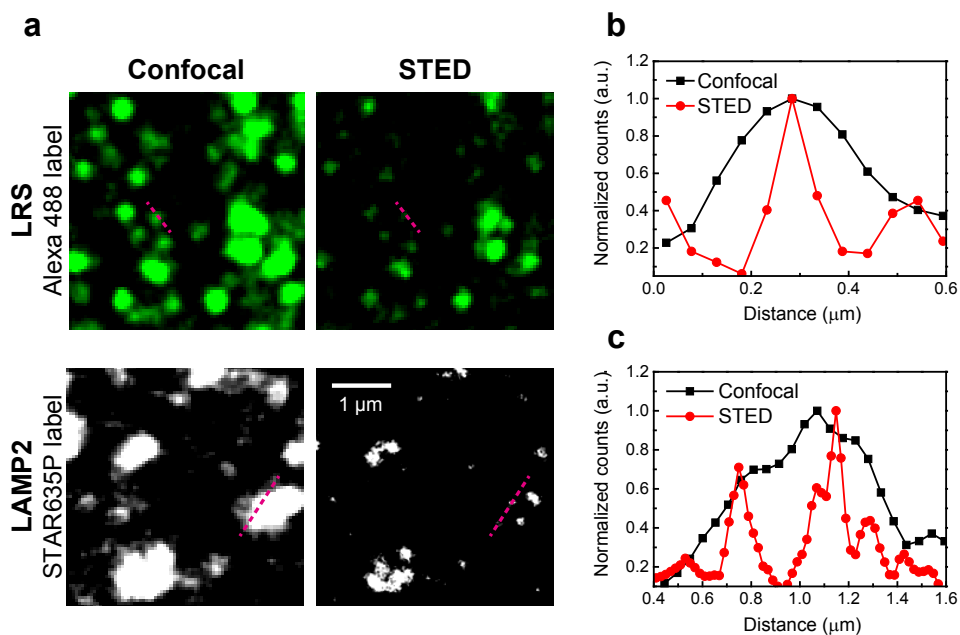


Figure 2.8 Intensity line profile of confocal and STED images. (a) Confocal and STED images of LRS labeled with Alexa 488 and LAMP2 labeled with STAR 635P. (b) Corresponding line profile of the pink line in (a) LRS. (c) Corresponding line profile of the pink line in (a) LAMP2. Line profiles of STED image (red) can resolve the different signals compared to that of confocal image (black)

LRS was detected on the lysosomal membrane with an improved resolution of STED microscope. Figure 2.8b and c show the line profiles of confocal and STED images of LRS and LAMP2. The STED line profile has ~ 80 nm resolution while the confocal line profile has ~ 1 μm resolution (Figure 2.8). (The line profiles were fitted by Lorentz function.) With STED image, we resolved two separated peaks which are indistinguishable in confocal images .

We not only confirmed the correlation between LRS and lysosome, but also provided the evidence of the interaction between RagD and LRS by determining the exact location of the LRS. In the presence of amino acids, LRS translocates to the lysosomal membrane, where it interacts with and facilitates GTP hydrolysis of RagD, which is required for mTORC1 activation.

2.4 Conclusion

LRS plays major roles in providing leucyl-tRNA and activating mTORC1 through intracellular leucine sensing. mTORC1 activated by amino acids affects the influence on physiology functions including cell proliferation, protein synthesis and autophagy in various organisms. Biochemical results demonstrating leucine sensing have been published, but visual results are lacking. In order for LRS to interact with RagD, LRS should be present on the membrane of the lysosome, but there was no direct experimental results. We observed the location of LRS with or without leucine using super resolution fluorescence microscope. Leucine induces the movement of LRS to lysosome, leading to mTORC1 activation. We revealed that LRS is located on the lysosomal membrane, not inside the lysosome, on addition of leucine. This direct visualization reveals the mechanism of LRS to activate the mTORC1. LRS is as an intracellular leucine sensor and positive regulator of amino acid signaling to mTORC1.

Chapter 3

Flexibility of Single-stranded DNA Measured by Single-molecule ALEX-FRET

3.1 Introduction

Single-stranded DNA Structure

Single-stranded DNA (ssDNA) plays an essential role in various DNA metabolic processes such as replication [72], transcription [73], and DNA repair [74] that involve many proteins. Nucleic acids in the cell nucleus undergo dynamic structural changes as they hand over their genetic information. It is therefore important to understand the structural properties of ssDNA, especially when it binds with proteins. The study of ssDNA flexibility can also provide clues to the RNA folding structure because of structural similarity of the RNA and DNA backbone [75].

The flexibility of ssDNA has been demonstrated by various spectroscopy methods, such as fluorescence correlation spectroscopy [76], single-molecule

FRET (fluorescence resonance energy transfer) [77, 78], and force spectroscopy [79–81]. The flexibility of long ssDNAs (> 100 nucleotides) has been widely investigated [82], but studies on shorter ssDNAs (< 15 nucleotides) are limited [77, 83, 84] since it is difficult to quantify the structural changes in ssDNA at the correspondingly short length scale. When proteins interact with DNA, they often interact with only a small number of nucleotides, the information of the flexibility of short ssDNA is very important. For example, the RNA polymerase interacts with promoter DNA through a single-stranded transcription bubble formed from ~ 14 nucleotides [85]. In this study, we directly measure the mechanical flexibility of ssDNA in short lengths.

DNA structures are affected by cations that can reduce electrostatic repulsion between the negatively charged phosphate groups of the DNA backbone. These ions can directly bind to DNA or change the dielectric characteristics of the medium. Divalent cations are known to be particularly effective in stabilizing the DNA structure [86] compare to monovalent cations. The effect of metal ions in nucleic acid structure has been widely investigated both theoretically and experimentally [76, 87]. In the present study, we investigated the change of ssDNA structure depending on the concentration of monovalent and divalent cations.

The Application of Single-molecule FRET Technique

Analysis of structure and dynamics of biomolecules is fundamental for understanding biomolecular mechanisms; a powerful method that can perform such an analysis is FRET [28, 88–91]. Various kinds of biomolecular processes have been investigated using FRET between two fluorescent probes. FRET is a phenomenon in which energy is transferred from a donor molecule to an acceptor molecule through non-radiative dipole-dipole coupling [29, 31, 92]. The energy

transfer efficiency is inversely proportional to the sixth power of the inter-probe distance and is very sensitive to the changes in the distance on the length scale of 1–10 nm. (See Section 1.5.2 for detailed information.)

The application of FRET phenomenon has been drastically increased by combining with the development of single-molecule detection technique. Since the first paper on single-molecule detection is published [93–96], single-molecule spectroscopy has been widely used in biological applications. Single-molecule detection makes it possible to observe changes in the absolute value of a single-molecule while avoiding ensemble averaging. For this reason, single-molecule FRET spectroscopy has been widely used as a spectroscopic ruler to analyze biomolecular structures.

Various single-molecule FRET techniques have been developed, however, conventional single-molecule FRET cannot distinguish changes in molecular stoichiometry from conformational changes. To overcome such limitations, the new platform of alternating laser excitation (ALEX)-FRET was introduced that employs an additional excitation laser to directly probe acceptor dye [97,98].

By alternating multiple lasers rapidly, the presence of each fluorophore on the distinct molecular compartment can be identified, which yields an independent parameter for molecular stoichiometry for compositional information in addition to the FRET efficiency for spatial information. By sorting molecules in 2-D E - S histogram along two independent parameters, i.e., FRET efficiency (E) versus stoichiometry ratio (S), molecular heterogeneities can be directly visualized along with their structural differences.

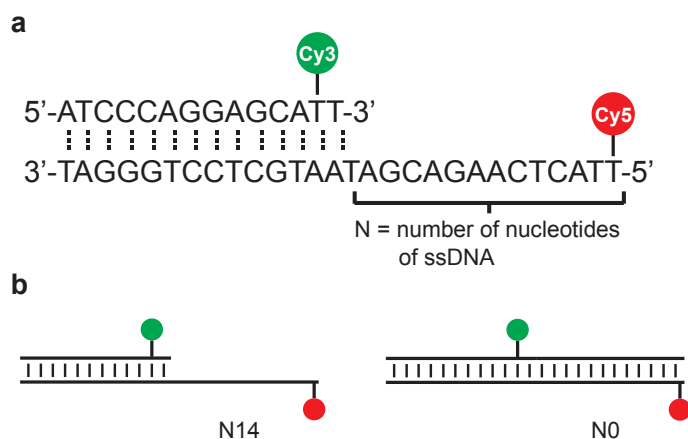


Figure 3.1 Sample design for studying the flexibility of ssDNA. (a) Sample design showing the dye labeling of two fixed sites separated by 14 nucleotides. N represents the number of nucleotides in the ssDNA segment called ‘overhang’ and is adjusted by varying the length of the upper strand labeled with Cy3. (b) N14 (left) and N0 (right) with each dye labeling the same position.

3.2 Materials and Methods

3.2.1 ssDNA Preparation

The scheme for our sample design is shown in Figure 3.1. We purchased nucleic acid samples from Integrated DNA Technologies (IDT). HPLC-purified sample was labeled with Cy3 and Cy5 on the shorter and longer strands, respectively, as shown in Figure 3.1a. The amino modifier C6 and C3, which is known to have only a slight effect on their configurations was used to link the dyes and DNA. The dye labeling sites are fixed at a specific position on each strand with a separation of 14 nucleotides between the dyes. We controlled the length of the overhang (the ssDNA segment) by varying the length of the shorter DNA from 14 to 28 nucleotides, giving the overhang a length of 14 to 0 nucleotides (Figure 3.1b). If we were to label the dye on the 3’ end of the shorter DNA, it

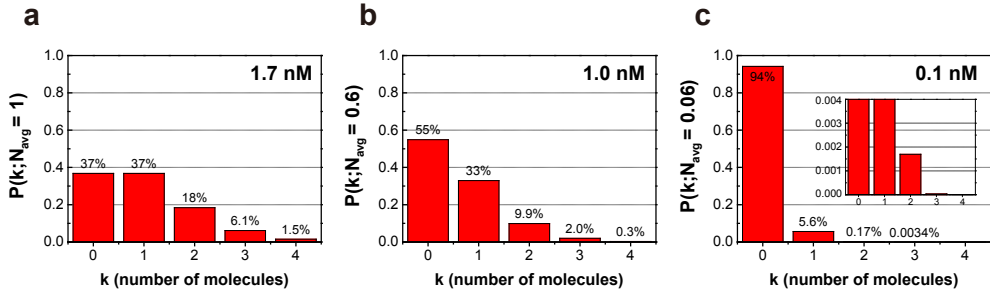


Figure 3.2 Poisson distribution of the number of molecules according to concentrations ((a) 1.7 nM, (b) 1.0 nM, and (c) 0.1 nM). (c) When the average number of molecules is 0.06 (100 pM), the probability of 0, 1, and 2 molecules in the observation volume is 94%, 5.6%, and 0.17%, respectively.

would have been difficult to see whether the overhang bends or not, especially at small N .

In our single molecule experiment, we used a DNA concentration of 100 pM to make sure that at most only one molecule was present in the observation volume within the detection time window of 600 μ s. The number of molecules in detection volume follows a Poisson distribution because the events occur independently of time since the last event [99, 100]. The average value was used to calculate a theoretical Poisson distribution, $P(k; N_{avg})$ which is

$$P(k; N_{avg}) = \frac{N_{avg}^k e^{-N_{avg}}}{k!} \quad (3.1)$$

where N_{avg} is the average number of molecules in observation volume (confocal volume used in this work is about 1 fL ($= 1 \mu m^3$)), k is the particular number of molecules and takes values 0, 1, 2, \dots .

The calculated probability, $P(k; N_{avg})$, is represented in Figure 3.2 when $N_{avg} = 1, 0.6,$ and 0.06 . “ $N_{avg} = 1$ ” means $(1/6.022 \cdot 10^{23})$ mole/1 fL ≈ 1.7 nM.

In the same way, $N_{avg} = 0.6$ and 0.06 mean 1.0 nM and 0.1 nM, respectively. When the molar concentration is 100 pM, $P(k > 2; N_{avg} = 100 \text{ pM})$ is 0.17% and $P(k = 0; N_{avg} = 100 \text{ pM})$ is 94% . This means that no molecules are observed for most of the time. The concentration of the sample should be lower than 100 pM to observe only single molecule.

The DNA was diluted with the buffer that contains 50 mM pH 8 Tris, 1 mM MEA, 5 vol% glycerol, and 1% BSA. The single molecule buffer reduces photobleaching and photoblinking, slows the diffusion rate, and inhibits the non-specific binding of the observed molecules. The salt concentration was varied from 10 mM to 2 M to investigate structural changes by cation.

3.2.2 Experimental Setup for ALEX-FRET

We obtained our ALEX-FRET data using a home-built fluorescence confocal setup (Figure 3.3). Two CW excitation lasers (532 nm: Samba™ 532, Cobolt; 635 nm: TECRL-25G-635, World Star Tech) were alternatively irradiated on the diffusing sample. Alternation of two lasers was achieved using an acousto-optic tunable filter (AOTF, AOTFnC-VIS, AA Opto-Electronic) running at $50 \mu\text{s}$ period. To avoid the temporal cross-talk, the “on” time of the AOTF was limited to $45 \mu\text{s}$, while $5 \mu\text{s}$ remained as the “off” time. After individual lasers passed through a polarization maintaining single-mode fiber (P1-488-PM-FC and P1-630PM-FC, Thorlabs) for beam cleanup, they were combined with dichroic mirrors ($488/532/633\text{rdc}$, Chroma). Lasers were circularly polarized to efficiently excite the dyes using half-wave plate and quarter-wave plate (RAC 3.2.15 and RAC 3.4.15, B. Halle). Lasers excite the sample on an objective (UplanSApo 60x/1.20 w, Olympus). Fluorescence signals from donor and acceptor were separated by a dichroic mirror (630dcxr , Chroma) and detected by two avalanche photodiodes (APDs) (SPCM-AQR-14, Perkin Elmer). We adjusted

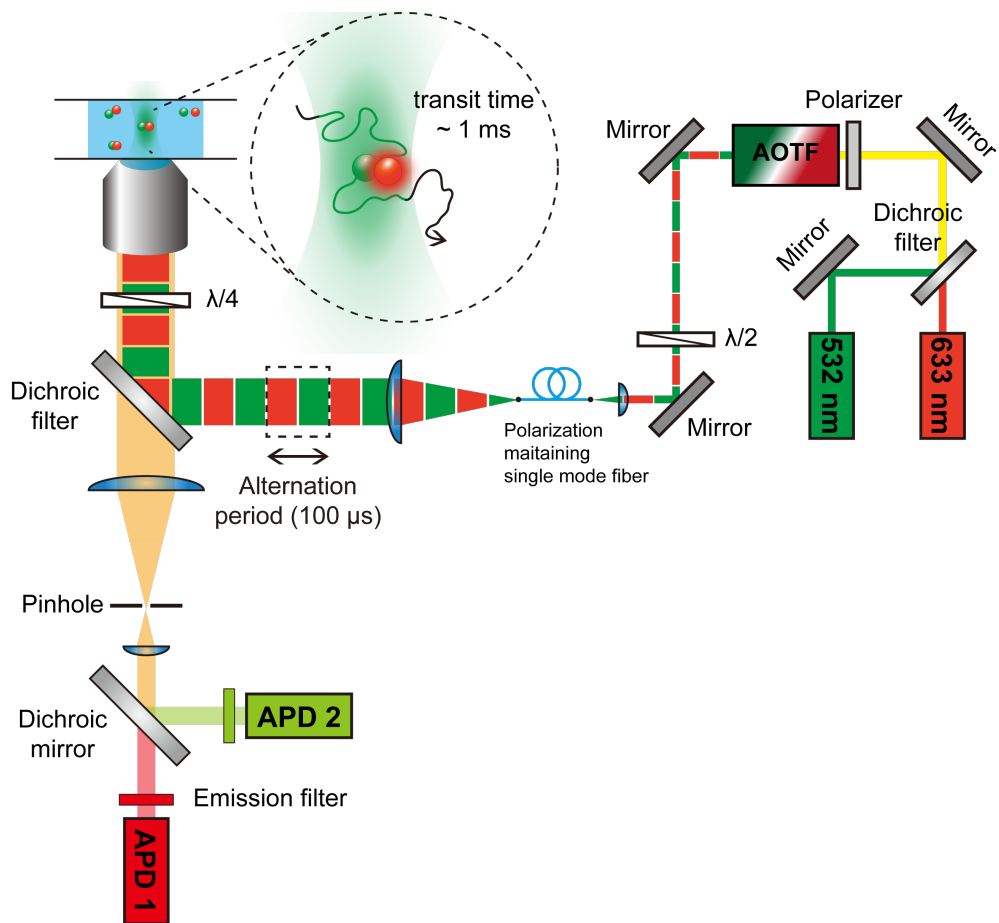


Figure 3.3 Experimental setup for ALEX-FRET. The enlarged circle represents an diffusing molecule in observation volume. (AOTF: acousto-optic tunable filter, APD: avalanche photodiode)

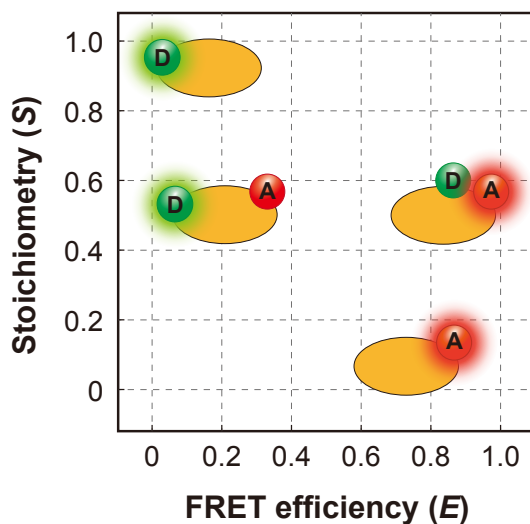


Figure 3.4 Molecular sorting based on E - S histogram. D-only, A-only, low FRET D-A pair, and high FRET D-A pair are clearly distinguished.

the laser power so that the S value is at 0.5 when there is one donor and one acceptor. The raw data were acquired and analyzed with LabVIEW program (NI6602 and NI6713, National Instruments)

3.2.3 ALEX-FRET Data Analysis

E - S Histogram

ALEX-FRET is a technique to excite the donor and the acceptor separately using two lasers, and it is possible to obtain not only the FRET efficiency (E) value, but also the stoichiometry (S) values of two molecules. The values of E and S were calculated from the photon traces detected by APD using the following equations:

$$E = \frac{F_D^A}{F_D^A + \gamma F_D^D} \quad (3.2)$$

where F_X^Y means the fluorescence intensity of Y fluorophore when X fluorophore is excited. (e.g., F_D^A is fluorescence intensity of acceptor channel when green laser is turned on to excite the donor dye.) $\gamma = \Phi_A \eta_A / \Phi_D \eta_D$, a normalizing the difference in quantum yields (Φ) and the detection efficiencies (η) for donor and acceptor molecules (See Section 1.5.2).

$$S = \frac{F_D}{F_D + F_A} \quad (3.3)$$

where F_X means the total fluorescence intensity when the laser that can excite X fluorophore is turned on. The donor excitation laser excites the donor so that the donor emits fluorescence or the acceptor emits fluorescence through the FRET. That is, $F_D = F_D^A + \gamma F_D^D$, and $F_A = F_A^D + F_A^A \approx F_A^A$ because F_A is caused only by the acceptor.

$$\begin{aligned} \text{For donor-only, } S &= \frac{F_D}{F_D + F_A} = \frac{F_D}{F_D + 0} = 1 \\ \text{For acceptor-only, } S &= \frac{F_D}{F_D + F_A} = \frac{0}{0 + F_A} = 0 \\ \text{For donor-acceptor pair, } S &= \frac{F_D}{F_D + F_A} = \frac{F_D}{F_D + F_D} = 0.5 \end{aligned} \quad (3.4)$$

It is assumed that the intensity of total fluorescence by each laser is the same. We can construct the 2-D E - S histogram using the above equations, where x -axis is FRET efficiency (E), and y -axis is stoichiometry (S) (Figure 3.4).

ALEX-FRET is particularly useful when dual labeling is not perfect. It cannot be distinguished by E value whether the donor exists only or the FRET value is 0 due to the distance between the donor and the acceptor. The S value can be used to identify between the two cases.

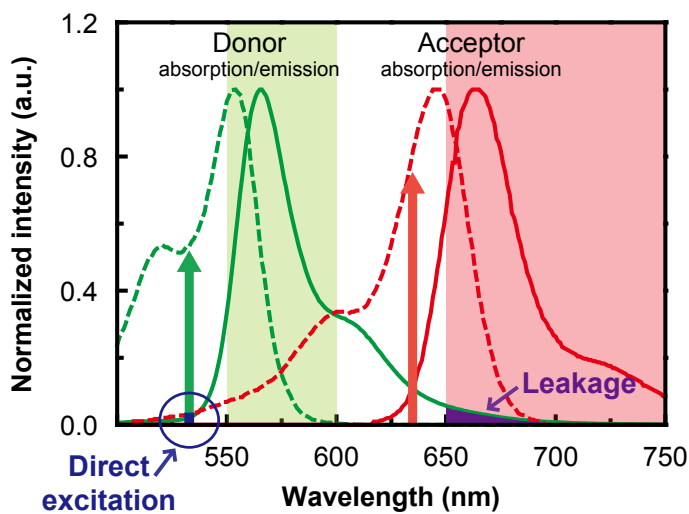


Figure 3.5 Absorption and emission spectra of Cy3 (donor) and Cy5 (acceptor) and their crosstalk. A green and red arrows indicate the wavelength of lasers to excite D and A, respectively. A green and red background squares imply the detection wavelength of D and A, respectively. Unwanted direct excitation of acceptor (blue) and leakage of donor emission (purple) are also expressed.

Accurate FRET Measurement

To measure accurate FRET efficiencies and distances from single molecules, we should correct the crosstalk between the donor and the acceptor [98]. Figure 3.5 shows two main crosstalk terms, direct excitation (*Dir*) and leakage (*Lk*). *Dir* is defined that the donor excitation laser is partially absorbed by the acceptor molecule; *Lk* means that the part of donor emission is detected by acceptor channel. Most FRET-capable donor-acceptor pairs naturally have the crosstalk.

$$\begin{aligned} F_D^A &= {}^D F_D^A + {}^A F_D^A + {}^{D \rightarrow A} F_D^A \\ &= Lk + Dir + \text{FRET} \end{aligned} \tag{3.5}$$

The upper superscript at left indicates the type of probe. D→A is the fluorescence generated from acceptor after energy transfer. F_D^A contains other contaminated signals such as *Lk* and *Dir* as well as the FRET signal. We could obtain the crosstalk by ALEX experiments. The ALEX measurements of donor-only sample and acceptor-only sample tells us *Lk* and *Dir*, respectively. We have to calibrate the crosstalk every measurement because it depends on instrumental factors such as excitation intensity and detector alignment.

3.3 Results and Discussion

3.3.1 Flexibility of ssDNA with 3-nucleotides

In ALEX FRET, a 2-D *E-S* histogram represents different subgroups of sample that has a heterogeneous distribution in chemical composition and molecular structure. Figure 3.6a shows a 2-D *E-S* histogram with four distinct (*E*, *S*) domains that may represent possible configurations of species expected from our sample. Doubly labeled species that have an intermediates *S* value can be readily distinguished from both singly labeled “impurities” that result from

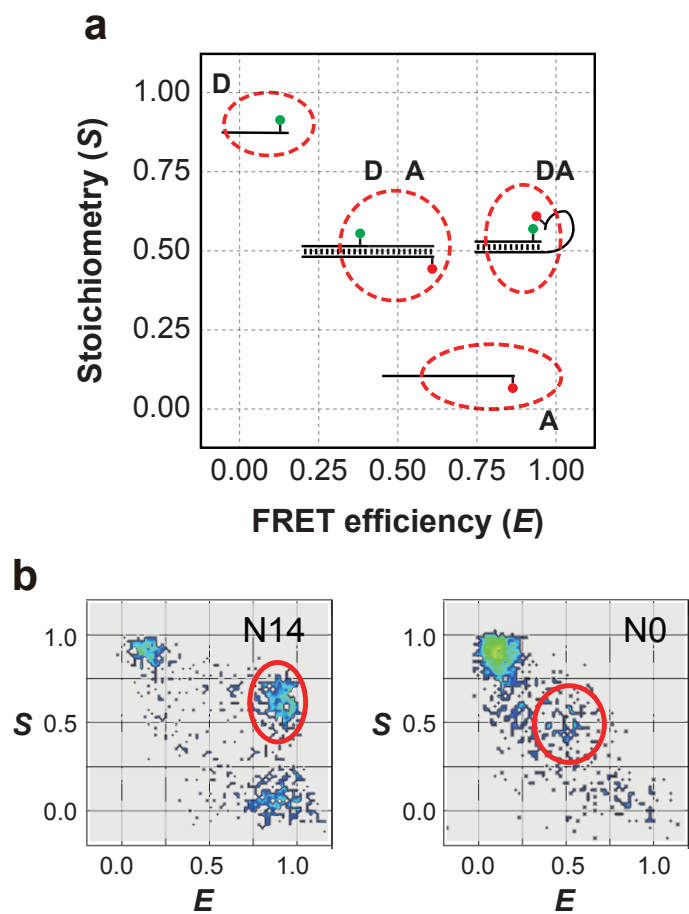


Figure 3.6 Experimental E - S histograms of ssDNA overhang. (a) Two-dimensional E - S histogram representing different domains of (E , S) values anticipated for four different subgroups of our sample: donor-only impurities with $S \sim 1$, acceptor-only impurities with $S \sim 0$, and doubly labeled species ($S \sim 0.5$) that are more flexible (high E) or less so (low E). (b) Experimental E - S histograms for N14 (left) and N0 (right) obtained at 2 M NaCl. Red circles represent the doubly labeled species with $S \sim 0.5$ that are the subject of our interest.

partial bleaching of fluorophores or failure of hybridization. The latter may further branch into those flexible enough to bring the two fluorophores together to yield a large E value and those not flexible enough. The minimum E value is expected to occur for N0 (i.e., double-stranded DNA or dsDNA). Since the persistence length of dsDNA is 50 nm [101], the 15-bp segment between the fluorophores should remain straight at a length of ~ 5 nm. Since Förster radius of Cy3-Cy5 pair is also ~ 5 nm, the expected minimum E value is about 0.5 from our experiments. Those with ssDNA overhang should have a higher E value since the two fluorophores can be brought closer due to its flexibility. Figure 3.6b shows two representative single-molecule ALEX FRET data for N14 (left) and N0 (right) collected from a large number ($> 1,000$) of DNA molecules at 2 M NaCl. The value of E was determined by fitting the peak at $S \sim 0.5$ to a Gaussian distribution and taking its center value. The E value of N14 was 0.944, representing a strongly curved structure of DNA while that of N0 was 0.541, indicating that dsDNA indeed has a rigid structure.

3.3.2 ssDNA in Various Ion Concentration

The averaged FRET efficiencies for overhangs of different lengths obtained under different ion concentrations are given in Figure 3.7. Any salt effect observed here is due to its effect on the DNA structure since the dye properties are hardly affected by salt conditions [77].

Figure 3.7 shows that, for instance, N0 and N3 have different FRET values. The E value of N3 is much higher than that of N0 even though the fluorophores are labeled on the same positions in N0 and N3. It indicates that sufficient flexibility is introduced with only 3 nucleotides of ssDNA. Since ssDNA may fluctuate freely during the detection time window of 600 μ s, we use the contour length of ssDNA that represents its length at maximum physically possible

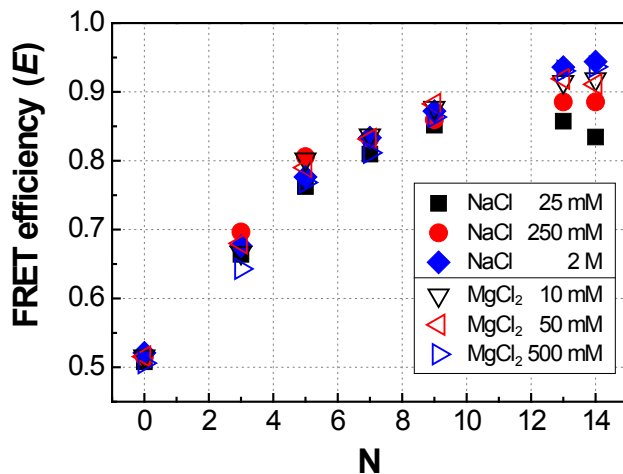


Figure 3.7 Average FRET efficiency values for different lengths of ssDNA ($N = 0-14$) in various concentrations of NaCl and MgCl₂.

extension. The contour length of N_3 is estimated to be 1.89 nm since the unit length of each base is well known to be 0.63 nm [102, 103]. This shows clearly that a ssDNA shorter than its persistence length can still bend. (The persistence length of ssDNA was reported to range from 2 to 5 nm, depending highly upon the ion concentration of the buffer [77].)

DNA structure is influenced by cations that screen the negatively charged phosphate backbone, perhaps more strongly for ssDNA than for dsDNA because of the higher flexibility of the former. In this study, we also examined the difference in the salt effect between monovalent and divalent cations by employing NaCl and MgCl₂.

For Na⁺ cation, our result shows that, for smaller N , there is little dependence of E on the cation concentration because the ssDNA structure is still not very flexible. For larger N ($N > 9$), however, E is significantly influenced by the

cation concentration, increasing as the cation increases.

At an intermediate concentration of Na^+ (250 mM), the E values of N9, N13, N14 are all comparable and seem to have reached a plateau, indicating that the flexibility does not increase even for longer overhangs at this cation concentration, which may not be sufficient to screen all negative charges. When we use a higher concentration (2 M) of Na^+ , however, the E value increases beyond the plateau since the flexibility of the overhang is enhanced again by further screening of the excess negative charges. By also looking at the data for the lowest Na^+ concentration (25 mM), we can see that it takes a certain amount of cations to sufficiently screen the negative charges of the backbone to make it flexible enough.

In the case of MgCl_2 , we observed little concentration dependence. Since the E values obtained for various concentrations of Mg^{2+} are also comparable to that for 2 M Na^+ , we think that the ssDNA is made flexible enough by the divalent cation even in its low concentration. This indicates that a divalent cation has a much stronger screening effect toward neutralization of the negative charges on the DNA backbone.

3.4 Conclusion

We examined the flexibility of a short ssDNA overhang ranging in length from 0 to 14 nucleotides at various concentrations of NaCl and MgCl_2 . The distance between the fluorophores measured by single-molecule ALEX-FRET yielded information about the bending structure of ssDNA and its flexibility. We discovered that sufficient flexibility is introduced with only 3 nucleotides of ssDNA and that a ssDNA shorter than its persistence length can still bend. The flexibility of ssDNA is little affected by cations when its length is short but becomes

increasingly affected by cation concentration as its length is increased. The screening effect was much greater for a divalent cation than a monovalent one.

Chapter 4

Detection of Single Diffusing Molecule in Sub-diffraction-limit Volume by ALEX-FRET and STED Microscopy

4.1 Introduction

In the last two decades, single-molecule FRET techniques have provided much useful information about such biophysical problems without ensemble average as chemical kinetics, mechanical/photophysical dynamics, conformational changes, inter-/intra-molecular interactions, and molecular movements [94, 97, 104–107]. Since the FRET efficiency has a strong dependence on the distance between two fluorophores ($E \propto r^{-6}$), one can readily obtain one-dimensional spatial information [28, 29]. Despite its many advantages, however, use of the diffusion-based single-molecule technique has been restricted to dilute samples (with a concentration down to tens of pM) due to the diffraction-limited observation volume (typically ~ 1 fL with a conventional confocal microscope) [108]. Considering that many biomolecular interactions have a dissociation constant

larger than \sim nM [109], this certainly poses a grave problem in applying the diffusion-based single-molecule technique to such molecules.

Various methods have been developed to break the concentration barrier (observe a single-molecule in high concentration). Total internal reflection is broadly used to confine the detection volume to a depth of \sim 100 nm with evanescent wave [110]. Zero-mode waveguide, whose diameter is much smaller than the wavelength of the light used, is employed to generate an evanescent field with a penetration depth of tens of nm [111]. Convex lens induced confinement (CLIC) utilizes the small contact point of a plano-convex lens and coverglass, which can confine the z -axis dimension down to 5 nm [112]. Concentration-independent single-molecule spectroscopy (ciSMS) uses UV and visible light for reversible photo-switching of a fluorophore in high concentration of fluorescent protein [113]. Most of these techniques have been applied to only immobilized samples, which have a possibility to cause surface-induced perturbations in the presence of a high level of background.

ALEX-FRET spectroscopy, one of single-molecule techniques to measure FRET efficiency of freely diffusing molecules, was developed to overcome the limitations of conventional single-molecule FRET measurements [97]. By exciting the acceptor fluorophore as well as the donor fluorophore in an alternating way, one can obtain not only the spatial information (E) but also the stoichiometric information (S) regarding the fluorophore composition. As shown in Chapter 3, ALEX-FRET can measure four inter-fluorophore distances and their compositions [114,115].

In this work, we introduced a novel method for the detection of single diffusing molecules at high concentration by utilizing the stimulated emission depletion (STED) microscopy to effectively reduce the observation volume. STED was developed to overcome the optical diffraction limit ($\delta r = \lambda/2NA$, λ : wave-

length of the excitation light, NA: numerical aperture, Equation 2.2) in far-field optical microscopy. A doughnut-shaped depletion beam is used to switch-off the fluorophores in excited state to prevent them from emitting fluorescence, resulting in reduced observation volume [48]. STED microscope can be easily adopted to a confocal microscope with an additional light source and can be applied to many of fluorophores commercially available. Therefore, an optical spectroscopy technique in sub-diffraction limited observation volume has been introduced utilizing the fluorescence correlation spectroscopy [60]. We combined the STED microscopy technique and the alternating laser excitation spectroscopy for fluorescence resonance energy transfer (ALEX-FRET), one of the diffusion-based single-molecule spectroscopy, and observed a single diffusing molecule in highly concentrated solution (called ‘ALFRED’).

4.2 Materials and Methods

4.2.1 DNA Sample Preparation

As a model system to demonstrate the feasibility of ALFRED, we observed 30-base double stranded DNA (dsDNA) labeled with a FRET pair, DY510XL (Dyomics GmbH) and ATTO647N (Atto-Tec GmbH). 30-mer of single stranded poly-A and poly-T DNA oligomers (IDT) were used, whose bases at the end were amino-modified for the fluorophore labeling (5’ modified poly-T for DY510XL; 5’ modified poly-A for ATTO647N (low-FRET); 3’ modified poly-A for ATTO647N (high-FRET)). In order to efficiently deplete both of the fluorophores with a single depletion laser, we chose DY510XL that shows a large Stoke’s shift and broad emission spectrum. DY510XL and ATTO647N were labeled at the end of oligomers via simple click reaction in sodium borate buffer (pH = 8.3, 2 h, room temperature). Unreacted oligomers and fluorophores were

removed by high performance liquid chromatography (1100 series, Agilent Technologies) using the C18 reverse phase column (RPC C2/C18 ST 4.6/100, GE Healthcare). Each labeled single strand was annealed with its complementary strand by gently cooling the mixture from $> 90^{\circ}\text{C}$ to the room temperature.

DY510XL	Viscosity (mPa·s)	Lifetime (ns)	Photon counts (kHz)
0% PEG	1.002	0.5	35.4
30% PEG	7.215	1.51	360

ALEX-FRET and ALFRED measurements were carried out in the presence of 30% of poly(ethylene glycol) (PEG), triplet quencher (β -mercaptoethylamine, 1 mM) and salt (NaCl, 50 mM) in Tris buffer (pH = 8.0). PEG was used to increase the viscosity and diffusion time to get enough photons from the fluorophores traveling the reduced observation volume. Moreover the quantum yield of DY510XL notably increases in the viscous solution. The viscosity of intracellular cytoplasm is known to be 1.9–3.1 mPa·s, which is higher than the normal aqueous buffer solution [116, 117]. Finally, prepared sample was put on a cover glass sealed by silicon spacer (CoverWell Perfusion Chamber Gasket, ThermoFisher) to prevent sample evaporation during the measurement.

4.2.2 Experimental Setup for ALFRED

Our experimental setup is briefly shown in Figure 4.1, which is a combined setup of Section 2.2.3 and 3.2.2. Ti-sapphire laser (< 100 fs, 80 MHz, MaiTai HP, Spectra-Physics) is separated in two path, excitation and STED. 510 nm and 635 nm were selected for excitation of DY510XL and ATTO647N, and 780 nm is suitable for depletion of two fluorophores. Two excitation lasers were alternatively irradiated using an acousto-optic tunable filter (AOTF, AOTFnC-

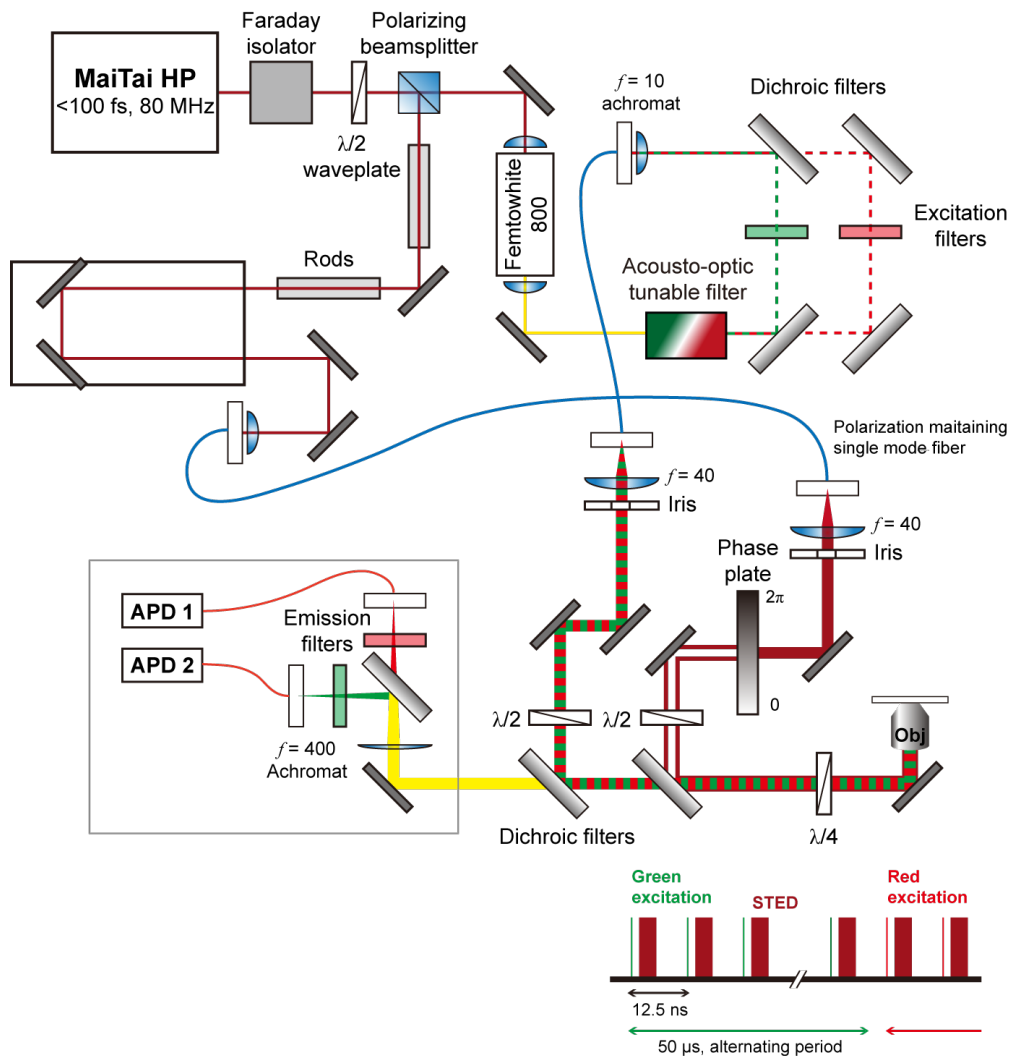


Figure 4.1 Experimental setup for ALFRED. The two excitation laser beams (510 and 635 nm) alternately irradiates the sample for 50 μs , while the doughnut-shaped STED beam (780 nm) depletes the fluorescence signal from outside its central hole confined at a sub-diffraction limit.

VIS, AA Opto-Electronic) running at 50 μ s period. To avoid the temporal cross-talk, the “on” time of the AOTF was limited to 45 μ s, while 5 μ s remained as the “off” time. For STED beam, 780 nm output of a Ti:Sapphire laser passed through the two glass rods and 100 m long fiber to be stretched to \sim 280 ps. STED beams passed through the phase plate (VPP-1a, RPC Photonics) to make a doughnut-shape beam at focal plane.

Two excitation beams (510, 635 nm) and STED beam (780 nm) are combined through dichroic mirrors and focused to the sample by an oil immersion objective (HCX PL APO 100X, 1.4 NA, Leica). They should be aligned in exactly same position at focal plane. Co-localization between excitation and STED beam was monitored by collecting scattered light from an Au bead with 80 nm diameter. STED beam was adjusted to irradiate the samples after 160 ps from the excitation to achieve the maximum depletion efficiency.

The fluorescence signals from donor and acceptor passed the pinhole to eliminate the backgrounds and divided by dichroic filter (ZT633drc, Chroma) and detected by two different APDs (SPCM-AQR-14-FC, Perkin Elmer). Some emission filters and notch filters were used to detect only each fluorescent signal. We adjusted the laser power so that the S value is at 0.5 when there is one donor and one acceptor. The raw data was analyzed with LabVIEW program (NI6602 and NI6713, National Instruments) as shown in Section 3.2.3. When only the excitation beam is irradiated, ALEX-FRET is measured in the diffraction-limited confocal volume, and ALFRED is measured in the reduced focal volume when STED beam is added.

Fluorescence correlation spectroscopy (FCS) is a technique that measures the time-dependent changes of fluorescence. FCS data were obtained with the correlator (Flex02-01D, Correlator.com), and the raw data were analyzed with LabVIEW program (National Instruments). Fitting of the FCS curve with the

autocorrelation function is described in Section 1.5.3. When we assume that only the random diffusion of the fluorophores results fluorescence fluctuation in our system, the autocorrelation function ($G(\tau)$) according to lag time (τ) is as follows:

$$G(\tau) = G(0) \left(1 + \frac{\tau}{\tau_{\text{Diff}}}\right)^{-1} \left(1 + \frac{s^2}{u^2} \frac{\tau}{\tau_{\text{Diff}}}\right)^{-1/2} \quad (4.1)$$

where $G(0)$ is the amplitude at $\tau = 0$, τ_{Diff} is diffusion time in observation volume and is inversely proportional to the diffusion constant (D). s and u are the radial radius and axial half-length of observation volume. τ_{Diff} and D are determined by least-squares fitting of the simulated curve with the measured data.

4.3 Results and Discussion

4.3.1 Observing Single-molecules in Reduced Focal Volume

To overcome the concentration limit in confocal, we apply an additional doughnut-shaped depletion laser, which effectively induces the stimulated emission of the excited fluorophores. This results further reduced observation volume, where much less fluorophores can be detected (Figure 4.2).

The final observation volume in ALFRED highly depends on the intensity of depletion laser. It is well known that the effective focal volume can be reduced proportionally to the square root of the depletion laser intensity (Equation 2.2). We plot a reference curve for the resolution and the STED beam power in the home-built STED microscope (Figure 4.3a). The resolution is obtained from full-width at half maximum (FWHM) value of the STED image of 20 nm fluorescent beads (FluoSpheres Carboxylate-Modified Microspheres, crimson fluorescent, Invitrogen). We obtain the $I_{\text{sat}} = 0.73 \text{ MW/cm}^2$ by interpolating the result with Equation 2.2, where the resolution equals to $r_0/\sqrt{2}$. The resolution

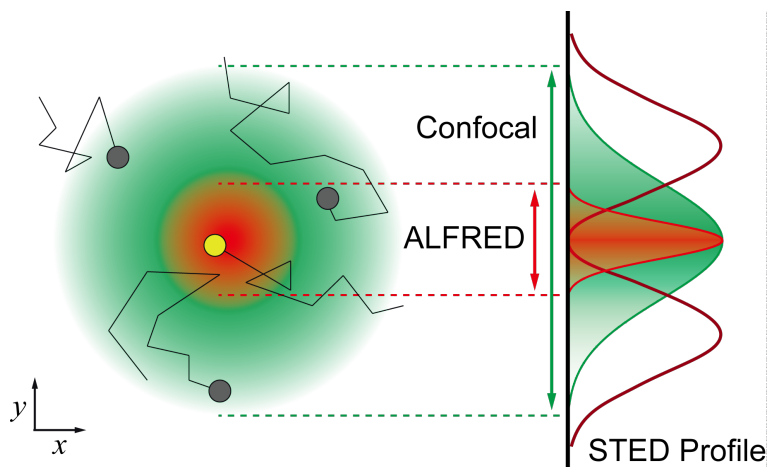


Figure 4.2 Conceptual illustration of ALEX-FRET-STED (ALFRED). The doughnut-shaped STED beam “erases” the fluorescence signal from outside its central hole. Although there exist a number of fluorophores in the diffraction-limited volume (green), only a single molecule can be detected in the reduced observation volume (red). A detection volume ~ 100 times smaller than the confocal volume allows a much higher sample concentration without compromising the single-molecule nature of the detection.

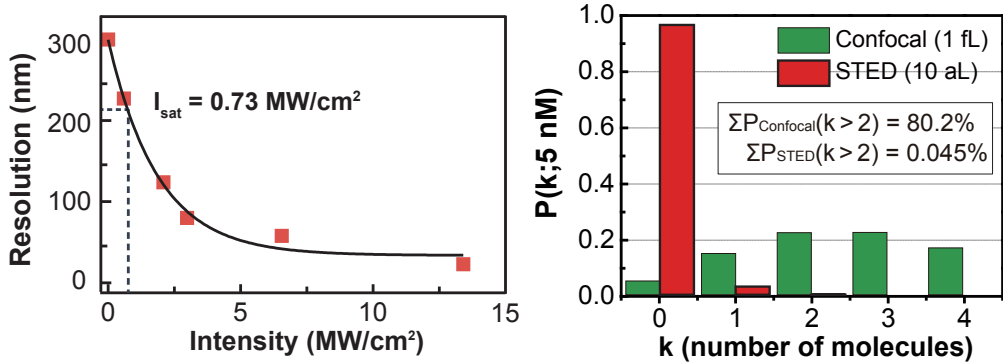


Figure 4.3 Focal volume reduction and subsequent change of Poisson distribution. (a) STED beam intensity (I) versus resolution (r). The saturation intensity (I_{sat}) is calculated as 0.73 MW/cm^2 at the focal plane. (b) Poisson distribution at 5 nM concentration in different observation volumes (green: confocal, red: ALFRED). With 10 aL observation volume, we can observe individual molecules in 5 nM solution.

is $\sim 23 \text{ nm}$ (at $I = 13.4 \text{ MW/cm}^2$), which is > 10 -times less than the resolution without the depletion laser ($\sim 300 \text{ nm}$). This result suggests that the concentration barrier in single molecule detection can be increased 100-times ($> 5 \text{ nM}$) in ALFRED measurement.

The probability that how many molecules exist in the observation volume at certain concentration is described by the Poisson distribution (Equation 3.1). Figure 4.3b shows the Poisson distribution of two different observation volumes, 1 fL (diffraction-limited observation volume, ALEX-FRET) and 10 aL (100 times reduced observation volume, ALFRED), at 5 nM concentration that is 100 -times higher than conventional condition (50 pM). In the diffraction-limited volume (1 fL), there exist more than two molecules with $> 80\%$ probability, where it reduces to $< 0.05\%$ with reduced observation volume (10 aL). Hence, the individual molecules are distinguishable even at high concentration if we successfully reduce the observation volume.

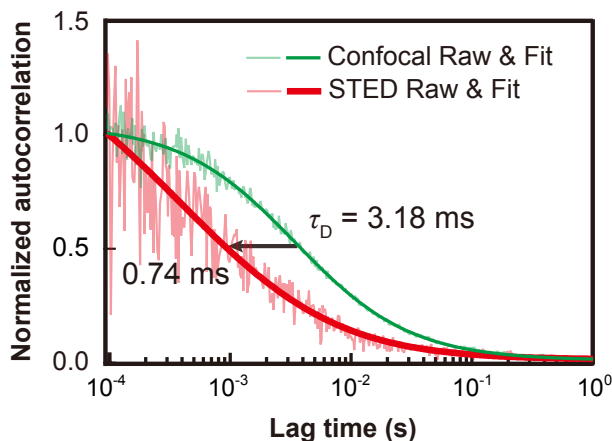


Figure 4.4 FCS results of ATTO647N labeled dsDNA in solution containing 30% of PEG (green: confocal, red: ALFRED). The diffusion time (τ_{Diff}) decreased to 0.74 ms when the depletion laser was applied.

We performed the FCS to evaluate the diffusion times (τ_{Diff}) of dsDNA in both of ALEX and ALFRED conditions (Figure 4.4), as well as the viscosity of 30% PEG solution ($\eta = 7.2$ mPa·s). In single-molecule spectroscopy, τ_{Diff} plays an important role when we use an intensity-based analysis method such as FRET. The longer binning time than the τ_{Diff} is required to obtain the accurate fluorescence intensity. Furthermore, the alternating periods of each excitation laser also should remain shorter than τ_{Diff} [118].

τ_{Diff} of dsDNA clearly decreases in ALFRED (3.18 ms \rightarrow 0.74 ms), suggesting that the observation volume is efficiently reduced. Based on the FCS results, the photon binning time is determined as 3.5 ms and 1.0 ms for the ALEX and ALFRED analysis, respectively (slightly longer than the diffusion times).

Figure 4.5 shows the fluorescence time trace of the dual-labeled dsDNA in 30% PEG solution at 5 nM concentration. The binning times are 3.5 ms for

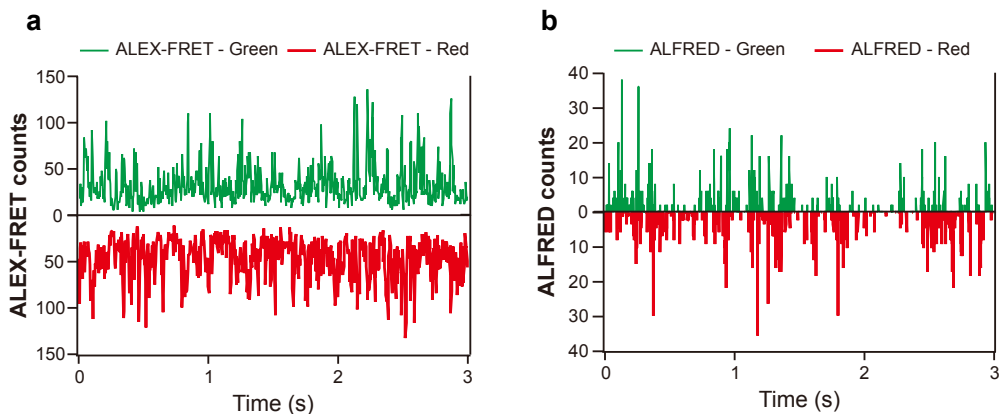


Figure 4.5 Fluorescence time trace of (a) ALEX-FRET and (b) ALFRED (5 nM dual-labeled dsDNA in 30% PEG solution). Bursts from single molecules observed by ALFRED (b) are not seen in the ALEX-FRET (a) because its focal volume contains too many molecules (above the line: F_D , below the line: F_A).

ALEX and 1.0 ms for ALFRED. Since there can exist more than two molecules in the diffraction-limited observation volume (ALEX-FRET), the time trace showed an average value with some stochastic fluctuations (Figure 4.5a). On the other hand, only one or no molecule can exist in the reduced observation volume (ALFRED) resulting the fluorescence ‘burst’ (Figure 4.5b). These bursts are regarded as the sum of the photons from the individual molecules, thus each burst can be analyzed to extract useful information from a single molecule.

4.3.2 *E-S* Histogram with ALEX-FRET and ALFRED

We test whether the ALFRED can distinguish the donor- and the acceptor-only samples in highly concentrated solution (Figure 4.6). ALEX-FRET and ALFRED are applied to samples at 100 pM and 1 nM, respectively. Clearly sorted results ensure the feasibility of our ALFRED system.

Figure 4.7 shows the 2-D *E-S* histogram of ALEX-FRET and ALFRED at

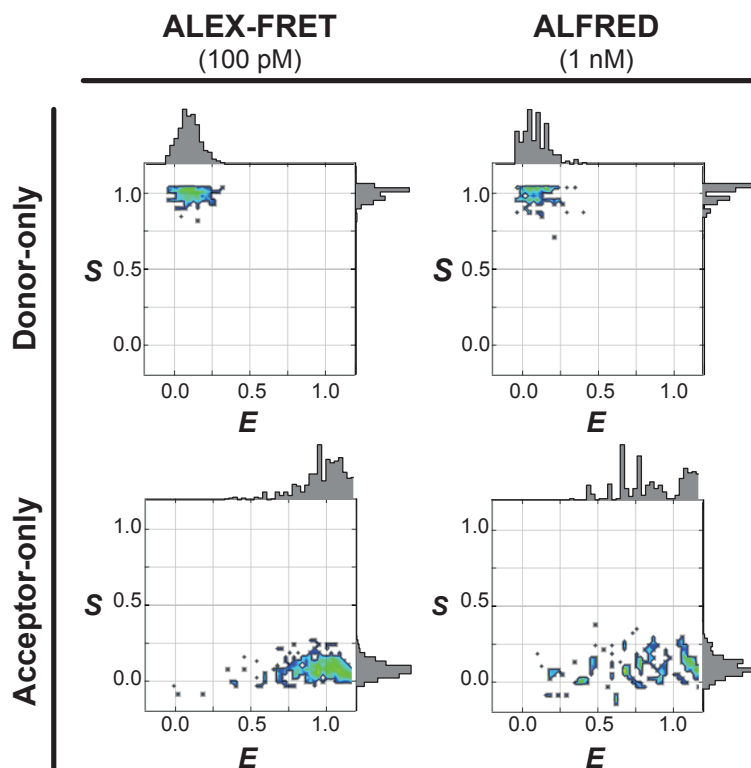


Figure 4.6 2-D E - S histogram of donor-only and acceptor-only samples measured by ALEX-FRET and ALFRED. ALEX-FRET examine samples in 100 pM concentrations, whereas ALFRED is applied to 1 nM of samples. D-only species appear near $S = 1$ and $E = 0$ position, but A-only samples appear in the bottom region of the histogram ($S = 0$). They are clearly coincident with each other, when proved the feasibility of ALFRED system.

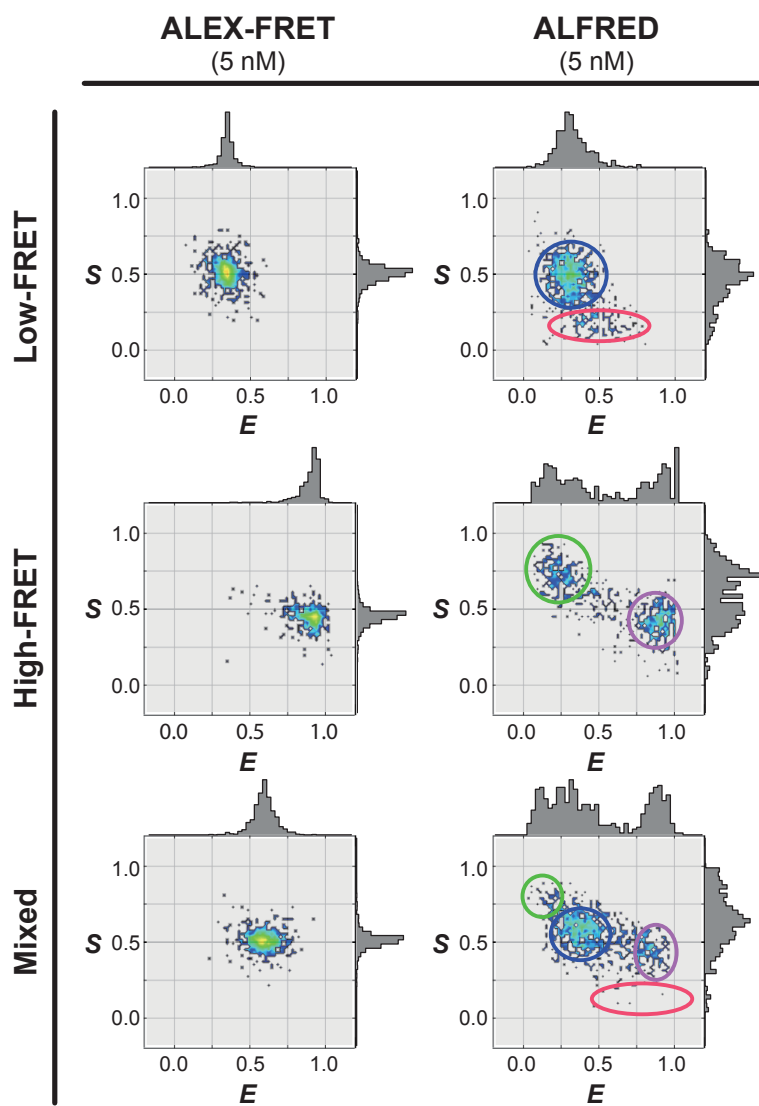


Figure 4.7 ALEX-FRET (left) and ALFRED (right) results of 5 nM dsDNA in 30% PEG solution. In 5 nM, several molecules exist in a confocal volume (ALEX-FRET), which give an unresolved ensemble-averaged distribution. In contrast, when the focal volume is reduced by ALFRED, only one diffusing molecule is detected during binning time. The signals from the D-only species (green circle), the A-only species (red circle), the low-FRET D-A species (blue circle), and the high-FRET D-A species (purple circle) are clearly resolved.

5 nM concentration. It is measured with the dual-labeled dsDNA having two different FRET states. E and S values were calculated from the fluorescent intensities collected in each binning time (Equation 3.2 and 3.3). We also calibrate the effects of the direct excitation (Dir) and emission leakage (Lk) from the photon counts, as well as the background noise, to evaluate the E and S values accurately.

In ALEX-FRET measurements, the signals came from several molecules having different fluorophore composition are collected together in the binning time, resulting the averaged FRET value in the histogram (Figure 4.7, left column). However, the reduced observation volume of ALFRED results in the detection of individual dsDNA molecules without the ensemble average (Figure 4.7, right column). ALFRED successfully resolved the donor- (green circles) and acceptor-only (red circles) molecules in the histogram as well as the dual-labeled molecules (blue and purple circles).

All the possible compositions of the sample are clearly appeared in the E - S histogram, but their standard deviations in distributions are larger than that in ALEX-FRET. The lower signal-to-noise ratio of ALFRED due to the smaller photon counts mainly contributes to this feature, which can be interpreted as a combination of two factors: i) reduction of the diffusion time, ii) photobleaching of the fluorophores during diffusion due to the intense depletion laser. Especially, the photobleaching during diffusion causes the dissymmetry of the photon counts from the donor and acceptor molecules, which induces much severe broadness effect to E and S values. In addition, highly populated features of the donor- and acceptor-only species in the ALFRED also can be explained by the photobleaching. Since the depletion laser surrounds the observation volume, STED-induced photobleached species are regarded as the solely labeled molecules.

4.4 Conclusion

In conclusion, we successfully combined ALEX-FRET single-molecule spectroscopy and super-resolution STED microscopy to confine the observation volume less than the diffraction-limited volume. We demonstrated the capability of our technique that can distinguish each individual fluorescent molecule in 5 nM concentration, which is 100-times increased concentration than that in conventional diffusion-based single molecule spectroscopy. Since this concentration is comparable with the dissociation constant of many enzymes, it will help us to investigate the biomolecules *in vivo* at the single-molecule level. The concentration limit of ALFRED is now restricted by the quantum yield and stimulated emission cross-section of the fluorophores, which can be overcome by developing proper fluorophores to enable the single-molecule detection in even higher concentration.

Bibliography

- [1] J. Michael Hollas. *Modern Spectroscopy*. John Wiley & Sons, 2004.
- [2] María-Magdalena Cid and Jorge Bravo. *Structure Elucidation in Organic Chemistry: The Search for the Right Tools*. John Wiley & Sons, 2014.
- [3] David Rendell and David J. Mowthorpe. *Fluorescence and Phosphorescence Spectroscopy*. Published on behalf of ACOL, London by Wiley, 1987.
- [4] Ashutosh Sharma and Stephen G. Schulman. *Introduction to Fluorescence Spectroscopy*, volume 13. Wiley-interscience, 1999.
- [5] Joseph R. Lakowicz. *Principles of Fluorescence Spectroscopy*. 2006.
- [6] Jihad René Albani. *Principles and Applications of Fluorescence Spectroscopy*. John Wiley & Sons, 2008.
- [7] Aleksander Jabłoński. Über den mechanismus der photolumineszenz von farbstoffphosphoren. *Zeitschrift für Physik A Hadrons and Nuclei*, 94(1):38–46, 1935.
- [8] Francis Perrin. La fluorescence des solutions-induction moléculaire.–polarisation et durée d'émission.–photochimie. *Annales de Physique*, 10(12):169–275, 1929.
- [9] Wolfgang Pauli. Über den zusammenhang des abschlusses der elektronengruppen im atom mit der komplexstruktur der spektren. *Zeitschrift für Physik A Hadrons and Nuclei*, 31(1):765–783, 1925.
- [10] James Franck and E. G. Dymond. Elementary processes of photochemical reactions. *Transactions of the Faraday Society*, 21(February):536–542, 1926.

- [11] Edward Condon. A theory of intensity distribution in band systems. *Physical Review*, 28(6):1182, 1926.
- [12] Michael Kasha. Characterization of electronic transitions in complex molecules. *Discussions of the Faraday Society*, 9:14–19, 1950.
- [13] George Gabriel Stokes. On the change of refrangibility of light. *Philosophical Transactions of the Royal Society of London*, 142:463–562, 1852.
- [14] James D. Ingle and Stanley R. Crouch. *Spectrochemical Analysis*. Old Tappan, NJ (US); Prentice Hall College Book Division, 1988.
- [15] Roger A. Lampert, Leslie A. Chewter, David Phillips, Desmond V. O'Connor, Anthony J. Roberts, and Stephen R. Meech. Standards for nanosecond fluorescence decay time measurements. *Analytical Chemistry*, 55(1):68–73, 1983.
- [16] Wolfgang Becker, Axel Bergmann, Giovanni L. Biscotti, and Angelika Rück. Advanced time-correlated single photon counting techniques for spectroscopy and imaging in biomedical systems. In *Proceedings of SPIE*, volume 5340, pages 104–112, 2004.
- [17] Wolfgang Becker. *Advanced time-correlated single photon counting techniques*, volume 81. Springer Science & Business Media, 2005.
- [18] Wolfgang Becker, H. Hickl, C. Zander, K. H. Drexhage, M. Sauer, S. Siebert, and J. Wolfrum. Time-resolved detection and identification of single analyte molecules in microcapillaries by time-correlated single-photon counting (TCSPC). *Review of Scientific Instruments*, 70(3):1835–1841, 1999.
- [19] Enrico Gratton, David M. Jameson, and Robert D. Hall. Multifrequency phase and modulation fluorometry. *Annual Review of Biophysics and Bioengineering*, 13(1):105–124, 1984.
- [20] W. Gärtner, B. Gröbler, D. Schubert, H. Wabnitz, and B. Wilhelmi. Fluorescence scanning microscopy combined with subnanosecond time resolution. *Experimentelle Technik der Physik*, 36(6):443–451, 1988.
- [21] I. Bugiel, K. König, and Heidrun Wabnitz. Investigation of cells by fluorescence laser scanning microscopy with subnanosecond time resolution. *Lasers Life Sciences*, 3(1):47–53, 1989.
- [22] Joseph R. Lakowicz, Henryk Szmajcinski, Kazimierz Nowaczyk, and Michael L. Johnson. Fluorescence lifetime imaging of free and protein-bound NADH. *Proceedings of the National Academy of Sciences*, 89(4):1271–1275, 1992.

- [23] Joseph R. Lakowicz, H. Szmacinski, K. Nowaczyk, W. J. Lederer, M. S. Kirby, and M. L. Johnson. Fluorescence lifetime imaging of intracellular calcium in COS cells using Quin-2. *Cell Calcium*, 15(1):7–27, 1994.
- [24] Fred S. Wouters and Philippe I. H. Bastiaens. Fluorescence lifetime imaging of receptor tyrosine kinase activity in cells. *Current Biology*, 9(19):1127–1130, 1999.
- [25] Peter J. Verwee, Fred S. Wouters, Andrew R. Reynolds, and Philippe I. H. Bastiaens. Quantitative imaging of lateral ErbB1 receptor signal propagation in the plasma membrane. *Science*, 290(5496):1567–1570, 2000.
- [26] Christopher D. Harvey, Ryohei Yasuda, Haining Zhong, and Karel Svoboda. The spread of Ras activity triggered by activation of a single dendritic spine. *Science*, 321(5885):136–140, 2008.
- [27] Ryohei Yasuda. Imaging spatiotemporal dynamics of neuronal signaling using fluorescence resonance energy transfer and fluorescence lifetime imaging microscopy. *Current Opinion in Neurobiology*, 16(5):551–561, 2006.
- [28] Theodor Förster. Zwischenmolekulare energiewanderung und fluoreszenz. *Annalen der Physik*, 437(1-2):55–75, 1948.
- [29] Robert M. Clegg. Fluorescence resonance energy transfer. *Current Opinion in Biotechnology*, 6(1):103–110, 1995.
- [30] Robert M. Clegg. Förster resonance energy transfer—FRET what is it, why do it, and how it’s done. *Laboratory Techniques in Biochemistry and Molecular Biology*, 33:1–57, 2009.
- [31] Lubert Stryer. Fluorescence energy transfer as a spectroscopic ruler. *Annual Review of Biochemistry*, 47(1):819–846, 1978.
- [32] Robert E. Dale, J. Eisinger, and W. E. Blumberg. The orientational freedom of molecular probes. The orientation factor in intramolecular energy transfer. *Biophysical Journal*, 26(2):161–193, 1979.
- [33] Elke Haustein and Petra Schwille. Fluorescence correlation spectroscopy: novel variations of an established technique. *Annual Review of Biophysics and Biomolecular Structure*, 36:151–169, 2007.
- [34] Petra Schwille. Fluorescence correlation spectroscopy and its potential for intracellular applications. *Cell Biochemistry and Biophysics*, 34(3):383–408, Jun 2001.
- [35] Huimin Chen, Elaine R Farkas, and Watt W Webb. In vivo applications of fluorescence correlation spectroscopy. *Methods in Cell Biology*, 89:3–35, 2008.

- [36] Jerker Widengren, Uelo Mets, and Rudolf Rigler. Fluorescence correlation spectroscopy of triplet states in solution: a theoretical and experimental study. *The Journal of Physical Chemistry*, 99(36):13368–13379, 1995.
- [37] Jerker Widengren and Rudolf Rigler. Mechanisms of photobleaching investigated by fluorescence correlation spectroscopy. *Bioimaging*, 4(3):149–157, 1996.
- [38] Nancy L. Thompson. *Fluorescence correlation spectroscopy*. Springer, 2002.
- [39] Rosa Puertollano. mTOR and lysosome regulation. *F1000prime reports*, 6, 2014.
- [40] Alejo Efeyan, Roberto Zoncu, and David M. Sabatini. Amino acids and mTORC1: from lysosomes to disease. *Trends in Molecular Medicine*, 18(9):524–533, 2012.
- [41] Mitsugu Shimobayashi and Michael N. Hall. Multiple amino acid sensing inputs to mTORC1. *Cell Research*, 26(1):7–20, 2016.
- [42] Jung Min Han, Seung Jae Jeong, Min Chul Park, Gyuyoung Kim, Nam Hoon Kwon, Hoi Kyoung Kim, Sang Hoon Ha, Sung Ho Ryu, and Sunghoon Kim. Leucyl-tRNA synthetase is an intracellular leucine sensor for the mTORC1-signaling pathway. *Cell*, 149(2):410–424, 2012.
- [43] Raúl V. Durán and Michael N. Hall. Leucyl-tRNA synthetase: double duty in amino acid sensing. *Cell Research*, 22(8):1207–1209, 2012.
- [44] Xu Zheng, Yan Liang, Qiburi He, Ruiyuan Yao, Wenlei Bao, Lili Bao, Yanfeng Wang, and Zhigang Wang. Current models of mammalian target of rapamycin complex 1 (mTORC1) activation by growth factors and amino acids. *International Journal of Molecular Sciences*, 15(11):20753–20769, 2014.
- [45] Yao Yao, Edith Jones, and Ken Inoki. Lysosomal regulation of mTORC1 by amino acids in mammalian cells. *Biomolecules*, 7(3):51–68, 2017.
- [46] Yasemin Sancak, Liron Bar-Peled, Roberto Zoncu, Andrew L. Markhard, Shigeyuki Nada, and David M. Sabatini. Ragulator-Rag complex targets mTORX1 to the lysosomal surface and is necessary for its activation by amino acids. *Cell*, 141(2):290–303, 2010.
- [47] Ernst Abbe. Beiträge zur theorie des mikroskops und der mikroskopischen wahrnehmung. *Archiv für Mikroskopische Anatomie*, 9(1):413–418, 1873.
- [48] Stefan W. Hell and Jan Wichmann. Breaking the diffraction resolution limit by stimulated emission: stimulated-emission-depletion fluorescence microscopy. *Optics Letters*, 19(11):780–782, 1994.

- [49] Thomas A. Klar and Stefan W. Hell. Subdiffraction resolution in far-field fluorescence microscopy. *Optics Letters*, 24(14):954–956, 1999.
- [50] Roman Schmidt, Christian A. Wurm, Stefan Jakobs, Johann Engelhardt, Alexander Egner, and Stefan W. Hell. Spherical nanosized focal spot unravels the interior of cells. *Nature Methods*, 5(6):539–544, 2008.
- [51] Gerald Donnert, Jan Keller, Christian A. Wurm, Silvio O. Rizzoli, Volker Westphal, Andreas Schönle, Reinhard Jahn, Stefan Jakobs, Christian Eggeling, and Stefan W. Hell. Two-color far-field fluorescence nanoscopy. *Biophysical Journal*, 92(8):L67–L69, 2007.
- [52] Lars Meyer, Dominik Wildanger, Rebecca Medda, Annedore Punge, Silvio O. Rizzoli, Gerald Donnert, and Stefan W. Hell. Dual-color STED microscopy at 30-nm focal-plane resolution. *Small*, 4(8):1095–1100, 2008.
- [53] Benjamin Harke, Chaitanya K. Ullal, Jan Keller, and Stefan W. Hell. Three-dimensional nanoscopy of colloidal crystals. *Nano Letters*, 8(5):1309–1313, 2008.
- [54] U. Valentin Nägerl, Katrin I. Willig, Birka Hein, Stefan W. Hell, and Tobias Bonhoeffer. Live-cell imaging of dendritic spines by STED microscopy. *Proceedings of the National Academy of Sciences*, 105(48):18982–18987, 2008.
- [55] Birka Hein, Katrin I. Willig, and Stefan W. Hell. Stimulated emission depletion (STED) nanoscopy of a fluorescent protein-labeled organelle inside a living cell. *Proceedings of the National Academy of Sciences*, 105(38):14271–14276, 2008.
- [56] Volker Westphal, Silvio O. Rizzoli, Marcel A. Lauterbach, Dirk Kamin, Reinhard Jahn, and Stefan W. Hell. Video-rate far-field optical nanoscopy dissects synaptic vesicle movement. *Science*, 320(5873):246–249, 2008.
- [57] Volker Westphal, Marcel A. Lauterbach, Angelo Di Nicola, and Stefan W. Hell. Dynamic far-field fluorescence nanoscopy. *New Journal of Physics*, 9(12):435–445, 2007.
- [58] Massimiliano Stagi, Zoe A. Klein, Travis J. Gould, Joerg Bewersdorf, and Stephen M. Strittmatter. Lysosome size, motility and stress response regulated by fronto-temporal dementia modifier TMEM106b. *Molecular and Cellular Neuroscience*, 61:226–240, 2014.
- [59] Roman Schmidt, Christian A. Wurm, Annedore Punge, Alexander Egner, Stefan Jakobs, and Stefan W. Hell. Mitochondrial cristae revealed with focused light. *Nano Letters*, 9(6):2508–2510, 2009.
- [60] Christian Eggeling, Christian Ringemann, Rebecca Medda, Günter Schwarzmann, Konrad Sandhoff, Svetlana Polyakova, Vladimir N. Belov, Birka Hein, Claas von Middendorff,

- Andreas Schönle, and Stefan W. Hell. Direct observation of the nanoscale dynamics of membrane lipids in a living cell. *Nature*, 457(7233):1159–1162, 2009.
- [61] Robert J. Kittel, Carolin Wichmann, Tobias M. Rasse, Wernher Fouquet, Manuela Schmidt, Andreas Schmid, Dhananjay A. Wagh, Christian Pawlu, Robert R. Kellner, Katrin I. Willig, *et al.* Bruchpilot promotes active zone assembly, Ca²⁺ channel clustering, and vesicle release. *Science*, 312(5776):1051–1054, 2006.
- [62] Gerald Donnert, Jan Keller, Rebecca Medda, M. Alexandra Andrei, Silvio O. Rizoli, Reinhard Lüthmann, Reinhard Jahn, Christian Eggeling, and Stefan W. Hell. Macromolecular-scale resolution in biological fluorescence microscopy. *Proceedings of the National Academy of Sciences*, 103(31):11440–11445, 2006.
- [63] Jochen J. Sieber, Katrin I. Willig, Carsten Kutzner, Claas Gerding-Reimers, Benjamin Harke, Gerald Donnert, Burkhard Rammner, Christian Eggeling, Stefan W. Hell, Helmut Grubmüller, *et al.* Anatomy and dynamics of a supramolecular membrane protein cluster. *Science*, 317(5841):1072–1076, 2007.
- [64] Albert Einstein. Zur quantentheorie der strahlung. *Physikalische Zeitschrift*, 18:121–128, 1917.
- [65] Robert C. Hilborn. Einstein coefficients, cross sections, f values, dipole moments, and all that. *American Journal of Physics*, 50(11):982–986, 1982.
- [66] Stefan W. Hell. Toward fluorescence nanoscopy. *Nature Biotechnology*, 21(11):1347–1355, 2003.
- [67] Volker Westphal and Stefan W. Hell. Nanoscale resolution in the focal plane of an optical microscope. *Physical Review Letters*, 94(14):143903, 2005.
- [68] Yuansheng Sun, Giorgio Tortarolo, Kai-Wen Teng, Yuji Ishitsuka, Ulas C. Coskun, Shih-Chu Jeff Liao, Alberto Diaspro, Giuseppe Vicidomini, Paul R. Selvin, and Beniamino Barbieri. A novel pulsed STED microscopy method using fastfilm and the phasor plots. In *Proceedings of SPIE*, volume 10069, pages 100691C–1, 2017.
- [69] Giuseppe Vicidomini, Gael Moneron, Kyu Young Han, Volker Westphal, Haisen Ta, Matthias Reuss, Johann Engelhardt, Christian Eggeling, and Stefan W. Hell. Sharper low-power STED nanoscopy by time gating. *Nature Methods*, 8(7):571–573, 2011.
- [70] Giuseppe Vicidomini, Andreas Schönle, Haisen Ta, Kyu Young Han, Gael Moneron, Christian Eggeling, and Stefan W. Hell. STED nanoscopy with time-gated detection: theoretical and experimental aspects. *PloS one*, 8(1):e54421, 2013.

- [71] Dominik Wildanger, Brian R. Patton, Heiko Schill, Luca Marseglia, J. P. Hadden, Sebastian Knauer, Andreas Schönle, John G. Rarity, Jeremy L. O'Brien, Stefan W. Hell, *et al.* Solid immersion facilitates fluorescence microscopy with nanometer resolution and sub-Ångström emitter localization. *Advanced Materials*, 24(44), 2012.
- [72] Jong-Bong Lee, Richard K. Hite, Samir M. Hamdan, X. Sunney Xie, Charles C. Richardson, and Antoine M. Van Oijen. DNA primase acts as a molecular brake in DNA replication. *Nature*, 439(7076):621–624, 2006.
- [73] Gijs J. L. Wuite, Steven B. Smith, Mark Young, David Keller, and Carlos Bustamante. Single-molecule studies of the effect of template tension on T7 DNA polymerase activity. *Nature*, 404(6773):103–106, 2000.
- [74] Lee Zou and Stephen J. Elledge. Sensing DNA damage through ATRIP recognition of RPA-ssDNA complexes. *Science*, 300(5625):1542–1548, 2003.
- [75] Jörg C. Schlatterer, Lisa W. Kwok, Jessica S. Lamb, Hye Yoon Park, Kurt Andresen, Michael Brenowitz, and Lois Pollack. Hinge stiffness is a barrier to RNA folding. *Journal of Molecular Biology*, 379(4):859–870, 2008.
- [76] Sören Doose, Hannes Barsch, and Markus Sauer. Polymer properties of polythymine as revealed by translational diffusion. *Biophysical journal*, 93(4):1224–1234, 2007.
- [77] M. C. Murphy, Ivan Rasnik, Wei Cheng, Timothy M. Lohman, and Taekjip Ha. Probing single-stranded DNA conformational flexibility using fluorescence spectroscopy. *Biophysical Journal*, 86(4):2530–2537, 2004.
- [78] Ted A. Laurence, Xiangxu Kong, Marcus Jäger, and Shimon Weiss. Probing structural heterogeneities and fluctuations of nucleic acids and denatured proteins. *Proceedings of the National Academy of Sciences*, 102(48):17348–17353, 2005.
- [79] M. -N. Dessinges, Berenike Maier, Y. Zhang, M. Peliti, David Bensimon, and Vincent Croquette. Stretching single stranded DNA, a model polyelectrolyte. *Physical Review Letters*, 89(24):248102, 2002.
- [80] D. B. McIntosh and O. A. Saleh. Salt species-dependent electrostatic effects on ssDNA elasticity. *Macromolecules*, 44(7):2328–2333, 2011.
- [81] Wuen-shiu Chen, Wei-Hung Chen, Zephan Chen, Ashton A. Gooding, Kuan-Jiuh Lin, and Ching-Hwa Kiang. Direct observation of multiple pathways of single-stranded DNA stretching. *Physical Review Letters*, 105(21):218104, 2010.
- [82] Berenike Maier, David Bensimon, and Vincent Croquette. Replication by a single DNA polymerase of a stretched single-stranded DNA. *Proceedings of the National Academy of Sciences*, 97(22):12002–12007, 2000.

- [83] Ashok A. Deniz, Ted A. Laurence, Maxime Dahan, Daniel S. Chemla, Peter G. Schultz, and Shimon Weiss. Ratiometric single-molecule studies of freely diffusing biomolecules. *Annual Review of Physical Chemistry*, 52(1):233–253, 2001.
- [84] Huimin Chen, Steve P. Meisburger, Suzette A. Pabit, Julie L. Sutton, Watt W. Webb, and Lois Pollack. Ionic strength-dependent persistence lengths of single-stranded RNA and DNA. *Proceedings of the National Academy of Sciences*, 109(3):799–804, 2012.
- [85] Nicole C. Robb, Thorben Cordes, Ling Chin Hwang, Kristofer Gryte, Diego Duchi, Timothy D. Craggs, Yusdi Santoso, Shimon Weiss, Richard H. Ebright, and Achillefs N. Kapanidis. The transcription bubble of the RNA polymerase–promoter open complex exhibits conformational heterogeneity and millisecond-scale dynamics: implications for transcription start-site selection. *Journal of Molecular Biology*, 425(5):875–885, 2013.
- [86] Xiangyun Qiu, Kurt Andresen, Lisa W. Kwok, Jessica S. Lamb, Hye Yoon Park, and Lois Pollack. Inter-DNA attraction mediated by divalent counterions. *Physical Review Letters*, 99(3):038104, 2007.
- [87] Gerard C. L. Wong and Lois Pollack. Electrostatics of strongly charged biological polymers: ion-mediated interactions and self-organization in nucleic acids and proteins. *Annual Review of Physical Chemistry*, 61:171–189, 2010.
- [88] Tomasz Heyduk and Ewa Heyduk. Molecular beacons for detecting DNA binding proteins. *Nature Biotechnology*, 20(2):171–176, 2002.
- [89] Alexander Hillisch, Mike Lorenz, and Stephan Diekmann. Recent advances in FRET: distance determination in protein–DNA complexes. *Current Opinion in Structural Biology*, 11(2):201–207, 2001.
- [90] Paul R. Selvin. The renaissance of fluorescence resonance energy transfer. *Nature Structural Biology*, 7(9):730–734, 2000.
- [91] Taekjip Ha. Single-molecule fluorescence methods for the study of nucleic acids. *Current Opinion in Structural Biology*, 11(3):287–292, 2001.
- [92] Paul R. Selvin. Fluorescence resonance energy transfer. *Methods in Enzymology*, 246:300–334, 1995.
- [93] Tomas Hirschfeld. Optical microscopic observation of single small molecules. *Applied Optics*, 15(12):2965–2966, 1976.
- [94] William E. Moerner and Lothar Kador. Optical detection and spectroscopy of single molecules in a solid. *Physical Review Letters*, 62(21):2535–2538, 1989.

- [95] Michel Orrit and J. Bernard. Single pentacene molecules detected by fluorescence excitation in a *p*-terphenyl crystal. *Physical Review Letters*, 65(21):2716–2719, 1990.
- [96] J. K. Trautman, J. J. Macklin, L. E. Brus, and E. Betzig. Near-field spectroscopy of single molecules at room temperature. *Nature*, 369(6475):40–42, 1994.
- [97] Achillefs N. Kapanidis, Nam Ki Lee, Ted A. Laurence, Sören Doose, Emmanuel Margeat, and Shimon Weiss. Fluorescence-aided molecule sorting: analysis of structure and interactions by alternating-laser excitation of single molecules. *Proceedings of the National Academy of Sciences*, 101(24):8936–8941, 2004.
- [98] Nam Ki Lee, Achillefs N. Kapanidis, You Wang, Xavier Michalet, Jayanta Mukhopadhyay, Richard H. Ebricht, and Shimon Weiss. Accurate FRET measurements within single diffusing biomolecules using alternating-laser excitation. *Biophysical Journal*, 88(4):2939–2953, 2005.
- [99] Stephen M. Stigler. Poisson on the Poisson distribution. *Statistics & Probability Letters*, 1(1):33–35, 1982.
- [100] Konan Peck, Lubert Stryer, Alexander N. Glazer, and Richard A. Mathies. Single-molecule fluorescence detection: autocorrelation criterion and experimental realization with phycoerythrin. *Proceedings of the National Academy of Sciences*, 86(11):4087–4091, 1989.
- [101] Carlos Bustamante, Steven B. Smith, Jan Liphardt, and Doug Smith. Single-molecule studies of DNA mechanics. *Current Opinion in Structural Biology*, 10(3):279–285, 2000.
- [102] Demetrios T. Braddock, John M. Louis, James L. Baber, David Levens, and G. Marius Clore. Structure and dynamics of KH domains from FBP bound to single-stranded DNA. *Nature*, 415(6875):1051–1056, 2002.
- [103] Wilma King Olson. Configurational statistics of polynucleotide chains. a single virtual bond treatment. *Macromolecules*, 8(3):272–275, 1975.
- [104] Richard A. Keller, W. Patrick Ambrose, Peter M. Goodwin, James H. Jett, John C. Martin, and Ming Wu. Single-molecule fluorescence analysis in solution. *Applied Spectroscopy*, 50(7):12A–32A, 1996.
- [105] William E. Moerner. A dozen years of single-molecule spectroscopy in physics, chemistry, and biophysics. *The Journal of Physical Chemistry B*, 106(5):910–927, 2002.
- [106] Benjamin Schuler, Everett A. Lipman, and William A. Eaton. Probing the free-energy surface for protein folding with single-molecule fluorescence spectroscopy. *Nature*, 419(6908):743–747, 2002.

- [107] Sua Myong, Ivan Rasnik, Chirlmin Joo, Timothy M. Lohman, and Taekjip Ha. Repetitive shuttling of a motor protein on DNA. *Nature*, 437(7063):1321–1325, 2005.
- [108] S. Rüttinger, V. Buschmann, B. Krämer, R. Erdmann, R. Macdonald, and F. Koberling. Comparison and accuracy of methods to determine the confocal volume for quantitative fluorescence correlation spectroscopy. *Journal of Microscopy*, 232(2):343–352, 2008.
- [109] Philip Tinnefeld. Single-molecule detection: Breaking the concentration barrier. *Nature Nanotechnology*, 8(7):480–482, 2013.
- [110] E. J. Ambrose. A surface contact microscope for the study of cell movements. *Nature*, 178(4543):1194–1194, 1956.
- [111] Michael J. Levene, Jonas Korlach, Stephen W. Turner, Mathieu Foquet, Harold G. Craighead, and Watt W. Webb. Zero-mode waveguides for single-molecule analysis at high concentrations. *Science*, 299(5607):682–686, 2003.
- [112] Sabrina R. Leslie, Alexander P. Fields, and Adam E. Cohen. Convex lens-induced confinement for imaging single molecules. *Analytical Chemistry*, 82(14):6224–6229, 2010.
- [113] C. Eggeling, M. Hilbert, H. Bock, C. Ringemann, M. Hofmann, A. C. Stiel, M. Andresen, S. Jakobs, A. Egner, A. Schönle, *et al.* Reversible photoswitching enables single-molecule fluorescence fluctuation spectroscopy at high molecular concentration. *Microscopy Research and Technique*, 70(12):1003–1009, 2007.
- [114] Nam Ki Lee, Achillefs N. Kapanidis, Hye Ran Koh, You Korlann, Sam On Ho, Younggyu Kim, Natalie Gassman, Seong Keun Kim, and Shimon Weiss. Three-color alternating-laser excitation of single molecules: monitoring multiple interactions and distances. *Biophysical Journal*, 92(1):303–312, 2007.
- [115] Jinwoo Lee, Sanghwa Lee, Kaushik Ragunathan, Chirlmin Joo, Taekjip Ha, and Sungchul Hohng. Single-molecule four-color FRET. *Angewandte Chemie International Edition*, 49(51):9922–9925, 2010.
- [116] Andrea M. Mastro, Michael A. Babich, William D. Taylor, and Alec D. Keith. Diffusion of a small molecule in the cytoplasm of mammalian cells. *Proceedings of the National Academy of Sciences*, 81(11):3414–3418, 1984.
- [117] Katherine Luby-Phelps. Cytoarchitecture and physical properties of cytoplasm: volume, viscosity, diffusion, intracellular surface area. *International Review of Cytology*, 192:189–221, 1999.
- [118] Nam Ki Lee, Hye Ran Koh, Kyu Young Han, and Seong Keun Kim. Folding of 8-17 deoxyribozyme studied by three-color alternating-laser excitation of single molecules. *Journal of the American Chemical Society*, 129(50):15526–15534, 2007.

Part II

Time-resolved Spectroscopy about Degradation Process of Organic Light Emitting Diode

Chapter 1

Introduction to Organic Light Emitting Diode (OLED)

1.1 History and Working Principle of OLED

History of OLED

Part II covers OLEDs that generate electroluminescence compared to Part I, which deals with photoluminescence. Electroluminescence refers to the generation of light by electrical excitation of organic materials. The first experiments dealt with electroluminescence on anthracene crystals were successfully carried out by Pope et al. (1963), as well by Helfrich and Schneider (1965) [1–3]. The organic molecules are electrically conductive as a result of delocalization of π electrons caused by conjugation over part or all of the molecules. In 1982, the first thin film electroluminescence device was developed by vacuum deposition method, and a year later, similar devices made of polymer materials were developed [4, 5]. The efficiency and lifetime of the devices were extremely low, requiring more than 100 V for operation.

The electroluminescence of organic materials initially did not get much attention. The first heterojunction device by Tang and Van Slyke in 1987 [6] sparked academic and commercial interest. The achievement of a double-organic-layered architecture consisting of a hole transporting layer and an emissive layer of aluminum quinolinolate (Alq_3) gave electroluminescence around $1,000 \text{ cd}\cdot\text{m}^{-2}$ at driving voltages below 10 V. Double-organic-layered OLED is still the archetypical structure for OLEDs [7, 8]. After then, a huge increase in device lifetime and efficiency has been achieved [9, 10], which allows organic electroluminescence to enter the display and lighting market [3, 11].

For high efficiency and stability, host-guest system has been used in emissive layer (EML). In 1998, Baldo significantly improved the internal quantum efficiencies of the devices by applying the triplet harvesting effect [12]. As the recombination of electrons and holes yields triplet (75%) and singlet (25%) excitons and organic materials usually emit only from singlet states (fluorescence), this limited the achievable internal quantum efficiency. Baldo could overcome this limitation by using phosphorescent transition metal complexes having heavy atoms (such as iridium or platinum) as the emitting materials. Light is emitted from the triplet states of these compounds and singlet excitons are rapidly converted into triplets through efficient intersystem crossing (ISC). Highly efficient green and red electrophosphorescent emitters have been demonstrated with internal quantum efficiencies approaching 100% [13, 14].

The development history of OLED device structure is shown in Figure 1.1. The OLED architectures became complicated from a simple mono-layer structure to a multi-layer structure in order to improve device efficiency [15]. Each layer has a special function such as the hole injecting layer (HIL), hole transporting layer (HTL), hole blocking layer (HBL), emissive layer (EML), and electron transporting layer (ETL). In electroluminescent devices the recombi-

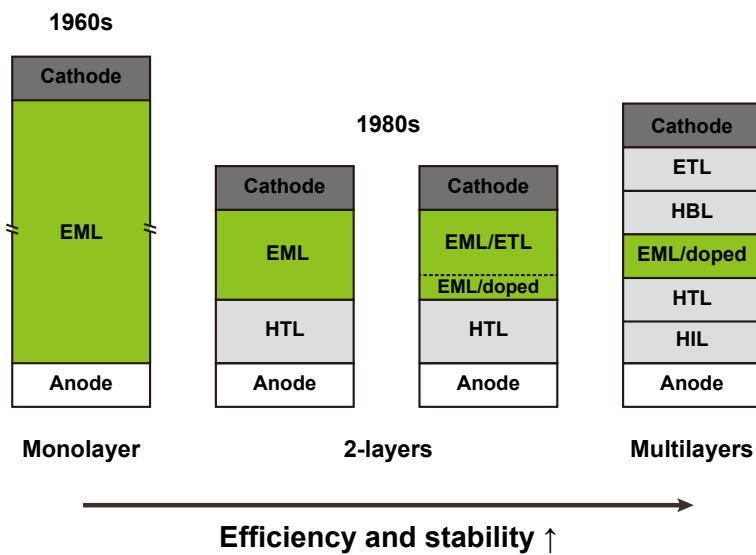


Figure 1.1 Evolution of OLED device structures. (HIL = hole injecting layer, HTL = hole transporting layer, EML = emissive layer, HBL = hole blocking layer, ETL = electron transporting layer)

nation zone should be in the middle of EML. However, balanced charge injection or carrier mobility is usually not observed in single layer OLEDs and is achieved by the incorporation of additional layers giving multilayer OLEDs. (In organic semiconductors, holes are generally more mobile than electrons.) Hole and electron transport layers provide facilitated charge injection and enhanced recombination of electrons and holes in the EML. Charge and exciton blocking layers block the opposite charge carriers from passing over the EML. It has been found that the electroluminescence efficiency of OLEDs can be increased by the confinement of charge carriers or excitons in a multilayer device [16]. The confinement of charge carriers can increase the capture of carriers, and the confinement of excitons can improve the energy transfer from the host to the guest [15].

Working Principle

OLEDs typically consist of a metal cathode (e.g., Ca, Al), an organic layers, and a transparent anode (e.g., indium tin oxide (ITO)) deposited on a transparent substrate such as glass or flexible polymer [17]. Figure 1.2 summarizes the working principle of three-layered OLED.

Under a driving voltage, electrons are injected from the cathode into the lowest unoccupied molecular orbital (LUMO) of the adjacent organic layer (ETL) and withdrawn from the highest occupied molecular orbital (HOMO) of the adjacent organic layer (HTL) to anode. The latter process is described as the holes are injected into the HOMO of HTL from the anode. At this time, HIL can be inserted between anode and HTL to facilitate hole injection. The electrons and holes move through the organic layers and recombine to form an “exciton”, a bound state of the electron and hole. The exciton, or excited molecule, is usually generated in the guest (doped) material of EML. As the exciton decay

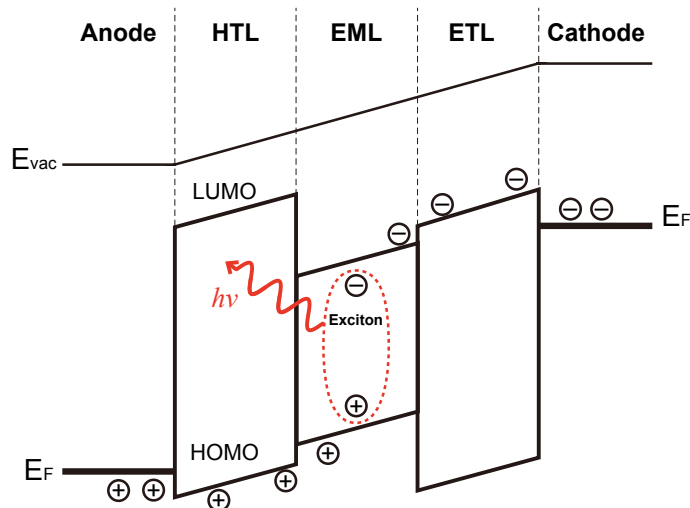


Figure 1.2 Energy level scheme of a typical heterojunction OLED with an applied bias voltage. HOMO and LUMO levels of organic layers, vacuum levels (E_{vac}), and the Fermi levels of electrodes (E_F) are represented.

to ground state, it emits the electroluminescence [18,19]. The frequency of this radiation depends on the bandgap of the material, in this case the difference in energy between the HOMO and LUMO.

The enormous interest in OLEDs is especially caused by technological aspects such as low costs, the ease of fabrication using standard techniques (e.g. vacuum deposition or solution processing) [8, 20], the possibility of realizing flexible or large-area displays [21], their use in lighting applications and the variety of organic materials providing emission wavelengths that cover wavelengths from the ultraviolet to near infrared [22].

1.2 Degradation Problem

OLEDs have been mass-produced for display applications and are expected to find application in the commercial lighting market in the near future. Besides

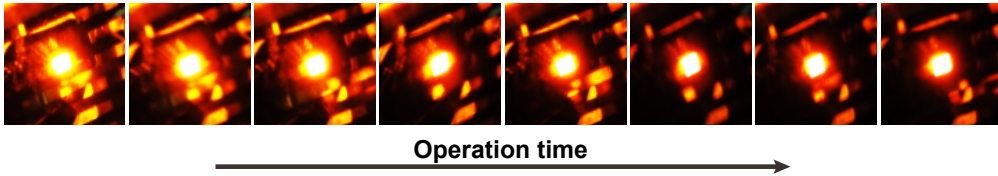


Figure 1.3 Reduced OLED brightness with operation time.

high efficiencies and low power consumptions, it is also important that the devices have a high operational stability [23]. Typically, the higher is the luminance of a device and the higher is the energy of the emission, the shorter is the lifetime of an OLED [3]. For applications requiring very high brightness like outdoor displays, high dynamic range displays, or window integrated transparent devices, the current OLED technology still does not provide the required lifetimes.

Over the past three decades, OLED research has been conducted to identify and overcome the failure and degradation processes that lead to limited device lifetimes. Already in 1982, there were discussions on the device lifetime for the first vacuum deposited device [4]. In 2004, Aziz and Popovic provided an extended overview about the known degradation mechanisms [24]. According to Sebastian Scholz *et al.* [3], the phenomenon of degradation can be categorized as (i) the growth of non-emissive areas, mainly known as “dark-spot degradation”, (ii) the immediate breakdown of the electroluminescent behavior (catastrophic failure), (iii) the short- or long-term degradation effect (“intrinsic degradation”), well described by the (stretched) exponential decay function of the decreasing luminance [24–26], and (iv) additionally, the voltage increase during the aging process (direct current (DC) driven) [25, 27].

Although many different degradation mechanisms have similar effects and appearances, they can be classified on the basis of external and internal causes of

degradation. (intrinsic factors: electro- or photochemical reactions, thermal behavior, or interfacial effects such as cathode delamination; extrinsic factors: water, oxygen, impurities, fabrication environment like dust and vacuum pressure, and the substrate conditions) (i) Dark spot degradation and (ii) catastrophic failure that are caused by extrinsic factors can be suppressed by carefully optimized and controlled fabrication conditions and an appropriate encapsulation of the devices and thus are no longer considered an obstacle for commercial applications [23]. Intrinsic degradation resulting in (iii) and (iv) is characterized by the decrease of overall luminance over time during continuous operation. In contrast to extrinsic degradation mechanisms, intrinsic degradation mechanisms are significantly more difficult to investigate.

Intrinsic degradation mechanisms have been studied by different chemical and electrochemical analysis techniques such as voltammetry techniques, electric field profiling, photoluminescence, as well as high performance liquid chromatography (HPLC) [28, 29]. Several researchers have discovered a wide range of photochemical and electrochemical reactions that can be detected in aged OLEDs [29–35]. It is assumed that the dipole reorientation, the charge carriers, and the excitons were changed by various chemical, electrochemical, and photochemical reactions during driving the device. These phenomena lead to a positional shifts of the recombination zone, an accumulation processes on interfaces, and an increase of internal resistance, resulting in OLED degradation.

Nevertheless, predictions of device stability based on material properties and overall device architecture are still out of reach. To enable the development of high performance and stability device, it is important to understand the degradation mechanism. An understanding of the degradation mechanisms and the chemical nature of defects in the organic layers will lead to further design rules for improved molecular stability for OLED applications, as well as other

organic based optoelectronic devices.

Chapter 2

Study for Luminescence Properties of the Charge Traps in OLED using Transient Electroluminescence

2.1 Introduction

The limited operational stability of organic light emitting devices (OLEDs) presents a challenge to their widespread acceptance [3,23,24]. In order to utilize OLED in various fields such as large-area displays and solid-state lighting, the development of devices with high luminescence is required. It is necessary to analyze the cause of device degradation for improving OLED device lifetime.

Luminescence intensity decrease and driving voltage increase in electrically aged device [36]. The charge carriers are confined in defect sites that have lower energy level than surrounding molecules. Giebink and coworkers introduced a model where defect sites act as luminescence quenchers, non-radiative recombination centers, and deep charge traps [37]. According to this model, when the defects act as luminescence quenchers, luminescence lifetime is reduced. Emitter

decays faster with quenchers than without them [38,39]. On the other hand, if the defects act as a non-radiative recombination centers or a charge traps independent of the light emitting process, it is difficult to observe through the luminescence. Several electrical measurements such as electrochemical impedance spectroscopy (EIS), linear sweep voltammetry (LSV), and charge-based deep level transient spectroscopy (Q-DLTS) have been used to observe charge traps in OLED devices. However, these methods have limitations such as highly dependence of fitting models or experimentally challenging process [40–44].

We have introduced transient electroluminescence (TREL) technique to analyze what happens in devices. TREL that measure the time-resolved luminescence when a pulse-shaped voltage is applied to device enables noninvasive measurements, as well as *in situ* analysis on the same environment in which OLED operates [45]. TREL technique is often used to study the properties of devices, particularly in measuring the mobility of charge carriers in devices [46–49]. The mobility was calculated by measuring the time between the first application of operating voltage to the OLED device and the light emission.

In this study, we have analyzed whole TREL curves by dividing it into onset, rise, and decay times. By analyzing the mobility of the charge carrier and the emission decay, we figure out the existence of the charge trap and the influence of the charge trap on the luminescence. TREL technique is a method of observing luminescence unlike conventional electric techniques, and it is possible to analyze the change of luminescence according to electrical properties. We develop a new analysis method of TREL result, which can be applied to identify the internal state of other optoelectronic device. We have also observed luminescence of the charge trap and its characteristics.

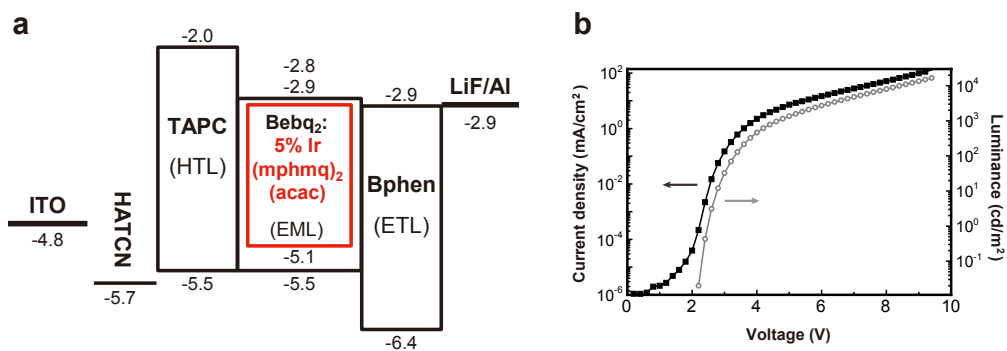


Figure 2.1 Fabricated red phosphorescent OLED device and its luminescence properties. (a) Schematic energy band diagram of red phosphorescent OLED device. The energy levels of LUMO and HOMO are written in units of eV. (b) J-V-L characteristics of fabricated red phosphorescent OLED.

2.2 Materials and Methods

2.2.1 OLED Fabrication

The exact device configuration used in this work was indium tin oxide (ITO, 150 nm)/hexaazatriphenylene hexacarboxylic diimide (HATCN, 7 nm)/4,4'-cyclohexyldienebis(N,N-bis(4-methylphenyl)benzenamine) (TAPC, 60 nm)/Bis(10-hydroxybenzo[h]quinolinato)beryllium (Bebq₂):red dopants Iridium(III)bis(4-methyl-2-(3,5-dimethylphenyl)quinolinato-N,C2')acetylacetonate (Ir(mphmq)₂(acac)) (20 nm)/Bathophenanthroline (Bphen, 60 nm) or tris-(8-hydroxyquinoline) aluminum (Alq₃, 60 nm)/Lithium fluoride (LiF, 2.5 nm)/Aluminum (Al, 100 nm). To fabricate OLED devices, clean glass substrates precoated with a 150 nm thick indium tin oxide (ITO) layer with a sheet resistance of 10 Ω/sq were used (Figure 2.1a). Line patterns of ITO were formed on glass by photolithography process. HATCN, TAPC, Bebq₂, Bphen were purchased from Jilin OLED Materials Tech. LiF and Al were purchased from Taewon Scientific. Ir (mphmq)₂(acac)

was synthesized according to the synthesis method of previous report [50]. The ITO glass was cleaned by sonification in an isopropylalcohol and acetone, rinsed in deionized water, and finally irradiation in a UV-ozone chamber. All organic materials were deposited by the vacuum evaporation technique under a pressure of $3 \cdot 10^{-7}$ Torr. LiF and organic materials were thermally deposited on the ITO substrate at a rate of 0.3 \AA/s and Al at a rate of 5 \AA/s . The fabricated OLED devices were encapsulated with a sealing glass and a UV curable resin in a nitrogen atmosphere to prevent contact with moisture and oxygen in the air. The J-V-L data of the OLEDs were measured using a sourcemeter (2635A, Keithley) and a spectroradiometer (CS-100A & CS-2000A, Konica Minolta) (Figure 2.1b). The fabricated devices were electrically degraded by applying 5 V DC voltage.

2.2.2 Transient Electro- and Photo-luminescence Measurements

The transient electroluminescence (TREL) measurement begins with applying a rectangular voltage pulse using DG645 (delay generator, Stanford Research System, rise time $< 100 \text{ ps}$, fall time $< 3 \text{ ns}$) (Figure 2.2). Voltage pulses are applied with a voltage of 4 V for $100 \text{ }\mu\text{s}$, with an off-time of 1 ms or 4 ms between each pulse. The OLED-emitted light was collected by lens ($f = 100 \text{ mm}$) and detected by APD (PFCCTC-FCAPC, MPD) and analyzed on a SPC-150 (Becker & Hickl GmbH) board (maximum time resolution of 25 ns). Only the light with a wavelength 580–620 nm was used for the analysis to measure the phosphorescence of the dopant material.

Transient photoluminescence (TRPL) is a method of forming an exciton using a light source rather than a voltage. Ir(mphmq)₂(acac), a dopant material, was excited with a 200 nW 405 nm laser (LDH-P-C-405 with PDL 800-B driver, Picoquant) through the lens ($f = 40 \text{ mm}$) as shown in Figure 2.2 blue line. 405

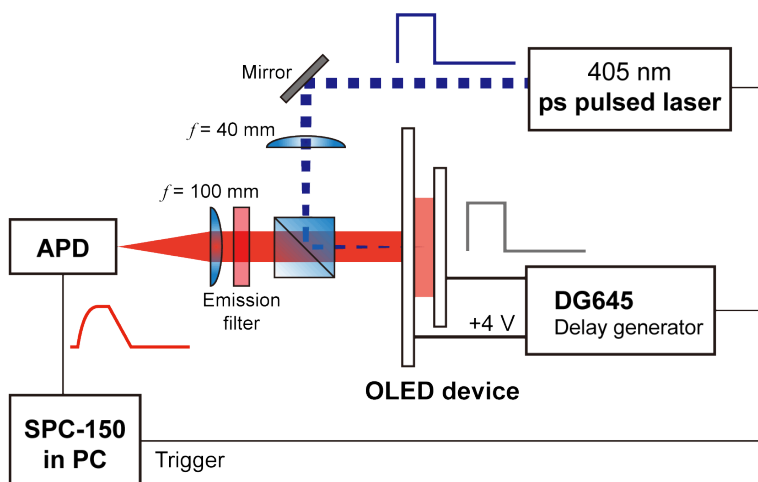


Figure 2.2 Experimental setup of transient electroluminescence (TREL) and photoluminescence (TRPL). Delay generator (for TREL) and pulsed laser (for TRPL) that were triggered by SPC-150 apply the pulsed excitation to the OLED. The generating light was detected by APD and analyzed by SPC-150 according to time.

nm can not excite other materials except $\text{Ir}(\text{mphpmq})_2(\text{acac})$ due to excitation energy mismatch. The shape of the laser pulse was the same as that of the voltage pulse in TREL experiment. Except for excitation source, the other setup was the same for TREL and TRPL.

2.2.3 Measuring Electronic Properties of OLED

We have compared the electrical properties before and after degradation of the device. Electrochemical impedance spectroscopy (EIS300, Gamry Instrument) was used to measure the capacitance of the OLED device depending on frequency of potential perturbation. DC voltage of 4 V was applied and the AC voltage of 10 mV was scanned at a frequency of 10^{-1} – 10^6 Hz, and the capacitance of the device was plotted as a Nyquist plot which is the relationship between real part and imaginary part of capacitance. EIS measurements con-

firmed the internal and interface resistance of the device. Detailed analyses are discussed with data in Section 2.3.2.

Linear sweep voltammetry (LSV) can observe the presence of the charge traps as reported by Kodacov *et al.* [42, 43]. Voltammetry measurements were performed with a electrochemical workstation (CHI6048, CHI Instruments) The voltage was scanned from -1 V to 4.5 V (forward scan) at sufficiently high scan rate (40 V/s). This is an electrical analysis method that can confirm the existence of the charge trap. Briefly, there is a trap when the bump appears in current-voltage curve when scanning the voltage. Further explanation is given in Section 2.3.2.

2.3 Results and Discussion

2.3.1 Analysis of TREL Curves

We used a red phosphorescent OLED device (ITO/HATCN/TAPC/Bebq₂:5% Ir(mpmhmq)₂(acac)/Bphen/LiF/Al) as a model system (Figure 2.1a). The device consists anode, hole injection layer, hole transport layer, emissive layer with Ir(mpmhmq)₂(acac) dopant, electron transport layer and cathode. For electrical aging, the devices were driven at constant voltage (5 V).

TERL is one of the most suitable method for analyzing properties of light emitting optoelectronic device. The graph in Figure 2.3 showing the brightness versus the time is called a TREL curve. Rectangular pulse voltage is applied at $t = 0$. The gray and red line refer to the applied voltage and EL intensity, respectively. When the voltage greater than built-in voltage is applied on device, the charge carriers are injected from corresponding electrodes (**I**). The electrons originating from the cathode pass through the electron transport layer and the holes originating from the anode pass through the hole transport layer. The

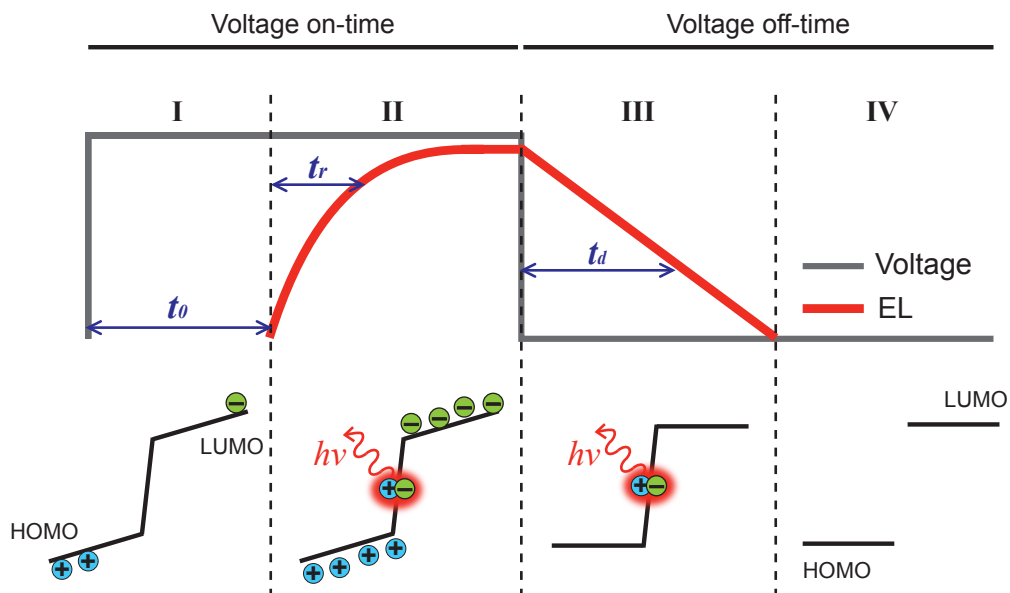


Figure 2.3 Schematic diagram of TREL experiments shows the time until the first light comes out (t_0), the time until light is saturated (t_r), and decay time (t_d) after voltage is turned off. The voltage of the rectangular pulse applied to the device over time and the amount of light generated by the device are represented by gray and red lines, respectively. Electrons and holes are injected from corresponding electrodes right after the voltage is applied (I). Two kinds of charge carriers with energy which comes from external voltage move along the organic layers and form an exciton that can make luminescence (II). When the voltage is turned off, the remaining excitons decay with their lifetime (III) and then the device has a rest before the next voltage pulse arrives (IV).

electrons and holes meet in the emissive layer to form excitons and they start to emit luminescence (II). We observe the luminescence emitted by the excitons. After the voltage is turned off, the remaining excitons decay with luminescence and the resulting decay curve is observed (III). After the off-time which is sufficient for the exciton to completely decay (IV), the pulsed voltage is applied again.

In order to analyze the TREL curves, there are three components that we should concentrate on: t_0 (onset time), t_r (rise time), and t_d (decay time). t_0 is the time between the first application of operating voltage to the OLED device and the light emission. The time at which the first two injected charge carriers meet is affected by the injection rate and the mobility of the relatively slow charge carriers (electrons in most cases). t_r is the time from t_0 until the EL intensity is saturated. t_r is also affected by the mobility of charge carriers. The rise curve is fitted with logarithmic function to obtain t_0 and t_r . We define t_0 as the time of the point that the baseline and the fitted curve intersects. t_r is the time until luminescence reaches 80% of the maximum value starting from the time t_0 . Finally, t_d means the emission lifetime of the excitons after the voltage is turned off. t_d is determined by single- or bi-exponential decay fitting of the TREL decay curve depending on the shape of the curve.

2.3.2 The Charge Traps in Degraded Device

TREL Experiments

Figure 2.4a shows how the TREL curve changes as the device is degraded. The degradation ratio means the degree of decrease in EL intensity compared to pristine device at the same voltage. The TREL curve of pristine device is black colored and that of the most degraded device (degradation ratio 66%) is red

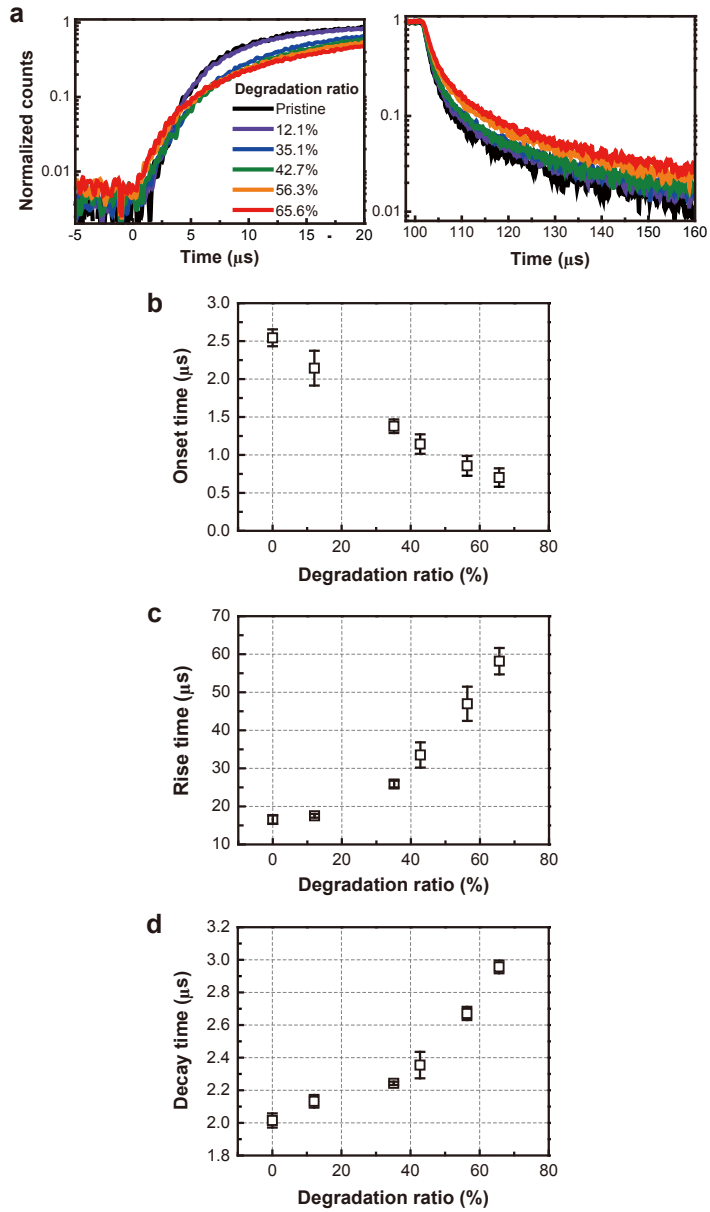


Figure 2.4 TREL results of OLED devices during degradation process. (a) TREL curves show the increase and decrease of EL according to time. The curves are smoothed 5 points by fast Fourier transform (FFT) method. (b-d) While the device is 66% degraded, t_0 , t_r , and t_d are plotted according to degradation ratio. t_0 is about 2 μs faster, t_r is about 55 μs slower, and t_d is about 1 μs longer. The error bars show the standard deviations of the four repeated experimental results.

colored. As the device is degraded, luminescence starts earlier and ends later. The changes of three time components (t_0 , t_r , and t_d) during degradation are plotted on Figures 2.4b-d. We investigated the implications of changes in the components as the device was degraded gradually.

t_0 and t_r : It is expected that t_0 and t_r will increase because the resistance inside the device will increase, then the mobility of the charge carriers will decrease in a degraded device. Surprisingly, t_0 decreases by 2 μs during the experiments as shown in Figure 2.4b. It means that the luminescence starts earlier in the degraded device even though the charge carriers in degraded device is slower than those in pristine device. If two charge carriers start to move from the inside the organic layer, rather than from the electrode, they can form excitons earlier in spite of their lower mobility, because the charge carriers are closer to each other. The hypothesis that charge carriers are trapped in defects in organic layers (that is, the charge traps) can explain that the t_0 becomes fast as degradation proceeds. As the amount of charge traps increases, the EL starts faster and t_0 decreases. The charge carriers trapped in the defect sites affect only the initial stage of luminescence and the luminescence saturation process (t_r) is affected only by the mobility of the charge carriers originating from the electrode. As expected, t_r tends to increase over degradation process, in our experiments, increasing by about 55 μs when the device is 66% degraded (Figure 2.4c).

t_d : The result that t_d increased by 1 μs with 66% degradation can be explained by the effect of the charge trap (Figer 2.4d). Electrons and holes trapped at close distances can cause delayed luminescence because they meet through diffusion even after voltage is turned off [51, 52]. Delayed luminescence due to the charge trap makes t_d longer. As the device is degraded, the number of charge traps increases and the amount of delayed luminescence also increases, leading

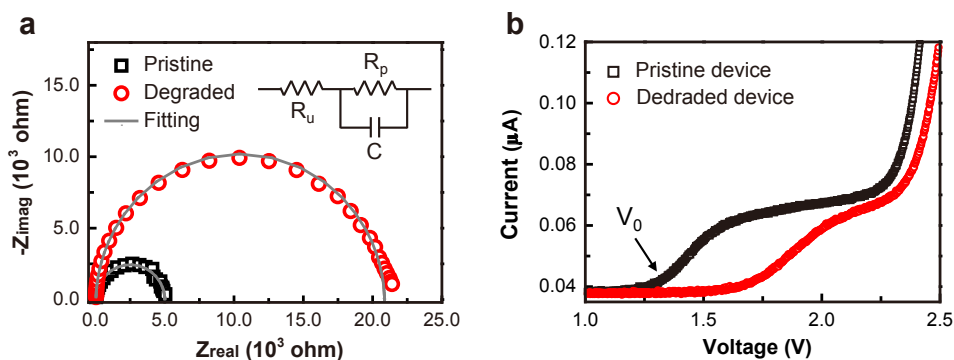


Figure 2.5 EIS and LSV results of OLED devices during degradation process. (a) Nyquist plot of pristine device (black square) and degraded device (red circle) obtained by EIS experiment. Assuming that the OLED devices are the circuit such as an inset, the internal resistance (R_p) of pristine device is $5.00 \cdot 10^3 \Omega$ and the R_p of 66% degraded device is $2.08 \cdot 10^4 \Omega$ according to the fitting result (gray line). (b) Voltage-current curve is measured at voltage before the current flows in the linear sweep voltammetry (LSV) experiment. Both pristine device (black line) and degraded device (red line) show V_0 (transient voltage), which suddenly increases current before the device starts operating. Degraded device has a higher V_0 than pristine device.

to a longer t_d . We observed that t_0 becomes faster and t_d becomes slower during degradation and concluded that the charge traps exist inside the organic layer and the number of traps increases with degradation.

Electric Experiments

We measured the capacitance of the OLED device depending on frequency of potential perturbation. Electrochemical impedance spectroscopy (EIS) results are represented in Nyquist plot, which shows the relationship between real part and imaginary part of capacitance (Figure 2.5a). The data at high frequency perturbation are located on the left side of the semicircle and the data at low frequency perturbation are located on the right side. OLED is typically assumed

as a constant phase element (CPE) circuit composed of two of resistors and a non-perfect capacitor (Figure 2.5a inset). R_u (uncompensated resistance), one of the resistors, refers the resistivity of interface between the electrode and the organic material. The other resistor R_p (polarization resistance) and C (non-perfect capacitor) wired in parallel mean resistivity of organic materials and the interfaces between the layers. Using CPE model, the left x intercept of the semicircle implies R_u , and the right x intercept is the sum of the resistance of two resistors (R_u and R_p). When the Nyquist plot is fitted to the CPE model, the R_u values, which are related with interfaces between organic and inorganic materials, are 25.4Ω and 34.9Ω in pristine and 66% degraded devices, respectively. The R_u values are relatively small, and the difference between pristine and degraded devices is not large. On the other hand, the internal resistance R_p , which is related to organic materials and the interfaces is different from R_u . R_p of pristine device is $5.00 \cdot 10^3 \Omega$ and the R_p of degraded device is $20.8 \cdot 10^3 \Omega$, which is more than four times larger than that of pristine device. Using EIS technique, we confirmed that the internal resistance (R_p) of the device increases as the device is degraded.

Figure 2.5b shows the result of measuring the current-voltage curve using the linear sweep voltammetry (LSV) technique. In this experiment, the applied voltage is ramped at a constant rate (40 V/s , forward scan), and the resulting current is recorded. A weak bump occurs in the current, and the bump moves to high voltage after degradation. If the OLED device does not contain the charge traps, in general, the current does not flow until the voltage reaches built-in voltage (V_{bi}), and increases immediately above V_{bi} .

In the study of Kondakov *et al.*, the bump is due to the charge traps of device. A micro current starts to flow at a transition voltage (V_0) that is lower than V_{bi} in the device with the charge traps. The field and the stored charge

vanish at V_0 . When the device has the charge traps, either electron or hole, the other charge carriers can be injected into device when voltage above V_0 is applied. It is also confirmed by the electrical method that the amount of charge traps inside the device increases when the device is degraded. We confirmed the existence of the charge traps by TREL and LSV experiments. TREL results show not only the existence of the charge traps but also the luminescence properties of the charge trap.

2.3.3 Luminescence Properties of the Charge Trap

We compare decay curves of TREL and TRPL to discuss the t_d in depth (Figure 2.6). Unlike the TREL experiment in which a voltage is applied to form an exciton, we use rectangular laser pulse to form an exciton in the TRPL experiment. When light is applied on device, the guest molecule is excited directly to form an exciton, so that no charge trap is formed. Only the intrinsic luminescence lifetime of the excitons can be measured using TRPL. The decay time of TRPL does not change significantly before and after degradation. The photoluminescence spectrum of the device also has the same shape and intensity in pristine and degraded device. It indicates that the dopant material ($\text{Ir}(\text{mphmq})_2(\text{acac})$) itself is not degraded. On the other hand, the t_d of TREL increased about 50% during degradation. The increase in t_d appears only in TREL experiments, not in TRPL experiments.

TRPL and TREL decays are not only different in lifetime but also in shape. The intrinsic luminescence lifetime of photo-generated excitons follows a single exponential function, while electro-generated excitons appears like a bi-exponential function. The electro-generated exciton has another emission path different from photo-generated exciton. Considering that TREL is measured by adding up to resistor-capacitor circuit time (rc time is typically 200–500

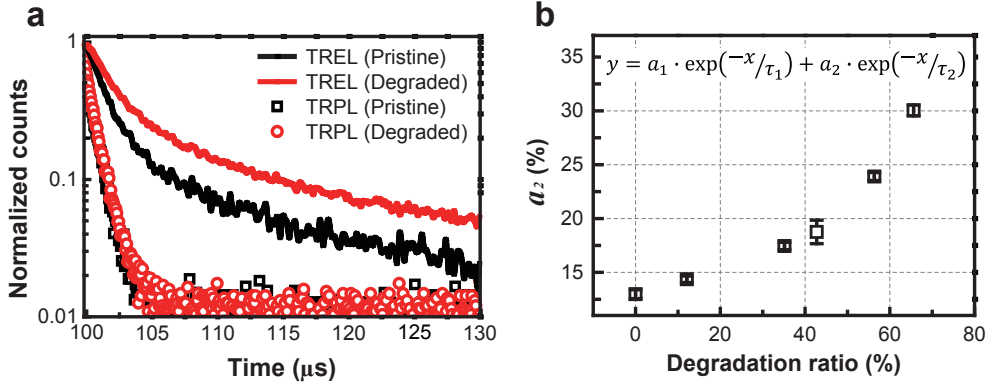


Figure 2.6 Decay curve analysis of OLED devices. (a) shows the result of comparing the decay curves of TRPL (shape) and TREL (line). The decay curves of TRPL do not differ between pristine (black shape) and degraded device (red shape) and follow a single-exponential decay in both cases. In TREL experiments, the decay lifetimes in degraded device (red line) become longer than those of pristine device (black line) and follow a bi-exponential decay in both cases. (b) When a TREL results are fitted with a bi-exponential function (inset), a_2 , which is the ratio of the delayed luminescence lifetime (τ_2), is plotted according to the degradation ratio. The a_2 increases as the device is degraded. The error bars are the standard deviations of the four experimental results.

ns [53].), we can say the short luminescence lifetime (τ_1) of TREL corresponds to t_{PL} of TRPL. This means τ_1 is luminescence through normal path. However, the long luminescence lifetime (τ_2) in TREL decay curve refers a delayed luminescence which is caused by the delayed recombination of the charge carriers trapped in defect sites (charge traps). Figure 2.6b shows the change of a_2 , which is the relative ratio of τ_2 in TREL fitting results. The a_2 means the amount of delayed luminescence and the increase in a_2 during degradation process intuitively shows the increase of the charge traps.

The luminescence behavior of defect can be confirmed by analyzing the change of t_d . Defects can act as luminescence quencher, non-radiative recom-

bination centers, and the charge traps [37]. The decreasing t_d means that a light-quenching material exists around the emitter when device is degraded. If the defect plays the role of non-radiative recombination center, t_d will not change since it does not affect the luminescent lifetime of the emitter. In this experiment, however, t_d increased in degraded device. This phenomenon can not be explained by the defects acting as luminescence quencher or non-radiative recombination center. Increased t_d indicates the presence of the charge traps that can decay with luminescence. (When the charge traps decay without luminescence, t_d does not change.) The change of t_d makes us estimate the behavior of the defects.

We designed the experiment to have much longer voltage off-time than the exciton's decay time. 1 ms off-time is long enough because the delayed luminescence lifetime by the charge traps, τ_2 , is only 5.85 μs . Even after delayed luminescence is completed during the off-time, t_0 gets faster by degradation. This means that the charge traps that can make early luminescence still exist after 1 ms. Even when the off-time increases to 4 ms, the same t_0 value is obtained as that in the case of 1 ms (Figure 2.7). It can be deduced that the charge traps that enable early luminescence (CT2) are different from the charge traps that cause delayed luminescence (CT1). CT1s can make luminescence with relatively low energy (thermal energy), and the lifetime is about 5.8 μs . On the other hand, CT2s are trapped in the defect unless external energy is applied, and the lifetime is much longer than 4 ms. In particular, the presence of the CT2s causing early luminescence has not been previously reported. Depending on the characteristics of the device, various types of the charge traps may exist. TREL results show that the effect on the device luminescence depends on the type of charge traps.

Figure 2.8 summarizes the effect of the charge traps on TREL curve. The

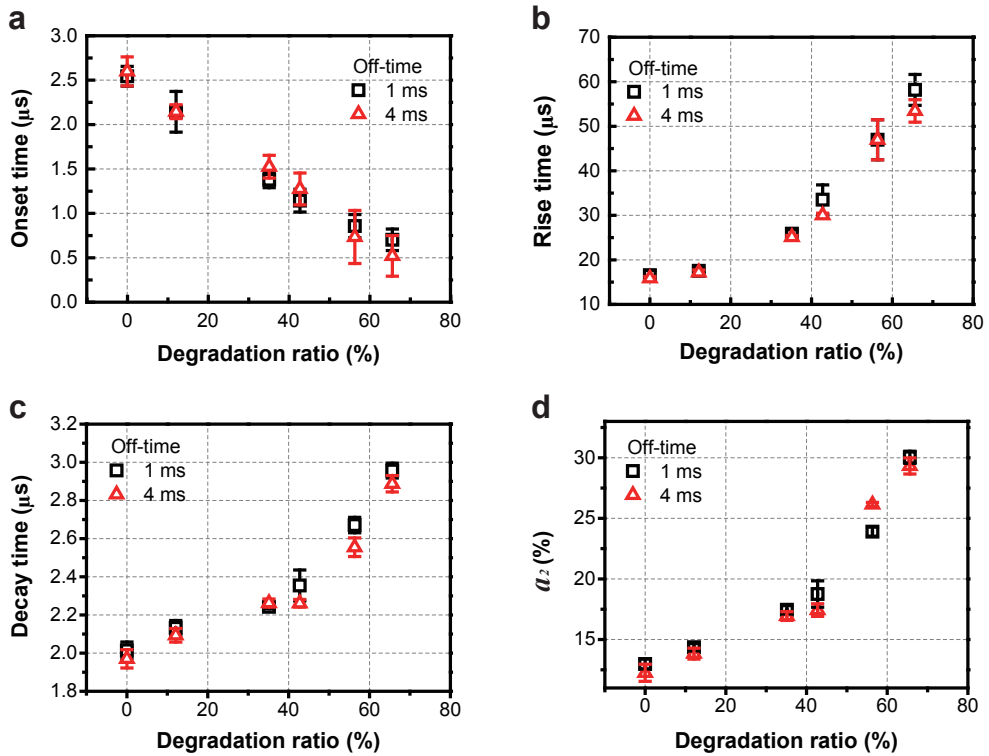


Figure 2.7 t_0 , t_r , t_d , and a_2 versus degradation ratio graph according to off-time. There is no significant difference in off-time. The error bars are the standard deviations of the four experimental results.

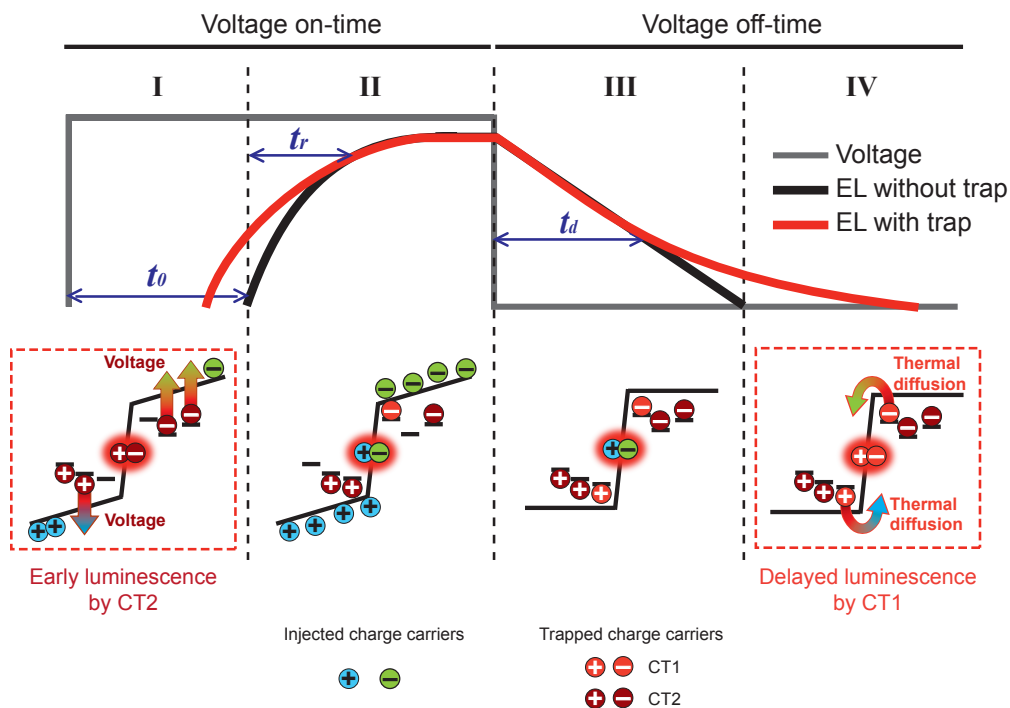


Figure 2.8 Schematic diagram of TREL experiments when the charge traps inside the OLED device. When the pulsed voltage (gray line) is applied, a black line-shaped EL appears when there is no charge trap, and a red line-shaped EL appears when there are radiative charge traps in the organic layers. In phase **II** and **III**, the EL is predominantly generated by injected charge carriers (yellow-green and sky blue). The luminescence in phase **I** and **IV** are caused by trapped charges. The luminescence in **IV** is caused by the CT1s (red) which can meet by thermal diffusion, whereas the luminescence in **I** is due to CT2s (dark red) which can escape by external voltage.

luminescence appearing in phase **I** and **IV** are generated by the charge traps. When the voltage is applied in phase **I**, trapped charge carriers (CT2) can escape from defects and meet earlier than charge carriers coming from electrodes. The luminescence processes in phase **II** and **III** are the same as those of pristine device without trap (Figure 2.3). Trapped charge carriers in defects with relatively low energy barrier (CT1) induce delayed luminescence through thermal diffusion (**IV**). The phenomena that occur in phase **I** and **IV** are caused by the charge traps, but it seems that there are differences in the types of the charge traps that cause two phenomena.

We investigated that the charge traps are inside the device through the analysis of three time components (t_0 , t_r , and t_d) from TREL curve as the device is degraded. We also investigate how the charge trap can affect the EL. It was observed that the charge traps caused an early luminescence at the initial stage of the voltage supply and a delayed luminescence after the voltage is turned off. TREL technique is a simple experimental method that can confirm the presence of the charge traps intuitively. The optical characteristics of the charge traps in the OLED device can be fully analyzed using TREL technique.

2.4 Conclusion

We observed the existence of the charge traps in the OLED device by the spectroscopic method and investigated its luminescence properties while the device was being degraded. During the degradation, OLED device shows several phenomena that can be explained only by the charge traps among Giebink's three kinds of defects [37] in TREL experiments. When the device is degraded, t_r increases as expected, but t_0 decreases, even though the mobility of the charge carriers is slowed down. Some of charge carriers trapped in the defects are able

to form excitons faster than charge carriers originating from the electrodes because they are close to each other. Therefore, t_0 decreases as the charge traps increase. Furthermore, another kinds of electron and hole traps are able to form excitons even after the voltage is turned off, which cause delayed luminescence. As the degradation proceeds, the amount of the charge traps increases, which indicates a decrease in t_0 and an increase in t_d . The a_2 , the ratio of delayed luminescence, increases with degradation. Because the charge traps exist only when electro-excited, a_2 does not appear in PL decay, but only in EL decay.

We developed the TREL experiment, which have been used for the measurement of the charge carrier mobility, into the technique that is capable of identifying the charge traps in the device. The presence of the charge traps is confirmed directly by time-resolved spectroscopy. Because TREL observes light, the effect of the charge traps is able to be confirmed via luminescence, unlike other electrical techniques that can observe charge traps. Moreover, we elucidate the phenomenon that the charge traps affect an early luminescence after the voltage is applied as well as the phenomenon that the charge traps cause a delayed luminescence. The understanding of these phenomena of the charge traps are able to be applied to the development of a new concept device in order to increase the repetition rate of the OLED device.

In situ charge trap analysis of a light emitting device can be utilized not only to study the degradation mechanism of the device, but also to confirm a new luminescence characteristic of the optoelectronic device. It also contributes to the development of a new level of light emitting device. Furthermore, this technique can contribute to the development of optoelectronics.

Chapter 3

Non-invasive and Layer-selective Analysis of OLED Degradation Process

3.1 Introduction

As mentioned in previous chapters, it is important to understand the degradation mechanism of OLEDs. The lifetime of the device can be improved by knowing which part of the device is responsible for the degradation process. It is investigated in various ways to figure out the origin of the degradation of OLED device. Matrix assisted laser desorption/ionization time-of-flight mass spectrometry (MALDI-TOF-MS) [54,55], high performance liquid chromatography (HPLC) coupled with UV absorption or MS [29,35] are typical methods for identifying chemical degradation of materials [3]. The change in the surface of the device can be observed by atomic force microscopy (AFM) [56–59], scanning tunneling microscopy (STM) [60], X-ray (XPS) [61–64] or ultraviolet (UPS) [65] photoelectron spectroscopy [3]. However it is impossible to observe

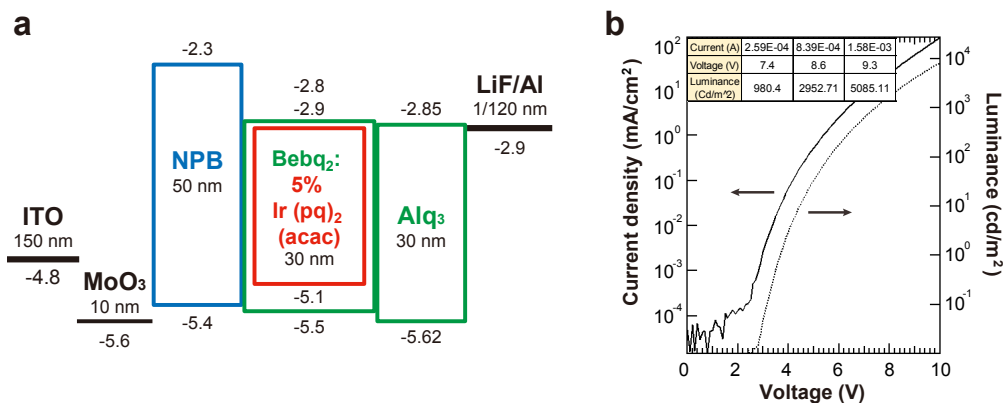


Figure 3.1 Fabricated red phosphorescent OLED device and its luminescence properties. (a) Schematic energy band diagram of red phosphorescent OLED device. MoO₃ is included to facilitate injection of holes. The energy levels of LUMO and HOMO are written in units of eV. (b) J-V-L curves of fabricated red phosphorescent OLEDs.

the degradation process in real time because these measurements cause a direct deformation of the device.

On the other hand, the optical method allows *in situ* measurement of the emission states of materials, but it is difficult to observe each layer because of an optical resolution limit (several hundred nm). Here, we proposed a new optical method that can identify which layer causes degradation. The optical method spectrally resolves each layer that can not be spatially resolved. We showed the feasibility of this new optical method with a four-layer OLED device.

3.2 Materials and Methods

3.2.1 OLED Fabrication

The exact device configuration used in this work was indium tin oxide (ITO, 150 nm)/MoO₃ (10 nm)/N,N'-Di(1-naphthyl)-N,N'-diphenyl-(1,1'-biphenyl)-4,4'-diamine (NPB, 50 nm)/Bis(10-hydroxy benzo[h]quinolinato)beryllium (Bebq₂):

(2,4-Pentanedionato)bis[2-(2-quinoliny)phenyl]iridium(III) ($\text{Ir}(\text{pq})_2(\text{acac})$) (30 nm)/ Tris-(8-hydroxyquinoline)aluminum (Alq_3 , 30 nm)/Lithium fluoride (LiF , 1 nm)/ Aluminum (Al , 120 nm) (Figure 3.1a). Organic materials were purchased from Luminescence Technology Corp. (Lumtec). Line patterns of ITO were formed on glass by photolithography process. All organic materials were deposited by the vacuum evaporation. The fabricated OLED devices were encapsulated with a sealing glass and a UV curable resin in a nitrogen atmosphere to prevent contact with moisture and oxygen in the air. The J-V-L data of the OLEDs were measured using a sourcemeter (236, Keithley) (Figure 3.1b). The fabricated devices were electrically degraded by applying constant 6 V DC voltage using DC power supply (E3620A, Agilent).

3.2.2 Luminescence Intensity and Lifetime Measurements

Fluorescence lifetime and steady state spectrometer (GB/FLSP920, Edinburgh instruments) combined with picosecond pulsed diode laser (EPL-375, Edinburgh instruments) were used for intensity and lifetime measurements. A few μW of 375 nm light source did not cause photodegradation of OLED. Monochromator in the spectrometer divided the wavelengths into 420, 530, and 600 nm for NPB (HTL), Alq_3 (ETL), and $\text{Ir}(\text{pq})_2(\text{acac})$ (guest), respectively. The intensities and lifetimes of each material are measured at the corresponding wavelength. Data were acquired for 10 seconds for accurate measurement of photoluminescence (PL) and electroluminescence (EL) intensities followed by accumulation up to 3000 peak counts (100 ns pulse period) and 1000 peak counts (10 μs pulse period) for fluorescence and phosphorescence lifetime measurements, respectively.

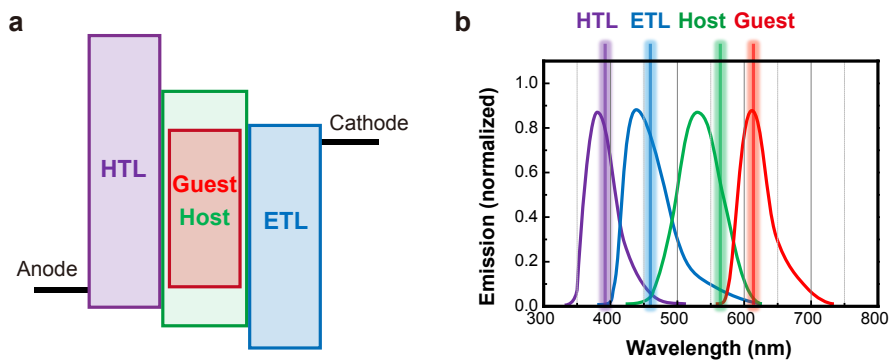


Figure 3.2 Device design that allows layer selective observation. When the bandgaps of layers are different, each layer can be spectrally resolved.

3.3 Results and Discussion

3.3.1 Experimental Concept for Layer Selective Degradation Analysis

An optical method is suitable for non-invasive observation of the device. However, even with the advanced techniques such as confocal microscope, the optical detection method can not spatially resolve an each layer because of the limited resolution. Therefore, we constructed the OLED with layers having different bandgaps to separate each layer by spectra (Figure 3.2).

In order to demonstrate the feasibility of the concept, we chose NBP (HTL, 3.1 eV), Alq₃ (ETL, 2.77 eV), and Ir(pq)₂acac (guest, 2.2 eV). The host material, Bebq₂ has 2.7 eV bandgap similar to Alq₃. However Bebq₂ is invisible in luminescence spectroscopy because its energy is totally transferred to a guest material. We can resolve HTL, ETL, and a guest material by the spectral difference. HTL, ETL, host, and guest were excited simultaneously by 375 nm laser, but were detected separately by a monochromator.

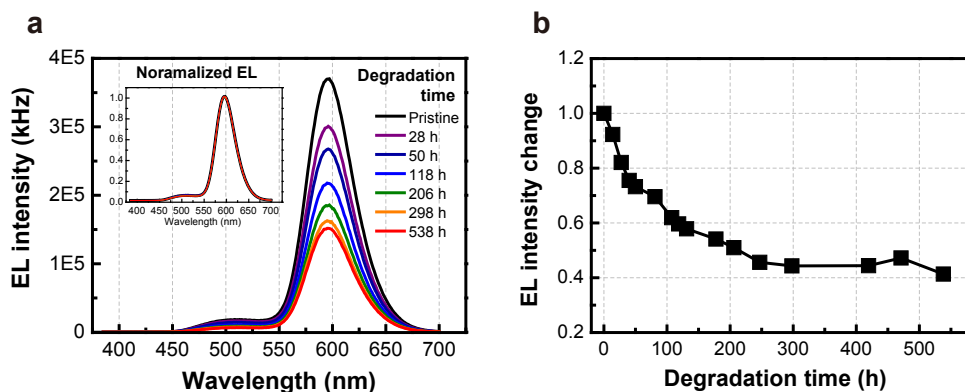


Figure 3.3 Change in electroluminescence (EL) intensity during degradation. (a) Spectra decreased but did not change in shape. (Inset: normalized EL spectra) (b) EL intensities at 600 nm decreased as degradation time. A rapid decrease in intensity was observed before 300 h.

3.3.2 Determining Which Layer is Degraded

The electroluminescence (EL) intensity gradually decreased over time when a constant voltage (6 V) was applied, which means the device was degraded. The intensity of the EL spectra decreased, but the shape of the EL spectra did not change (Figure 3.3a and inset). This indicates that new molecules, having different spectrum, were not generated. When the device was driven for about 300 hours, the EL intensity decreased by 60% (Figure 3.3b).

On the other hand, during the same electro-degradation time, the photoluminescence (PL) intensities and lifetimes of three materials were only slightly changed (Figure 3.4). PL intensities decreased after 400 hours but the difference is very small compared to the change of EL intensity. Among the three materials, the guest material appeared to be the most damaged. Figure 3.4c-d shows the change of PL lifetime that is similar to the change of PL intensity. The intensity and lifetime of the guest material decreased after 400 hours, indicating

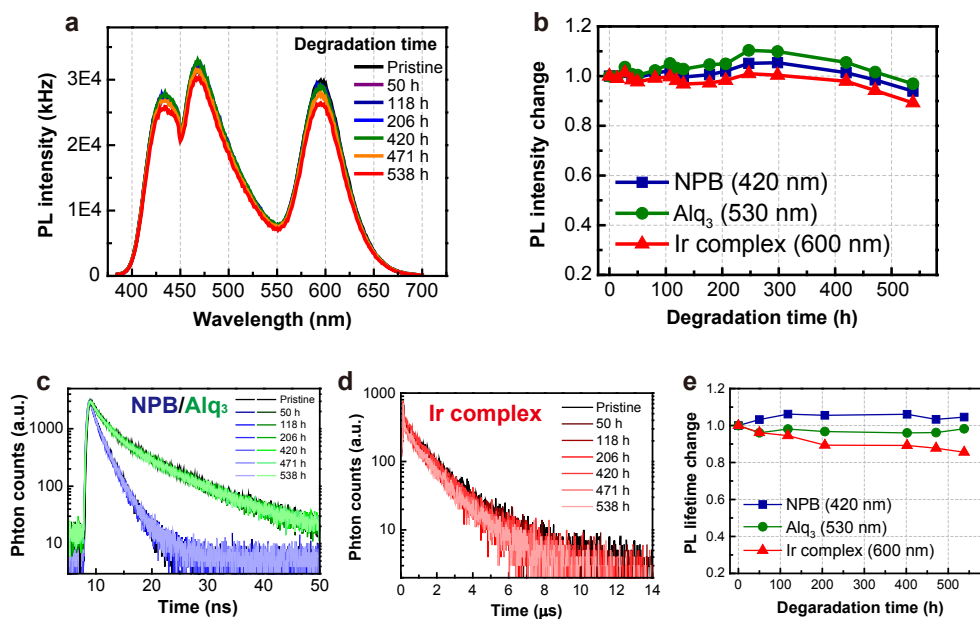


Figure 3.4 Change in photoluminescence (PL) intensity and lifetime of HTL, ETL, and guest materials during degradation. (a) Spectra did not decrease so much nor change in shape. (b) PL intensity of HTL, ETL, and guest materials started to decrease after 400 h. (c,d) show the decay curves of HTL, ETL, and guest materials. More degraded devices are displayed in more bright color. (e) PL lifetime of HTL, ETL did not change much. PL lifetime of guest materials were reduced by about 20% over 500 h degradation. HTL, ETL, and guest materials are represented in blue, green, and red color, respectively.

that $\text{Ir}(\text{pq})_2(\text{acac})$ is degraded.

In the beginning of the observation, the change of the PL intensities and lifetimes was not observed from HTL, ETL and guest molecules. Therefore, the degradation of EL intensity cannot be elucidated by the change of materials. There is a possibility of defect at the interface which might affect the decrease of EL intensity. Although interface is composed of a much smaller quantity compared to the entire layer and has no significant effect on PL, it has a crucial effect on EL. It can be explained that the cause of the degradation of the device is caused by the difficulty of charge carrier injection at interface rather than chemical decomposition of the organic material [66–68]. Another cause of the rapid degradation can be proposed as the effect of quencher which is assumed to be polaron quencher because it was activated only when voltage was applied. Some researchers have been reported that exciton (or triplet) polaron annihilation (EPA or TPA) is the cause of the degradation [66–68]. Decrease in PL intensity and lifetime after 400 h indicates the start of chemical degradation of the bulk material, however, the chemical degradation does not affect substantially the EL intensity.

Additionally, there are a few things to complement in this experiment. The EL intensity decay is also affected by the reduction of applied current. The reason why a number of excitons are reduced over time is complicated. Therefore, in order to eliminate the influence of the internal resistance, the device is degraded in constant current mode. It is necessary to compare the results of EL (at a constant current) with the results of PL. Few other additional experiments are necessary to reveal the specific cause of the degradation. In this experiment, excitation source was 375 nm that limited the material selection, but the shorter wavelength of laser will allow to observe a broader range of materials.

The bandgap of each layer was intentionally manipulated with a high degree of diversity in this experiment. When the emission spectra (i. e., bandgap) are overlapped between the layers of the OLED device, the layers can be separated using a linear unmixing method which is used for spectral imaging in fluorescence microscopy. A reliable separation of the layers is required for analysis and quantitation, but it is complicated by the significant overlap of the bandgaps of layers [69]. Linear unmixing method allows the reliable separation of even strongly overlapping emission spectra. It is based on the assumption that the total detected signal S for every channel of wavelength (λ) can be expressed as a linear combination of the contributing layers. $S(\lambda) = \Sigma A_i \cdot L_i(\lambda)$ where A_i and L_i represents the amount of contribution by specific layer and the reference emission spectra of the layer. A_i is determined by calculating contribution values that most closely matches the detected signals in the channels [69]. By adding the linear unmixing method to our new optical analysis, it can be universally applied to a device composed of layers having similar bandgaps.

Even though the layer-specific degradation of the device was not fully understood through this optical method, there is an importance of building a new technique that can diagnose the degradation of a material *in situ*. The method has a great advantage of diagnosing the degradation of a material non-invasively unlike other chemical analysis methods. This optical method also has another advantage of observing the luminescence. When we apply the technique to other OLEDs, such as OLED using thermally activated delayed fluorescence (TADF) material, blue phosphorescent OLED, or OLED in high current, we can use the technique to determine which layers or materials are degraded.

3.4 Conclusion

We developed a new technique that can overcome optical resolution limit by spectrally resolving the bandgap, so that we could examine the layers of OLED respectively. Using the method, we can verify the optical change of materials in OLED layer-selectively and observe each layer in real time to discover the degradation mechanism. In our experiments, there is no correlation between the break down of a molecule and the initial device degradation shown by EL intensity although the guest material, Ir(pq)₂(acac), seems to be degraded after 400 h. It can be concluded that the degradation of a molecule was not observed but rather other factors such as interface failure or polaron quencher caused degradation, which requires a few additional control experiments to prove the exact the factor. This technique, which can efficiently investigate the luminescence properties of a material without destroying the device, can be used in other OLED devices to diagnose chemical degradation.

Bibliography

- [1] M. Pope, H. P. Kallmann, and P. Magnante. Electroluminescence in organic crystals. *The Journal of Chemical Physics*, 38(8):2042–2043, 1963.
- [2] W. Helfrich and W. G. Schneider. Recombination radiation in anthracene crystals. *Physical Review Letters*, 14(7):229, 1965.
- [3] Sebastian Scholz, Denis Kondakov, Björn Lüssem, and Karl Leo. Degradation mechanisms and reactions in organic light-emitting devices. *Chemical Reviews*, 115(16):8449–8503, 2015.
- [4] P. S. Vincett, W. A. Barlow, R. A. Hann, and G. G. Roberts. Electrical conduction and low voltage blue electroluminescence in vacuum-deposited organic films. *Thin Solid Films*, 94(2):171–183, 1982.
- [5] R. H. Partridge. Electroluminescence from polyvinylcarbazole films: 1. carbazole cations. *Polymer*, 24(6):733–738, 1983.
- [6] Ching W. Tang and Steven A. VanSlyke. Organic electroluminescent diodes. *Applied Physics Letters*, 51(12):913–915, 1987.
- [7] Man-Keung Fung, Chun-Sing Lee, and Shuit-Tong Lee. Metal/polymer interface studies for organic light-emitting devices. *Organic Light Emitting Devices: Synthesis, Properties and Applications*, pages 181–214, 2006.
- [8] Stefan Kappaun, Christian Slugovc, and Emil J. W. List. Phosphorescent organic light-emitting devices: Working principle and iridium based emitter materials. *International Journal of Molecular Sciences*, 9(8):1527–1547, 2008.

- [9] Rico Meerheim, Karsten Walzer, Martin Pfeiffer, and Karl Leo. Ultrastable and efficient red organic light emitting diodes with doped transport layers. *Applied Physics Letters*, 89(6):061111, 2006.
- [10] Sebastian Reineke, Frank Lindner, Gregor Schwartz, Nico Seidler, Karsten Walzer, Björn Lüssem, and Karl Leo. White organic light-emitting diodes with fluorescent tube efficiency. *Nature*, 459(7244):234–238, 2009.
- [11] Antti Laaperi. OLED lifetime issues from a mobile-phone-industry point of view. *Journal of the Society for Information Display*, 16(11):1125–1130, 2008.
- [12] Marc A. Baldo, D. F. O’Brien, Y. You, A. Shoustikov, S. Sibley, Mark E. Thompson, and Stephen R. Forrest. Highly efficient phosphorescent emission from organic electroluminescent devices. *Nature*, 395(6698):151–154, 1998.
- [13] Chihaya Adachi, Marc A. Baldo, Mark E. Thompson, and Stephen R. Forrest. Nearly 100% internal phosphorescence efficiency in an organic light-emitting device. *Journal of Applied Physics*, 90(10):5048–5051, 2001.
- [14] D. F. O’Brien, M. A. Baldo, Mark E. Thompson, and Stephen R. Forrest. Improved energy transfer in electrophosphorescent devices. *Applied Physics Letters*, 74(3):442–444, 1999.
- [15] Bernard Geffroy, Philippe Le Roy, and Christophe Prat. Organic light-emitting diode (OLED) technology: materials, devices and display technologies. *Polymer International*, 55(6):572–582, 2006.
- [16] Yutaka Ohmori, Akihiko Fujii, Masao Uchida, Chikayoshi Morishima, and Katsumi Yoshino. Observation of spectral narrowing and emission energy shift in organic electroluminescent diode utilizing 8-hydroxyquinoline aluminum/aromatic diamine multilayer structure. *Applied Physics Letters*, 63(14):1871–1873, 1993.
- [17] Hartmut Yersin. Triplet emitters for OLED applications. mechanisms of exciton trapping and control of emission properties. *Transition Metal and Rare Earth Compounds*, pages 1–26, 2004.
- [18] J. Frenkel. On the transformation of light into heat in solids. I. *Physical Review*, 37(1):17, 1931.
- [19] W. Y. Liang. Excitons. *Physics Education*, 5(4):226, 1970.
- [20] Dino A. Pardo, Ghassan E. Jabbour, and Nasser Peyghambarian. Application of screen printing in the fabrication of organic light-emitting devices. *Advanced Materials*, 12(17):1249–1252, 2000.

- [21] G. Gustafsson, Y. Cao, G. M. Treacy, F. Klavetter, N. Colaneri, and A. J. Heeger. Flexible light-emitting diodes made from soluble conducting polymers. *Nature*, 357(6378):477–479, 1992.
- [22] Junji Kido, Masato Kimura, Katsutoshi Nagai, *et al.* Multilayer white light-emitting organic electroluminescent device. *Science*, 267:1332–1332, 1995.
- [23] Susanna Schmidbauer, Andreas Hohenleutner, and Burkhard König. Chemical degradation in organic light-emitting devices: Mechanisms and implications for the design of new materials. *Advanced Materials*, 25(15):2114–2129, 2013.
- [24] Hany Aziz and Zoran D. Popovic. Degradation phenomena in small-molecule organic light-emitting devices. *Chemistry of Materials*, 16(23):4522–4532, 2004.
- [25] Yoshiharu Sato, Shoko Ichinosawa, and Hiroyuki Kanai. Operation characteristics and degradation of organic electroluminescent devices. *IEEE Journal of Selected Topics in Quantum Electronics*, 4(1):40–48, 1998.
- [26] Zoran D. Popovic and Hany Aziz. Reliability and degradation of small molecule-based organic light-emitting devices (OLEDs). *IEEE Journal of Selected Topics in Quantum Electronics*, 8(2):362–371, 2002.
- [27] Hossein Zamani Siboni and Hany Aziz. Causes of driving voltage rise in phosphorescent organic light emitting devices during prolonged electrical driving. *Applied Physics Letters*, 101(17):173502, 2012.
- [28] Denis Y. Kondakov. The role of homolytic reactions in the intrinsic degradation of OLEDs. *Organic Electronics: Materials, Processing, Devices and Applications*, page 211, 2009.
- [29] Denis Y. Kondakov, W. C. Lenhart, and W. F. Nichols. Operational degradation of organic light-emitting diodes: Mechanism and identification of chemical products. *Journal of Applied Physics*, 101(2):024512, 2007.
- [30] Denis Y. Kondakov. Role of chemical reactions of arylamine hole transport materials in operational degradation of organic light-emitting diodes. *Journal of Applied Physics*, 104(8):084520, 2008.
- [31] Sebastian Scholz, Karsten Walzer, and Karl Leo. Analysis of complete organic semiconductor devices by laser desorption/ionization time-of-flight mass spectrometry. *Advanced Functional Materials*, 18(17):2541–2547, 2008.
- [32] Rico Meerheim, Sebastian Scholz, Selina Olthof, Gregor Schwartz, Sebastian Reineke, Karsten Walzer, and Karl Leo. Influence of charge balance and exciton distribution

- on efficiency and lifetime of phosphorescent organic light-emitting devices. *Journal of Applied Physics*, 104(1):014510, 2008.
- [33] Sebastian Scholz, Björn Lüssem, and Karl Leo. Chemical changes on the green emitter tris(8-hydroxy-quinolino) aluminum during device aging of *p-i-n*-structured organic light emitting diodes. *Applied Physics Letters*, 95(18):293, 2009.
- [34] Leonard J. Soltzberg, Jason D. Slinker, Samuel Flores-Torres, Daniel A. Bernards, George G. Malliaras, Hector D. Abruña, Ji-Seon Kim, Richard H. Friend, Michael D. Kaplan, and Velda Goldberg. Identification of a quenching species in ruthenium tris-bipyridine electroluminescent devices. *Journal of the American Chemical Society*, 128(24):7761–7764, 2006.
- [35] Varatharajan Sivasubramaniam, Florian Brodkorb, Stephanie Hanning, Hans Loebel, Volker Elsbergen, Herbert Boerner, Ullrich Scherf, and Martin Kreyenschmidt. Investigation of FIrpic in PhOLEDs via LC/MS technique. *Open Chemistry*, 7(4):836–845, 2009.
- [36] Franky So and Denis Kondakov. Degradation mechanisms in small-molecule and polymer organic light-emitting diodes. *Advanced Materials*, 22(34):3762–3777, 2010.
- [37] N. C. Giebink, B. W. D’andrade, M. S. Weaver, P. B. Mackenzie, J. J. Brown, Mark E. Thompson, and Stephen R. Forrest. Intrinsic luminance loss in phosphorescent small-molecule organic light emitting devices due to bimolecular annihilation reactions. *Journal of Applied Physics*, 103(4):044509, 2008.
- [38] Zoran D. Popovic, Hany Aziz, Andronique Ioannidis, Nan-Xing Hu, and Paulo N.M. dos Anjos. Time-resolved fluorescence studies of degradation in tris (8-hydroxyquinoline) aluminum (ALQ₃)-based organic light emitting devices (OLEDs). *Synthetic Metals*, 123(1):179–181, 2001.
- [39] Tobias D. Schmidt, Lars Jäger, Yutaka Noguchi, Hisao Ishii, and Wolfgang Brütting. Analyzing degradation effects of organic light-emitting diodes via transient optical and electrical measurements. *Journal of Applied Physics*, 117(21):215502, 2015.
- [40] Stefan Nowy, Wei Ren, Andreas Elschner, Wilfried Lövenich, and Wolfgang Brütting. Impedance spectroscopy as a probe for the degradation of organic light-emitting diodes. *Journal of Applied Physics*, 107(5):054501, 2010.
- [41] Stefan Berleb, Wolfgang Brütting, and Gernot Paasch. Interfacial charges and electric field distribution in organic hetero-layer light-emitting devices. *Organic Electronics*, 1(1):41–47, 2000.

- [42] Denis Y. Kondakov, James R. Sandifer, Ching Wan Tang, and Ralph H. Young. Non-radiative recombination centers and electrical aging of organic light-emitting diodes: Direct connection between accumulation of trapped charge and luminance loss. *Journal of Applied Physics*, 93(2):1108–1119, 2003.
- [43] Denis Y. Kondakov. Direct observation of deep electron traps in aged organic light emitting diodes. *Journal of Applied Physics*, 97(2):024503, 2005.
- [44] Thien-Phap Nguyen, C. Renaud, P. Le Rendu, and S. H. Yang. Investigation of defects in organic semiconductors by charge based deep level transient spectroscopy (Q-DLTS). *physica status solidi (c)*, 6(8):1856–1861, 2009.
- [45] Chishio Hosokawa, Hiroshi Tokailin, Hisahiro Higashi, and Tadashi Kusumoto. Transient behavior of organic thin film electroluminescence. *Applied Physics Letters*, 60(10):1220–1222, 1992.
- [46] Mark A. Baldo and Stephen R. Forrest. Transient analysis of organic electrophosphorescence: I. Transient analysis of triplet energy transfer. *Physical Review B*, 62(16):10958, 2000.
- [47] Marc A. Baldo, Chihaya Adachi, and Stephen R. Forrest. Transient analysis of organic electrophosphorescence. II. Transient analysis of triplet-triplet annihilation. *Physical Review B*, 62(16):10967, 2000.
- [48] S. Barth, P. Müller, H. Riel, P. F. Seidler, W. Riess, H. Vestweber, and H. Bässler. Electron mobility in tris(8-hydroxy-quinoline) aluminum thin films determined via transient electroluminescence from single-and multilayer organic light-emitting diodes. *Journal of Applied physics*, 89(7):3711–3719, 2001.
- [49] T. C. Wong, J. Kovac, C. S. Lee, L. S. Hung, and S. T. Lee. Transient electroluminescence measurements on electron-mobility of *N*-arylbenzimidazoles. *Chemical Physics Letters*, 334(1):61–64, 2001.
- [50] Do Han Kim, Nam Sung Cho, Hyoung-Yun Oh, Joong Hwan Yang, Woo Sik Jeon, Jung Soo Park, Min Chul Suh, and Jang Hyuk Kwon. Highly efficient red phosphorescent dopants in organic light-emitting devices. *Advanced Materials*, 23(24):2721–2726, 2011.
- [51] Zoran D. Popovic and Hany Aziz. Delayed electroluminescence in small-molecule-based organic light-emitting diodes: Evidence for triplet-triplet annihilation and recombination-center-mediated light-generation mechanism. *Journal of Applied Physics*, 98(1):013510, 2005.
- [52] Subrata Sinha and A. P. Monkman. Delayed recombination of detrapped space-charge carriers in poly [2-methoxy-5-(2'-ethyl-hexyloxy)-1,4-phenylene vinylene]-based light-emitting diode. *Journal of Applied Physics*, 97(11):114505, 2005.

- [53] Hartmut Yersin. *Highly efficient OLEDs with phosphorescent materials*. John Wiley & Sons, 2008.
- [54] Koichi Tanaka, Hiroaki Waki, Yutaka Ido, Satoshi Akita, Yoshikazu Yoshida, Tamio Yoshida, and T. Matsuo. Protein and polymer analyses up to m/z 100 000 by laser ionization time-of-flight mass spectrometry. *Rapid Communications in Mass Spectrometry*, 2(8):151–153, 1988.
- [55] Michael Karas, Doris Bachmann, U. Bahr, and Franz Hillenkamp. Matrix-assisted ultraviolet laser desorption of non-volatile compounds. *International Journal of Mass Spectrometry and Ion Processes*, 78:53–68, 1987.
- [56] Lee-M Do, Mitsuaki Oyamada, Amane Koike, Eun-M Han, Noritaka Yamamoto, and Masamichi Fujihira. Morphological change in the degradation of Al electrode surfaces of electroluminescent devices by fluorescence microscopy and AFM. *Thin Solid Films*, 273(1-2):209–213, 1996.
- [57] Ki-Beom Kim, Yoon-Heung Tak, Yoon-Soo Han, Kwang-Heum Baik, Myung-Hee Yoon, and Moon-Ho Lee. Relationship between surface roughness of indium tin oxide and leakage current of organic light-emitting diode. *Japanese Journal of Applied Physics*, 42(4B):L438, 2003.
- [58] M. S. Xu, J. B. Xu, and J. An. Visualization of thermally activated morphology evolution of N, N' -di(naphthalene-1-yl)- N, N' -dipthalbenzidine films on ITO/copper phthalocyanine underlying layer. *Applied Physics A: Materials Science & Processing*, 81(6):1151–1156, 2005.
- [59] Eun-Mi Han, Lee-Mi Do, Noritaka Yamamoto, and Masamichi Fujihira. Crystallization of organic thin films for electroluminescent devices. *Thin Solid Films*, 273(1-2):202–208, 1996.
- [60] Jian-Ru Gong, Li-Jun Wan, Sheng-Bin Lei, Chun-Li Bai, Xiao-Hong Zhang, and Shuit-Tong Lee. Direct evidence of molecular aggregation and degradation mechanism of organic light-emitting diodes under joule heating: an STM and photoluminescence study. *The Journal of Physical Chemistry B*, 109(5):1675–1682, 2005.
- [61] S. Olthof, R. Meerheim, M. Schober, and K. Leo. Energy level alignment at the interfaces in a multilayer organic light-emitting diode structure. *Physical Review B*, 79(24):245308, 2009.
- [62] D. Grozea, A. Turak, X. D. Feng, Z. H. Lu, D. Johnson, and R. Wood. Chemical structure of Al/LiF/Alq interfaces in organic light-emitting diodes. *Applied Physics Letters*, 81(17):3173–3175, 2002.

- [63] S. Gardonio, L. Gregoratti, P. Melpignano, L. Aballe, V. Biondo, R. Zamboni, M. Murgia, S. Caria, and M. Kiskinova. Degradation of organic light-emitting diodes under different environment at high drive conditions. *Organic Electronics*, 8(1):37–43, 2007.
- [64] Qi Wang, Graeme Williams, Ting Tsui, and Hany Aziz. Photochemical deterioration of the organic/metal contacts in organic optoelectronic devices. *Journal of Applied Physics*, 112(6):064502, 2012.
- [65] A. Rajagopal and A. Kahn. Photoemission spectroscopy investigation of magnesium–Alq₃ interfaces. *Journal of applied physics*, 84(1):355–358, 1998.
- [66] Qi Wang, Iain W. H. Oswald, Michael R. Perez, Huiping Jia, Bruce E. Gnade, and Mohammad A. Omary. Exciton and polaron quenching in doping-free phosphorescent organic light-emitting diodes from a Pt(II)-based fast phosphor. *Advanced Functional Materials*, 23(43):5420–5428, 2013.
- [67] N. C. Giebink, B. W. D’Andrade, M. S. Weaver, J. J. Brown, and S. R. Forrest. Direct evidence for degradation of polaron excited states in organic light emitting diodes. *Journal of Applied Physics*, 105(12):124514, 2009.
- [68] Qi Wang and Hany Aziz. Degradation of organic/organic interfaces in organic light-emitting devices due to polaron–exciton interactions. *ACS Applied Materials & Interfaces*, 5(17):8733–8739, 2013.
- [69] Timo Zimmermann. Spectral imaging and linear unmixing in light microscopy. *Microscopy Techniques*, pages 1308–1310, 2005.
- [70] Nancy L. Thompson. *Fluorescence correlation spectroscopy*. Springer, 2002.

Appendix A

Molar Concentration Measurement and Bio-imaging Application of ZAIS/ZnS Core/Shell Nanocrystals

A.1 Introduction

Semiconductor nanocrystals (NCs) with fluorescence, which are also called quantum dots (QDs), have been widely used in solar cell, photocatalysts, and biological application because they have an excellent and unique optical properties. They have robust photostability and high absorption coefficient, and their fluorescence wavelengths can easily be adjusted depending on their size or composition [1–3]. Many researchers were initially focused on II-VI based QDs such as CdSe because of their rapid synthesis method and excellent optical properties. However, the application of QDs have been limited by the toxic effects of heavy metals on humans and the environment [4–6].

III-V and I-III-VI based semiconductor NCs such as InP/ZnS, CuInS₂, AgInS₂, and ZnS-AgInS₂ (ZAIS) have replaced cadmium based QDs [7–11].

Cadmium-free NCs are not toxic but have a disadvantage of low fluorescence quantum yield. The formation of shell layer with wide band gap such as ZnS (3.68 eV) was a good solution for improvement of quantum yields.

Various synthetic approach for formation of ZnS shell layer have been studied. Formation of ZnS layer has been mostly achieved by thermal reaction in organic solvent or water, hydrothermal reaction, ultrasound, and microwave reaction. In this study, we fabricate the core-shell NCs using ultrasound technique, which is an easy and simple method.

For general application of NCs, it is important to know the molar concentration and molecular extinction coefficient that allows for a reproducible concentration measurement. When NCs are used to label biomolecules, for example, their concentration is essential to control the number of biomolecules that are conjugated at the NC surface [12]. Although concentrations of metal element are determined by various measurement techniques such as atomic emission spectroscopy (AES), atomic absorption spectroscopy (AAS), UV-Vis spectroscopy, and MALDI-TOF mass spectroscopy, it is difficult to determine the exact molar concentration for NCs [13,14].

Fluorescence correlation spectroscopy (FCS) is a sensitive and non-invasive detection technique using statistical analysis of the fluctuations of the fluorophores in small observation volume [15,16]. This technique has been successfully used to characterize hydrodynamic diameters and surface charges of organic and aqueous QDs [17–20]. The FCS method has applied to measure the concentration of QDs based on the amplitude of their autocorrelation curves and detection volume [21,22]. We measured the averaged molar concentration and extinction coefficient of aqueous ZAIS/ZnS NCs using FCS. The concentration of NC was quantified and applied to imaging experiments.

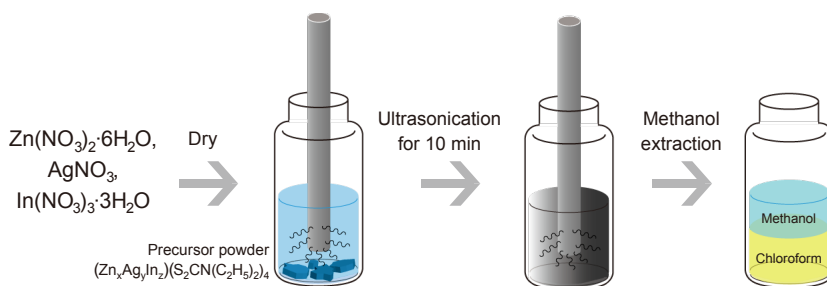


Figure A.1 Synthesis process of ZAIS NCs using ultrasound technique.

A.2 Materials and Methods

A.2.1 Synthesis of ZAIS and ZAIS/ZnS NCs

We introduce a novel strategy for fast synthesis of high quality ZAIS and ZAIS/ZnS NCs. The detail process for synthesis of ZAIS core was reported previous work [11]. 0.1 g metal-carbamate precursor powder and 10 mL dodecylamine were added into a 20 mL reaction vial and the mixed solution was treated ultrasound (Sonic Dismembrator 500, Fisher Scientific) for 10 min at 20 kHz in ambient condition (Figure A.1). The reaction solution was centrifuged to remove the side products and obtained clear solution. Mixture solvent (chloroform:methanol = 1:3) was added into 5 mL clear solution and centrifuged to obtained purified ZAIS core in octadecene.

For formation of shell layer, zinc undecylanate and sulfur powder were dissolved in 5 mL mixture solution (octadecene:trioctylphosphine = 4:1) and added into the 20 mL reaction vial with core solution. The solution was treated ultrasound at several times with various amplitude of ultrasound. The optimum condition of power and time are 15% and 10 min. The final product was obtained centrifugation with chloroform, 1-butanol and methanol.

The ultrasound is formed from the acoustic cavitation for collapsing bubbles,

and it generates hot spots with harsh conditions ($T = 5000$ K, $P = 1800$ atm, and cooling rate = 1010 K/s). In the hot spot, raw materials were changed to the metal ion through dissociation, atomization, and ionization process. The metal ions made covalent bonds and then formed NCs [23].

The water soluble NCs were obtained by ligand exchange method. $200 \mu\text{L}$ 3-mercaptopropionic acid (MPA) was diluted in 10 mL methanol solution and its pH was controlled up over 13 using 1 M KOH. The MPA solution was added into the sample solution, and the mixture was vigorously stirred for 30 min. After the stirring, the solution with precipitate was centrifuged and washed several times with methanol. The precipitate containing MPA-coated NCs was re-dispersed in distilled water [11].

A.2.2 Quantum Yield and Fluorescence Lifetime Measurements

We use a quantum efficiency measurement system (QE-1000, Otsuka Electronics) for measuring quantum yield. Fluorescence lifetime was measured by conventional time-correlated single photon counting (TCSPC) method. 405 nm 10 MHz diode laser (LDH-P-C-405 with PDL 800-B driver, Picoquant) was used to excite the NCs. The detection of single photon and determination of its arrival time were performed using an avalanche photodiode (APD) (PFCCTC-FCAPC, MPD) and a TCSPC module (SPC-150, Becker & Hickl GmbH). ZAIS and ZAIS/ZnS NCs were dissolved in chloroform and distilled water for measurement.

A.2.3 Molar Concentration Measurements Using FCS

FCS is a technique that measures fluorescence emitted by particles diffusing through the observation volume [24, 25]. Random diffusion of the fluorophore results in time-dependent changes of intensity, called fluorescence fluctuation.

Correlation analysis of fluorescence fluctuation gives us the molecular information. ZAIS and ZAIS/ZnS NCs do not fluctuate due to blinking because there is no dark state such as triplet state unlike other QDs [11]. We used the model in which fluorescence fluctuation depends only on the diffusion. We have already discussed the autocorrelation function in Section 1.5.3.

$$G(\tau) = G(0) \left(1 + \frac{\tau}{\tau_{\text{Diff}}}\right)^{-1} \left(1 + \frac{s^2}{u^2} \frac{\tau}{\tau_{\text{Diff}}}\right)^{-1/2} \quad (\text{A.1})$$

where $G(0)$ is the amplitude at $\tau = 0$, τ_{Diff} is diffusion time in observation volume and is inversely proportional to the diffusion constant (D). s and u are the radial radius and axial half-length of observation volume. Because $G(0)$ is equal to $1/N$, the number of fluorophores (N) is calculated from $G(0)$. $G(0)$ is determined by least-squares fitting of the simulated curve with the measured data.

The concentration \bar{C} can be calculated using the relationship below.

$$\bar{C} = \frac{N}{V_{\text{eff}}} \quad (\text{A.2})$$

We can calculate the concentration if we know the exact effective volume (V_{eff}), but generally we do not know the exact value of V_{eff} . For this reason, V_{eff} should be calibrated by reference fluorophores with known concentrations and diffusion coefficient.

To measure the concentration, MPA-coated ZAIS/ZnS NCs are diluted with 0.4% triton X-100 (T8787, Sigma Aldrich) and PBS buffer to prevent self-aggregation or non-specific binding. FCS measurements are best performed when observing a small number of fluorophores (< 10), typically near 1 nM. FCS was measured with a confocal setup which is composed of objective lens (UPlanApo 60x/1.20w, Olympus), 488 nm laser (TECBL-20GC-488, World Star

Tech) to excite ZAIS/ZnS NCs, and 500 nm long pass filter to obtain the emission of ZAIS/ZnS NCs. FCS data was obtained with the correlator (Flex02-01D, Correlator.com). We needed to calibrate the setup and confirm the observation volume. Alexa488 dye solution which has known diffusion coefficient and concentration was used for calibration. The fitting process was repeated until the measured correlation function matched the calculated correlation function. The process is essential for the FCS experiment of the sample. V_{eff} and u/s are typically less than 1 fL and 15, respectively. We obtained the autocorrelation curve of ZAIS/ZnS NCs for 120 s. All measurements were repeated more than 5 times and each result was fitted independently giving the average values and the standard errors to increase the reliability.

A.2.4 Imaging of HeLa Cell and Cell Viability Assay

HeLa cell lines were cultured according to conventional methods. DMEM (LM001-05, Welgene), 10% fetal bovine serum (16000-044, Gibco), and 1% Streptomycin-penicillin (15140-122, Gibco) were used for grow media. For confocal fluorescence imaging, HeLa cell was grown in cover slip for about one day. Cell was incubated another 24 hour in 2 ml of growth media containing 10% MPA-coated ZAIS and ZAIS/ZnS NCs. Cell was fixed by 4% paraformaldehyde and mounted with prolong Gold antifade reagent (P10144, Life technologies).

Confocal laser scanning platform (SP8 X, Leica) was used for confocal imaging of HeLa cells containing MPA-coated ZAIS and ZAIS/ZnS NCs. 405 nm and 488 nm laser were illuminated through objective (HC PL APO CS2 63x/1.40 oil) and used to excite DAPI and the ZAIS and ZAIS/ZnS NCs in the fixed HeLa cells, respectively. The fluorescence of NCs were detected, ranging from 488 nm to 750 nm.

For the cell viability assay, toxic effect was evaluated with MTS (3-[4,5-

dimethylthiazol-2-yl]-5-[3-carboxymethoxyphenyl]-2-[4-sulfophenyl]-2H-tetrazolium). MTS assay measures the activity of enzymes that produce a formazan product that absorb 490 nm in live cells. Cells were seeded on 96-well plates and treated with MPA-coated ZAIS and ZAIS/ZnS NCs 0–500 nM concentration and incubated for 24 h. MTS stock solution was added and incubated for 1 h. After incubation, the absorbance at 490 nm was measured using iMark microplate absorbance reader (Picoquant). All experiments were performed in triplicate.

A.3 Results and Discussion

A.3.1 Synthesis of ZAIS and ZAIS/ZnS NCs and Their Optical Properties

ZAIS and ZAIS/ZnS NCs were synthesized according to the procedure as described in Section A.2.1. It is known that the shell layer influences on chemical and physical stability and emission intensity of NC. ZnS is a suitable material for formation of the shell layer because of its wide band gap (3.68 eV).

The TEM images of ZAIS and ZAIS/ZnS NCs are showed in Figure A.2a and b, respectively. The growth of ZnS shell leads to a large particle size. The TEM images clearly show spherical shape with an average size of 4.3 nm (ZAIS) and 5.8 nm (ZAIS/ZnS). The excitation and emission spectra of ZAIS and ZAIS/ZnS NCs are showed in Figure A.2c and d, respectively. In excitation spectra, ZAIS/ZnS shows two peaks (410 nm and 488 nm) compared to ZAIS with one peak (516 nm). The 488 nm of ZAIS/ZnS is due to the core absorption, and the 410 nm is due to the ZnS shell. The ZnS shell also leads to a blue shift of core absorption (516 nm \rightarrow 488 nm). The process of etching the core surface when the ZnS shell is formed may cause the spectral changes by the diffusion of

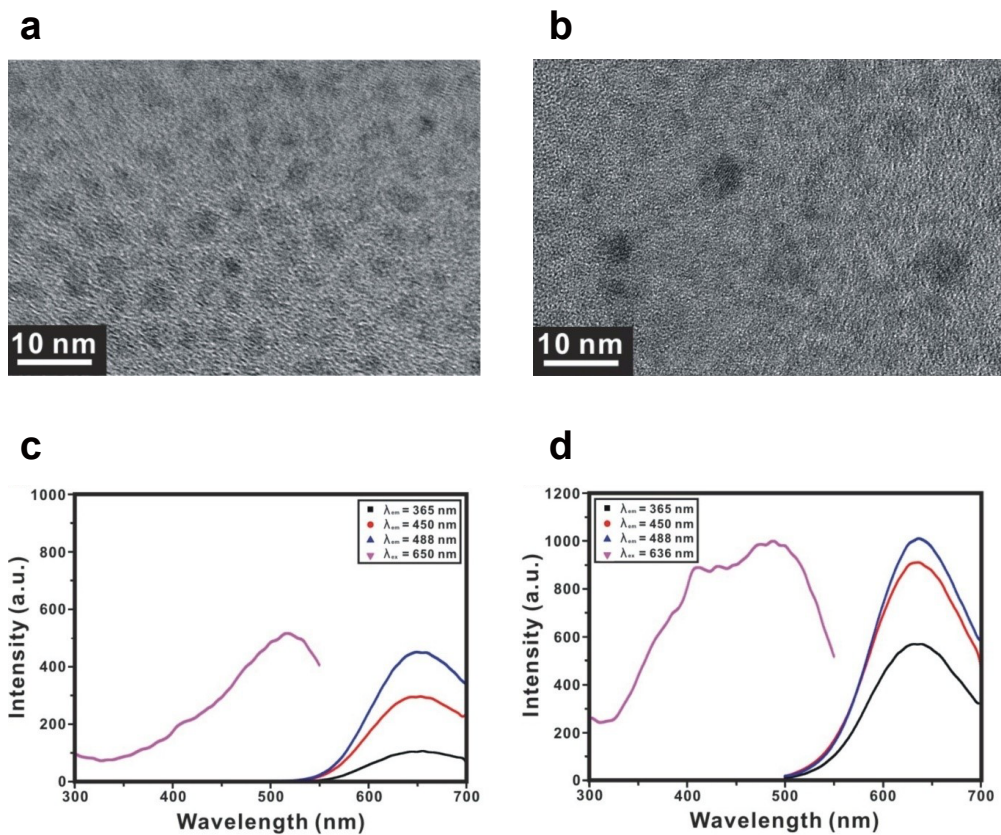


Figure A.2 TEM images of ZAIS (a) and ZAIS/ZnS (b) NCs. Diameters of ZAIS and ZAIS/ZnS are about 4.3 nm and 5.8 nm, respectively. Excitation and emission spectra of ZAIS (c) and ZAIS/ZnS (d) NCs. ZAIS/ZnS NCs show 2 times higher fluorescence intensity than ZAIS NCs at 488 nm.

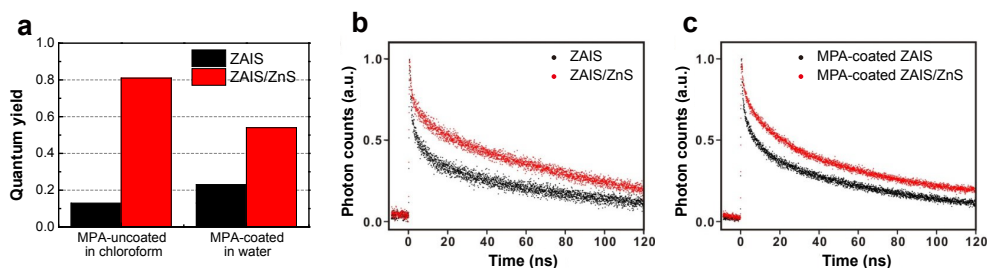


Figure A.3 Quantum yields of the NCs are show in (a). Photoluminescence decay curves of ZAIS and ZAIS/ZnS NCs in the different solvents in chloroform (b), in water (c).

zinc from the shell into the core. Both NCs show the highest emission intensity at 488 nm. This means that we do not have to use UV light inducing cell damage to excite NCs.

Quantum yields and lifetimes of ZAIS and ZAIS/ZnS NCs were measured in chloroform and water (Figure A.3). Water-soluble NCs are made by exchanging the ligand with MPA as described in Section A.2.1.

The fluorescence quantum yields of ZAIS and ZAIS/ZnS NCs are 13% and 81% in the chloroform, respectively. In water soluble NCs, the fluorescence quantum yields of ZAIS and ZAIS/ZnS NCs show 23% and 54%, respectively. The ZAIS/ZnS has 6 times higher quantum yield than ZAIS, and doubled when MPA-coating is applied (Figure A.3a). Thus, formation of ZnS shell reduced the defects on surface of NCs and increased emission intensity.

Figure A.3b and c show fluorescence lifetime curves of ZAIS and ZAIS/ZnS NCs in chloroform and water. First, ZAIS (black) has a shorter lifetime than ZAIS/ZnS (red) in both solvents. ZAIS core has many non-radiative decay paths through defects on the core surface, whereas the ZnS shell reduces some of non-radiative decay paths. Therefore, ZAIS/ZnS has a higher quantum yield and a longer lifetime than ZAIS, which means that there are fewer defects in

ZAIS/ZnS than ZAIS.

We compared uncoated and MPA-coated NCs to examine the effect of MPA-coating. It is difficult to compare uncoated and MPA-coated NCs precisely because they are in different solvent environments. MPA-coated ZAIS has 2 times higher quantum yields and longer lifetime than MPA-uncoated ZAIS. We assume that MPA acts as a kind of shell and removes the defect on the ZAIS core surface. On the other hand, when ZAIS/ZnS is coated with MPA, quantum yields and lifetime decrease compare to uncoated ZAIS/ZnS. This seems to be due to some damage during the MPA ligand exchange process of the ZnS shell.

A.3.2 Determining the Molar Concentration and Extinction Coefficient of ZAIS/ZnS NCs

We determined the molar concentration of MPA-coated ZAIS/ZnS NC solution using FCS technique. After diluting the solution of unknown concentration to 1/25, 1/50, 1/100, 1/200, autocorrelation curves from each diluted samples are obtained (Figure A.4). The concentration of each solution was calculated by fitting the curve with Equation A.1. As described in Section 1.5.3, high correlation values mean low concentration. The concentration linearly increases with dilution ratio, which means that the fitting is successful (Figure A.4b). The slope of linear fit indicates the original concentration of unknown ZAIS/ZnS solution, 6.34 μM . If the photoblinking of the NCs affects the fluorescence fluctuation, a bump appears near 1 μs . Since there is no bump in the correlation curves, NCs does not blink due to the triplet state.

The Beer-Lambert law shows the relationship between molar concentration (\overline{C}), path length (b), and absorbance (A), $A = \varepsilon \cdot b \cdot \overline{C}$. Here, ε is the wavelength-dependent molar extinction coefficient with units of $\text{M}^{-1}\text{cm}^{-1}$. This equation can be used to determine the extinction coefficient (ε) when we know the con-

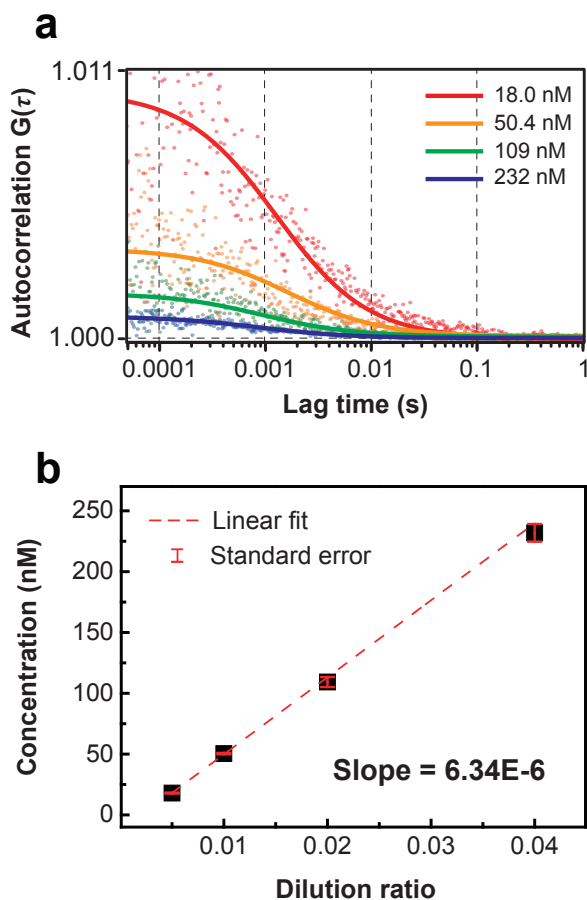


Figure A.4 Determining the molar concentration of MPA-coated ZAIS/ZnS NCs with fluorescence autocorrelation curve. (a) Fluorescence autocorrelation curve of MPA-coated ZAIS/ZnS NCs in PBS 0.4% triton X-100. Sigmoidal curve is fitted result from raw data (scattered). From top to bottom, the molar concentrations of ZAIS/ZnS were fitted as 18.0, 50.4, 109, and 232 nM each. (b) In four diluted solutions (1/25, 1/50, 1/100, 1/200), concentrations showed linear correlation with dilution ratio. One can tell the estimated concentration of original ZAIS/ZnS solution from the slope of dilution ratio–concentration graph.

centration of solution.

The absorbance of the 6.34 μM ZAIS/ZnS solution at 488 nm was measured by UV-Vis spectrometer. Substituting the absorbance and calculated concentration into the equation, we estimate the extinction coefficient of solute (ZAIS/ZnS). The calculated extinction coefficient in wavelength 488 nm ($\epsilon_{488\text{nm}}$) of ZAIS/ZnS is 238,761 $\text{M}^{-1}\text{cm}^{-1}$, which is relatively large compared to other organic dyes such as Alexa 488 ($\epsilon = 73,000$) and ATTO 488 ($\epsilon = 90,000$).

We figure out that the concentration of the MPA-coated ZAIS/ZnS solution is 6.34 μM in FCS experiments. The extinction coefficient of the ZAIS/ZnS is determined as 238,761 $\text{M}^{-1}\text{cm}^{-1}$ using the relationship between the absorbance and the concentration. The concentration of unknown ZAIS/ZnS solution can be easily measured using the extinction coefficient.

A.3.3 Application of ZAIS and ZAIS/ZnS NCs as an *in vivo* Imaging Probe

The confocal images of a HeLa cell with ZAIS and ZAIS/ZnS NCs confirm the possibility of fluorescent probes in bio-imaging. To make them water-soluble, the surface of the NCs was inevitably coated with MPA which is hydrophilic. In spite of their hydrophilic surface, NCs are well absorbed into the cells.

Figure A.5 show confocal images with MPA-coated ZAIS NCs (top line) and with MPA-coated ZAIS/ZnS NCs (bottom line). We confirmed a typical HeLa cell morphology in bright field images (Figure A.5 left column) which means that NCs does not damage the cell. The cell nucleus is stained with DAPI (blue), and fluorescence of NCs (red) are spread uniformly in the cytoplasm.

For the application of fluorescent probes, *in vitro* cytotoxicity of NCs is an important factor. Cell viability assay based on MTS is performed on HeLa cell

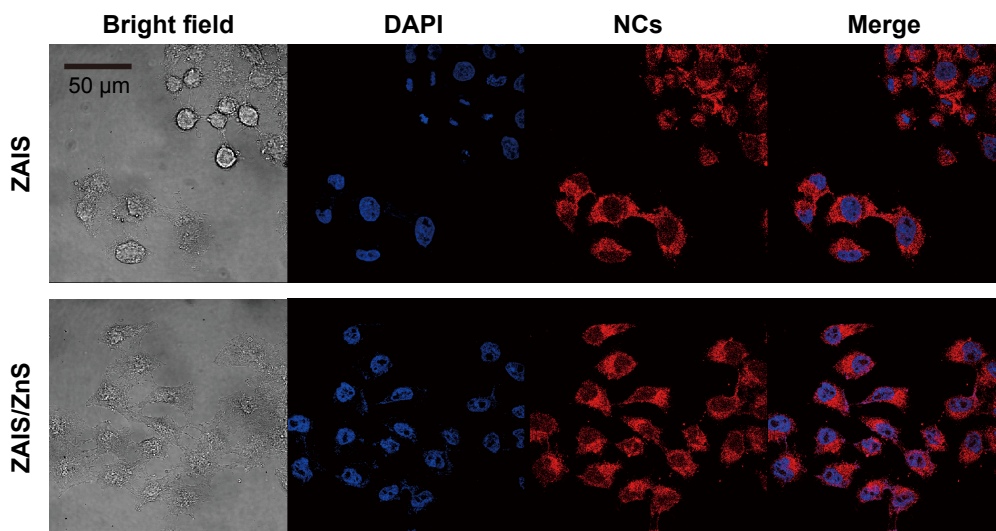


Figure A.5 Confocal images of HeLa cells incubated with ZAIS (top line) and ZAIS/ZnS NCs (bottom line). NCs enter into the cytoplasm well.

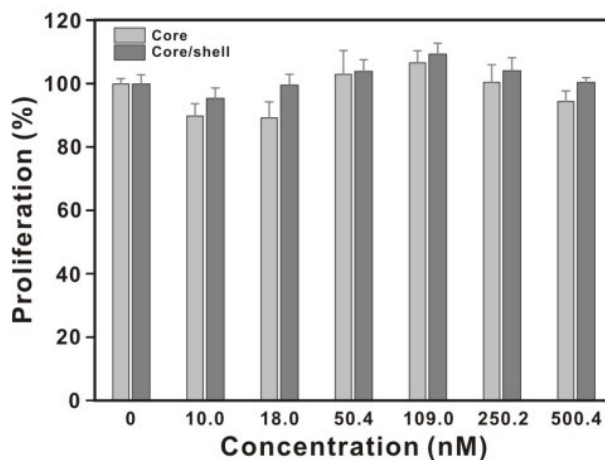


Figure A.6 MTS cell viability assay was performed to check the cell viability and cytotoxicity of ZAIS and ZAIS/ZnS NCs. Concentrations of up to 500 nM do not affect cell viability. The error bars are mean standard deviations.

line (Figure A.6). We test various molar concentrations (ranging from 0 to 500 nM) as measured by FCS method. The toxicity of the ZAIS and ZAIS/ZnS NCs is not found on HeLa cell after 24 h incubation.

A.4 Conclusion

We synthesized ZAIS and ZAIS/ZnS NCs containing less-toxic elements (Zn, Ag, In, and S) by ultrasonic irradiation that is a simple and rapid synthesizing method. The ZnS shell with high bandgap is added to ZAIS core to make the fluorescence brighter. ZAIS/ZnS has higher quantum yield and longer lifetime than ZAIS. This is because the ZnS layer effectively removes defects on the core surface and reduces non-radiative decay paths. For use as a bio-imaging probe, water soluble NCs are fabricated by ligand exchange. The MPA-coated ZAIS core has higher quantum yield and longer lifetime than uncoated ZAIS, because MPA has a kind of shell effect. On the other hand, MPA-coated ZAIS/ZnS has smaller quantum yield and shorter lifetime than uncoated ZAIS/ZnS. MPA has a contrary effect on the two types of NCs.

The molar concentration of MPA-coated ZAIS/ZnS solution is measured by FCS technique. Using the molar concentration and absorbance, we determine that the molar extinction coefficient ($\epsilon_{488\text{nm}}$) of ZAIS/ZnS is $238,761 \text{ M}^{-1}\text{cm}^{-1}$. Once extinction coefficient is known, the concentration can be easily calculated from absorbance measurements.

To investigate the possibility of NCs as a cell imaging probe, we incubated HeLa cells in cell culture medium containing MPA-coated ZAIS and ZAIS/ZnS NCs. The confocal images show that water soluble NCs are well absorbed into the cytoplasm of HeLa cells in spite of their hydrophilicity. In MTS assay, NCs are rarely toxic to HeLa cell when cells are treated with 500 nM NCs for 24 h.

The newly synthesized ZAIS and ZAIS/ZnS NCs have high quantum yields and high extinction coefficients as well as very low cytotoxicity, demonstrating their potential for using in cell imaging and other biological applications. We measured the concentration and extinction coefficients of the fluorescent NCs that could increase the utilization of NCs.

Appendix B

Generation of Highly Luminescent Micro Rings by Optical Irradiation

This chapter was published in *Chem. Comm.*, 2017, **53**, 7642

B.1 Introduction

As a fundamental element of nature, light performs essential roles in energy production [26], visual perception [27], and signal transduction [28] and so on. The material-specific nature of the light-matter interaction has been widely used to characterize unknown materials [29], while the ubiquity and versatility of such interaction has even allowed unexpected applications such as animal motion control by light [30], light-induced nano motors [31], and photothermal therapy for cancer treatment [32].

Sometimes the light-matter interaction is used to generate a certain structure of materials on the microscopic scale. A prime example is found in photolithography for semiconductor devices [33,34], where the light-induced change

of solubility is used to control the device structure. Another example may include the light-induced manipulation of azo-polymer films utilizing photoinduced molecular migration and surface deformation [35–37], although its actual use has been restricted to holographic surface relief gratings [38].

In our experiment, we reported another light-induced process that results in a highly luminescent, ring-shaped microstructure (named the “luminescent micro ring”, LMR) on a glass surface. There have been reported cases analogous to our finding in terms of the resultant ring-like structure, including the agglomeration of metal nanoparticles [39] and the aforementioned azo-polymer films, but our LMR has unique photophysical and mechanical properties distinctly different from those of the previously reported cases.

B.2 Materials and Methods

B.2.1 Sample Preparation

Since almost all of experiments were performed on the optical microscope, the sample was basically prepared on the microscope cover glass (0101242, Marienfeld). We used plastic coverslips (12547, Fisher Scientific) as a different substrate. Depending on the type of light absorbing molecules, we prepared each sample in the following conditions.

1. Liquid samples containing dye molecules

We made 2 mM aqueous solutions of fluorescein (F6377, Sigma Aldrich), rhodamine 6G (R6G, 83697, Sigma Aldrich) and methylene blue (M9140, Sigma Aldrich). To test the importance of absorbance of samples, we prepared 50 mM solution of phenolphthalein (PhP, 015945, Sigma Aldrich) in EtOH (A995-4, Fisher Scientific) and used 1 M aqueous solution of NaOH (7571-4400, Daejung

Chemicals & Metals) to make the basic PhP sample (PhP in EtOH : NaOH(aq) = 98 : 2, volume ratio). Effect of sample's charges/ions were tested by using [2 mM R6G + 20 mM NaCl] aqueous solution and 2 mM Nile Red (N0659, TCI) solution in methoxybenzene (A0492, TCI). A 2 mM Atto540Q (AD540Q-21, Atto-tec) solution in acetonitrile (9017-03, J.T.Baker) was used as a nonfluorescent but highly absorbing sample. In order to remove aggregated particles and impurities, the samples were mildly sonicated for more than 60 minutes and filtered by a syringe filter with a 20-nm pore size (6809-1102, Whatman GmbH). A small volume ($\sim 20 \mu\text{L}$) of sample was dropped onto the cover glass for further experiments.

2. Surface-Bound Nanoparticles

We tested three kinds of nanoparticles: 30, 35, 50, 100 and 140 nm fluorescent nanodiamonds (FND) from the Dr. Huan-Cheng Chang group of Taiwan, 80 nm gold colloid (EM.GC80, BBI Solutions), and CdSe/ZnS quantum dot (Q21321MP, Invitrogen). All nanoparticles were immobilized on the surface of the cover glass through the electrostatic interaction, resulted from treatment of the cover glass with poly-L-lysine solution (P8920, Sigma Aldrich) for 3 minutes to coat the surface with positive charges. After washing out the poly-L-lysine with deionized water, the aqueous solutions of nanoparticles were incubated on the surface for 3 minutes to induce electrostatic binding to the surface. The unbound nanoparticles were washed out with deionized water, and finally a proper mounting medium was applied on the cover glass.

3. Transparent Polymer Matrices

PDMS elastomer (SYLGARD 184, Dow Corning) and PMMA (MW 15,000 and 350,000, Sigma Aldrich) were used as model systems for transparent polymer

matrices. PDMS was coated on the glass surface following the protocol provided by the company. PMMA was dissolved in a chloroform solvent and the solution was drop-casted on the glass surface. The glass coverslip was then baked in an oven at 80 °C for 30 minutes to remove the solvent and obtain the glass surface coated with PMMA.

4. Dye Powder

In our fluorescence lifetime measurement of R6G powder for comparison with those of R6G solution and the LMR, the sample powder was dropped on the glass surface and used without further treatment.

When we characterized the LMR, the mounting media was removed by vigorous washing of the glass coverslip with acetone, methanol, and deionized Milli-Q water. The LMR strongly adhered to the glass surface, even sonication in various solvents cannot remove it from glass coverslips. All images and spectra in Figure B.2 were obtained without any mounting medium. If long-term generation and observation of the LMR was necessary in the liquid medium, we used a cover glass bottom dish (100350, SPL Life Sciences) as a sample container to reduce the effect of solvent evaporation. In particular, when we tested benzene and other aromatic hydrocarbons, we used a homemade sample container made of stainless steel to avoid unintended generation of organic impurities resulting from dissolution of container materials into the solvent.

B.2.2 Optical Microscopy and Spectroscopy

All optical experiments were performed using a home-built microscope (Figure B.1). Two laser beams (532 nm: Samba™ 532, Cobolt; 633 nm: 25-LHP-928-230, CVI Melles-Griot) were combined into a single optical path with dichroic mirrors (ZT532rdc, Chroma), and coupled to a single-mode fiber ($\Phi = 4.2 \mu\text{m}$,

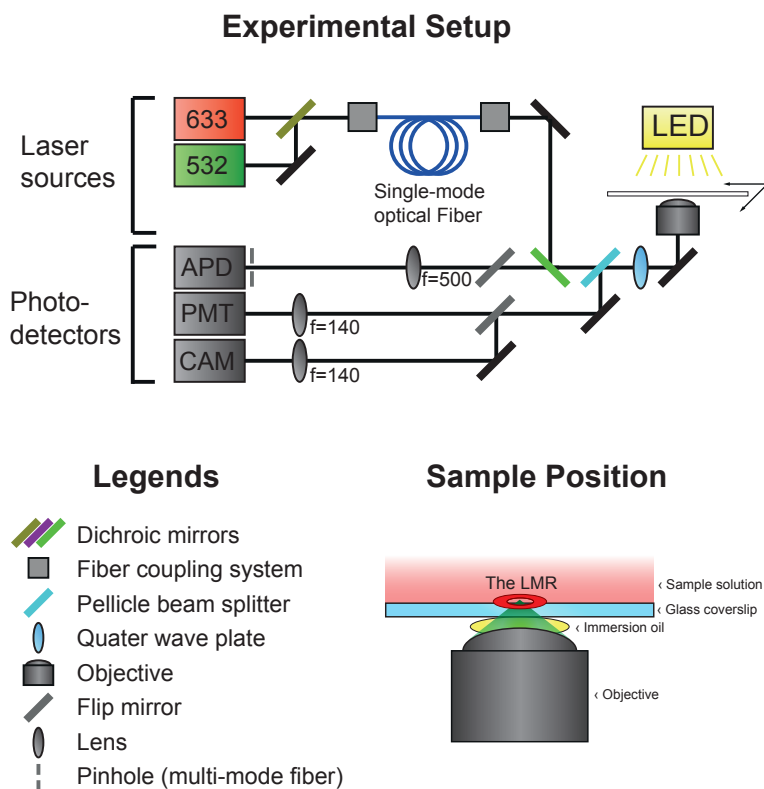


Figure B.1 Schematic design for the home-built optical microscope. A white light LED and three lasers were used as the light source for optical imaging. A quarter waveplate made the excitation light circularly polarized. The sample was placed on a piezo stage for precise control of scanning. In order to avoid severe signal loss, a pellicle beam splitter was introduced to split the scattered light to another beam path that cannot pass through the dichroic mirror. A WebCam has strong resistance against photo-damage. Scanning-based luminescence and scattering images were obtained by the APD and PMT.

P1-630PM-FC, Thorlabs) to make Gaussian-like beams. They passed through a second dichroic mirror (ZT375/488/532/633rpc, Chroma) which removed scattered light from luminescence signals. An achromatic $\lambda/4$ retarder (RAC-3.4.15, Bernhard Halle Nachfl.) was employed to make the circularly polarized excitation light for efficient excitation of the sample. An oil-immersion objective lens (UIS2 series, PlanApo N, NA = 1.4, 100x, Olympus) effectively focuses the excitation light and collect the transmitted, scattered and luminescence signals. The sample was placed on a piezo stage (Nanomax Max311, Thorlabs) that can precisely scan the sample for scanning-based luminescence/scattering imaging. A common white light LED placed above the sample stage was also used as an illumination light source for bright-field imaging.

A removable pellicle beam splitter (BP145B1, Thorlabs) was introduced for the bright-field and scattering images to avoid severe signal loss due to the dichroic mirrors, whereas the luminescence signals were collected after passing the dichroic mirrors without the pellicle beam splitter. Three photodetectors, which were selectable by using flip mirrors, were employed to acquire the signals: an avalanche photodiode (APD, SPCM-AQR-14FC, Perkin Elmer) coupled to a multi-mode fiber $\Phi = 62.5 \mu\text{m}$, M31L02, Thorlabs) acts as a pinhole in the confocal luminescence imaging mode; A photomultiplier tube (MP962, Perkin Elmer) with active quenching control collects scattered signals without the pinhole to generate scattering images; a WebCam (VX1000, Microsoft) with a relatively low detection quantum yield records signals when extremely large photon counts are expected as in the case of taking a movie for the LMR formation. The detection lenses that effectively focus optical signals to the detectors were selected by considering the size of the confocal pinhole or wide-field image magnification. If an emission filter was needed to separate the signals from backgrounds, a proper filter was placed in front of each detector (Table

1). The acquired signals were analyzed by a multi-channel scaler (P7882, Fast ComTech) or a data acquisition board provided by the supplier and then processed by the imaging software also provided by the supplier, except when the Inspector program was used for scanning-based imaging.

	Luminescence	Transmission	Scattering	Spectrum	Lifetime
Light Source	CW 532 nm	White light LED	CW 532 nm	CW 532 nm	Femtosecond Ti:sapphire
Emission Filter	LP03-532RE-25	-	ET525/50m	LP03-532RE-25	LP03-532RE-25

Table 1 Light sources and emission filters used in each experiment. In particular, we changed the dichroic mirror that reflects the excitation light and transmits the luminescence (ZT375/488/532/633rpc \rightarrow ZT532rdc, not shown in table) to prevent the spectral deformation due to the dichroic mirror while getting photoluminescence spectrum of the LMR.

In order to characterize the emission spectra from dye solutions, solid powders and the LMR, a portable spectrometer (SM240, Spectral Products) replaced the APD (Table 1). For the lifetime analysis, light from a femtosecond laser (MaiTai, Spectra-physics) with supercontinuum generator (FemtoWHITE-800, NKT Photonics) and appropriate bandpass filter excited the sample (Table 1), and a time-correlated single photon counter (SPC-150, Becker & Hickl GmbH) analyzed the collected photons to generate luminescence decay profiles. The height/phase imaging of the LMR was performed using a commercially available atomic force microscope system (NanoWizard, JPK Instruments).

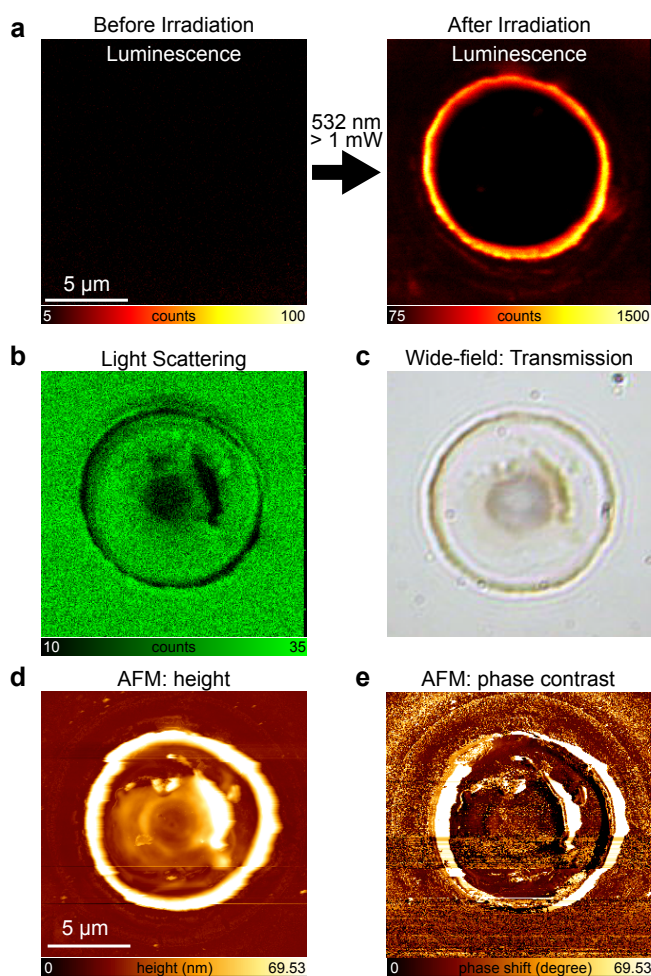


Figure B.2 Images of luminescent micro ring (LMR). (a) Confocal luminescence images for the generation of luminescent micro ring (LMR) under intense CW laser irradiation. When a glass surface coated with an aqueous solution of 2 mM R6G (left) is irradiated, a bright image of LMR appears around the irradiation centre (right). (b) Light-scattering image of the same LMR. (c) Wide-field transmission image of the same LMR. The LMR showed poor efficiency for transmission as well as scattering. The length scale of the wide-field transmission image did not exactly follow the scale bar, but was roughly adjusted. (d) Surface morphology scan by AFM shows that the LMR has a thickness of ≈ 100 nm. Some high-thickness structures are also observed inside the LMR but they are not luminescent. (e) The lock-in phase shift of these microstructures was larger than that of the glass surface, suggesting that the LMR is composed of softer materials than the glass.

B.3 Results and Discussion

B.3.1 LMR Phenomenon

When an intense CW laser (532 nm, 41 mW) beam was focused on a glass surface coated with an aqueous solution of Rhodamine 6G (R6G), we discovered that an LMR was unexpectedly formed on the glass surface (Figure B.2a). To see how this process takes place, we recorded its temporal evolution using a WebCam and found that the LMR was generated following a dynamic, explosion-like event. In order to characterize the physical properties of the LMR, we obtained its light scattering and transmission images by optical microscopy and surface morphology and phase contrast images by atomic force microscopy (AFM) (Figure B.2b-e). Although a surface morphology scan by AFM showed that both the ring and certain internal regions of the ring had protrusions (with a height of ~ 170 nm, Figure B.2d), it was only the circular ring that was luminescent (Figure B.2a). A phase contrast image taken using an AFM showed a larger lock-in phase shift at these microstructures, indicating its softer material nature than the glass surface (Figure B.2e) [40].

As for the photophysical properties, the LMR has a much broader luminescence spectrum, ranging from mid-visible to even near-IR (Figure B.3a), than the R6G solution [41]. The luminescence lifetime of the LMR measured by time-correlated single photon counting (TCSPC) was much shorter (~ 0.3 ns) than that of the R6G solution (3.5 ns) [42] (Figure B.3b). We found that the most striking photophysical property of the LMR was its great resistance against photobleaching (Figure B.3c). Under continuous raster-scanning with 532 nm laser irradiation at an optical power of 10 mW, the LMR showed little photobleaching for up to ~ 130 min, except for a slight decrease in luminescence intensity.

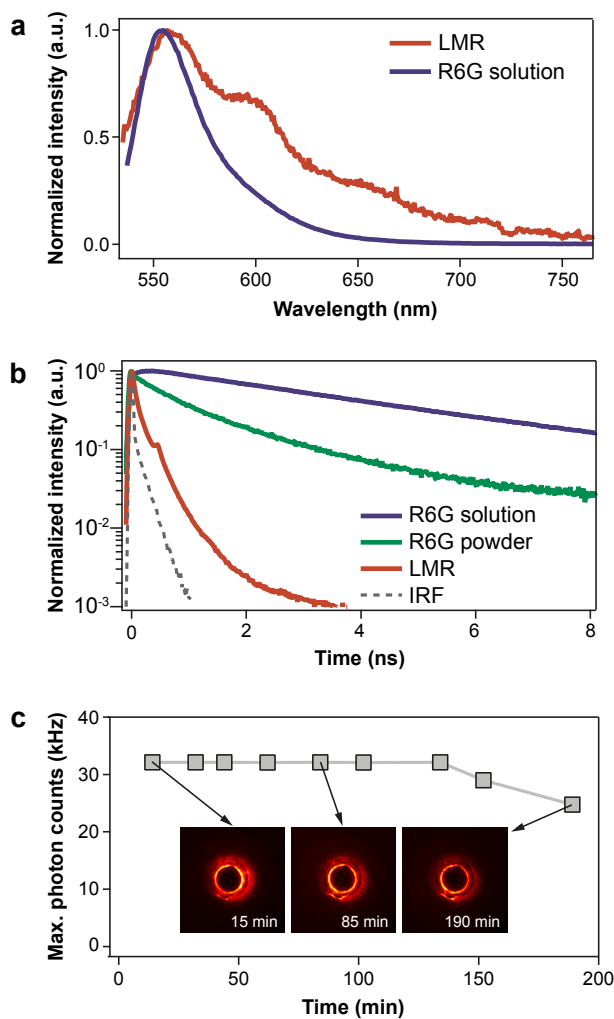


Figure B.3 Photophysical properties of LMR (a) Photoluminescence spectrum of the LMR in Figure B.2 and that of R6G in aqueous solution. (b) Temporal decay profiles of luminescence for R6G solution, R6G powder, and the LMR. (c) Resistance of the LMR against photobleaching during continuous irradiation of light. The bright luminescence from the LMR was sustained for more than 3 hours with a sufficient signal-to-background ratio for imaging.

B.3.2 Characterization of the LMR

The characteristic emission spectrum and lifetime of the LMR give clues to its identity. In a previous study, a thin film of R6G with luminescence peaks at 617 and 660 nm was attributed to various aggregates of R6G molecules in the film [43]. Another study showed that a high concentration of R6G in xerogel nanolayers gave rise to a large bathochromic shift in its photoluminescence spectrum, which was suggested to be caused by fluorescent J-aggregates [44]. On the other hand, the luminescence lifetime of the R6G aggregates intercalated into Laponite clay films was much shorter than that of the monomer [45]. Our own data in Figure B.3b shows that the solid powder of R6G has a faster TCSPC decay than its solution, as the former may contain some aggregates, unlike the latter. If indeed our LMR consists of various aggregates of R6G molecules, it would be consistent with the broader luminescence spectrum and the decrease in the TCSPC lifetime.

As a first step to characterize the light-induced formation of the LMR, we tested several light-absorbing molecules and mounting media to generate the LMR in addition to R6G in water (Table 2). It is clear that large absorbance at the irradiation wavelength is a key factor for the LMR formation. In particular, phenolphthalein (PhP), whose absorbance changes significantly as the pH of its solution is changed [46], was introduced as a light absorber to investigate whether light absorption plays a crucial role in the LMR formation. It turned out that LMR formation was possible only when the solution was basic and thus PhP could efficiently absorb the 532 nm light. LMR formation was also achieved with nearly transparent immersion oils when light-absorbing nanoparticles such as fluorescent nanodiamonds were present on the glass surface.

Light-absorbing Molecule	Mounting Medium	LMR Formation
-		X
Fluorescein	Water	O
Rhodamine 6G		O
Methylene Blue		O
Rhodamine 6G		Water (on a plastic coverslip)
	Water (20 mM NaCl)	O
Nile Red	Methoxybenzene	O
Atto540Q	Acetonitrile	O
Phenolphthalein	Ethanol (neutral) ¹	X
	Ethanol (basic) ¹	O
-	Immersion oils ³	X
Nanoparticles ²		O
-	Polymer matrices ⁴	X
-	Hydrocarbons ⁵	X

Table 2 ¹Neutral (basic) ethanol is a 98:2 (volume ratio) mixture of ethanol +H₂O (1 M NaOH (aq)). ²Fluorescent nanodiamonds (30, 35, 50, 100, 140 nm in diameter), 80 nm Au beads, or 10 nm CdSe/ZnS quantum dots. ³Immersion oils manufactured by Olympus, Leica, and Merck. ⁴PDMS and PMMA. ⁵Cyclohexane, octane, benzene, naphthalene, anthracene, pyrene, and perylene (aromatic hydrocarbons were dissolved in benzene).

We also tested the possible effect of electrostatic charge in the form of ions in the sample. We found that neither complete absence of charge (as with 2 mM Nile Red in methoxybenzene) nor abundance of charge (as with 20 mM NaCl added to 2 mM R6G in water) made any difference as long as the solution contained light-absorbing molecules. Transparent polymer matrices alone yielded no LMR, as did benzene derivatives whose absorption coefficient at the irradiation laser wavelength (532 or 633 nm in this experiment) was effectively zero. Therefore, we conclude that intense light absorption by matter in the form of either solute molecules or nanoparticles in solution is a prerequisite for the LMR formation. Incidentally, Table 2 shows that we could not generate the LMR eas-

ily on a plastic coverslip, possibly because of its lower transparency to visible light (for absorption) or different surface properties (for material adhesion).

Next, we measured the diameter of the LMR as we varied the concentration of R6G, the power of irradiation laser, and the duration of laser irradiation (Figure B.4). Results indicated a general saturation behaviour, suggesting that a steady-state is reached during the formation of the LMR. We propose that a key step in the LMR formation should involve a heat-induced process following light absorption, since the convection in solution allows its temperature near the glass surface to reach its steady-state value when the laser power is sufficiently high or when the duration time is sufficiently long [47].

If the heat is caused by light absorption, the temperature will also reach a plateau when the absorber concentration is high enough to allow nearly all incident light energy to be absorbed regardless of the concentration. In addition, a simple simulation showed that the temperature of the glass-solution interface could reach thousands of Kelvin (Figure B.5) [48], which is high enough to change materials properties through thermal reactions or phase transition. Indeed, we could generate highly luminescent micro rings even with the highly-absorbing but virtually non-fluorescent quencher dye Atto540Q (Figure B.6), which suggests that materials properties of the LMR can grossly change from its source material as complex photothermal reactions take place. Likewise, LMRs made from nanoparticle absorbers in immersion oil showed significantly different photoluminescence decay behaviour from its source material (Figure B.7). Therefore, we suggest that the generation of the LMR may be induced by a light-induced photothermal process and may involve complex reactions, based on the absorption dependent propensity for LMR formation (Table 2), the saturation of the LMR diameter (Figure B.4), distinct photophysical properties from those of source materials (Figure B.5, B.6), and our simulation result

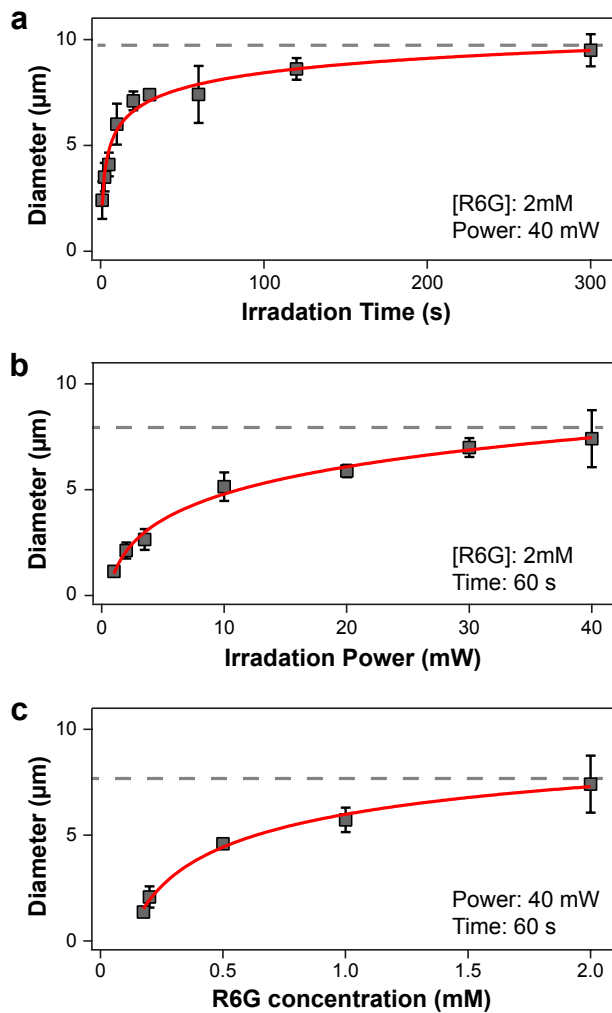


Figure B.4 Control the diameter of the LMR as a function of (a) irradiation time, (b) irradiation power, and (c) the concentration of absorbing molecule (R6G). Red lines are guides for the eye, not fitted lines. The grey dashed-lines indicate possible saturation values.

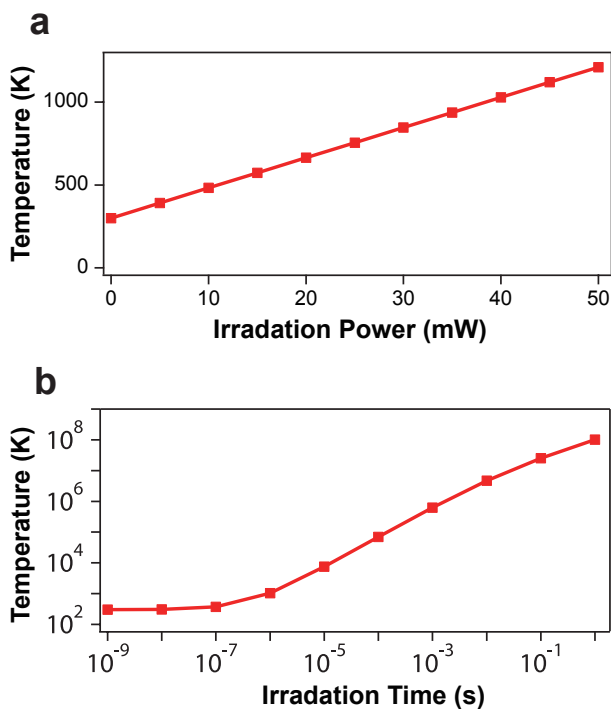


Figure B.5 Simulated temperature at the interface between the glass coverslip and the light-absorbing medium (a 2 mM aqueous solution of R6G) as a function of (a) the irradiation power (at 1 μ s) and (b) the irradiation time (at 40 mW) [48]. Irradiation beam size for the simulation is 600 nm in diameter, typical value in confocal microscope with high-NA objective lens. Convection, radiation, and phase transitions were neglected in this simulation. Without these heat transport processes that lower the interfacial temperature, it reaches a sufficiently high temperature after $\sim 1 \mu$ s (when using 40 mW of laser power) to evaporate water-based media and to initiate thermal reactions. In reality, interfacial cooling will happen quite efficiently but nevertheless, a local region with a sufficiently high temperature may still be present for the above processes.

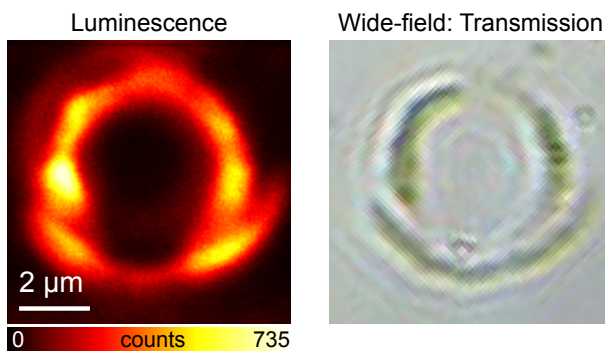


Figure B.6 Comparison of the confocal luminescence image (Left) and wide-field transmission image (Right) of the LMR generated with 2 mM Atto540Q solution in acetonitrile. The LMR showed bright luminescence despite the very low fluorescence quantum yield of the quencher dye Atto540Q. The length scale of the wide-field transmission image does not exactly follow the scale bar but is roughly adjusted.

(Figure B.5).

B.4 Conclusion

In conclusion, we serendipitously discovered light-induced formation of a microstructure hitherto unknown and characterized the photophysical properties of the resultant LMR. The generation of the LMR takes place only when the laser is highly focused near the interface between glass coverslip and solution containing a sufficient amount of light-absorbing materials. From the photoluminescence spectra and the TCSPC lifetimes, it is assumed that the LMR consists largely of materials other than the original sample, which may include its complex aggregates. We also found that the generation of the LMR may well be induced by a light-induced photothermal process. The uniquely appealing properties of the LMR include: i) highly bright luminescence and robust photostability ii) ease of generation at any intended location, and iii) strong

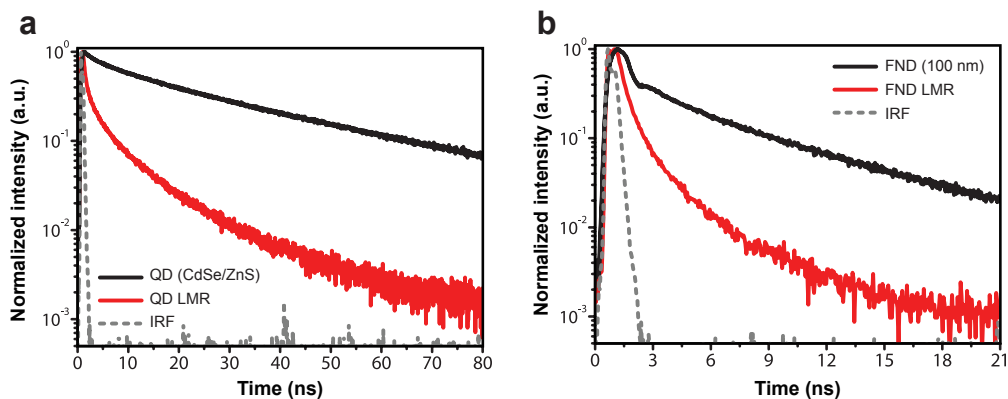


Figure B.7 Comparison of the TCSPC photoluminescence lifetimes of nanoparticle absorbers QD and FND vs. those of the LMRs generated from them in immersion oil (manufactured by Olympus, containing 1,3,5-triisopropylbenzene as a major component). In both cases, the LMR exhibits a much shorter lifetime and more complex decay profile, which suggests that the LMR may contain complex materials resulting from diverse photothermal processes.

adhesion to glass surface. With these desirable properties, the LMR can be used as a fiducial marker for drift-corrected long-term imaging [49] as well as in many other applications. Since the exact composition of the LMR and the mechanism of LMR formation are still unclear, further study is needed and now underway.

Bibliography

- [1] Philip Jackson, Dimitrios Hariskos, Erwin Lotter, Stefan Paetel, Roland Wuerz, Richard Menner, Wiltraud Wischmann, and Michael Powalla. New world record efficiency for Cu(In,Ga)Se₂ thin-film solar cells beyond 20%. *Progress in Photovoltaics: Research and Applications*, 19(7):894–897, 2011.
- [2] Tatsuya Kameyama, Takuya Takahashi, Takahiro Machida, Yutaro Kamiya, Takahisa Yamamoto, Susumu Kuwabata, and Tsukasa Torimoto. Controlling the electronic energy structure of ZnS–AgInS₂ solid solution nanocrystals for photoluminescence and photocatalytic hydrogen evolution. *The Journal of Physical Chemistry C*, 119(44):24740–24749, 2015.
- [3] Maureen A. Walling, Jennifer A. Novak, and Jason R. E. Shepard. Quantum dots for live cell and *in vivo* imaging. *International Journal of Molecular Sciences*, 10(2):441–491, 2009.
- [4] Ron Hardman. A toxicologic review of quantum dots: toxicity depends on physicochemical and environmental factors. *Environmental Health Perspectives*, 114(2):165–172, 2006.
- [5] Sung Pyo Hong, Hoo Keun Park, Ji Hye Oh, Heesun Yang, and Young Rag Do. Comparisons of the structural and optical properties of o-AgInS₂, t-AgInS₂, and c-AgIn₅S₈ nanocrystals and their solid-solution nanocrystals with ZnS. *Journal of Materials Chemistry*, 22(36):18939–18949, 2012.
- [6] Haizheng Zhong, Zelong Bai, and Bingsuo Zou. Tuning the luminescence properties of colloidal I–III–VI semiconductor nanocrystals for optoelectronics and biotechnology applications. *The Journal of Physical Chemistry Letters*, 3(21):3167–3175, 2012.

- [7] Evren Mutlugun, Pedro Ludwig Hernandez-Martinez, Cuneyt Eroglu, Yasemin Coskun, Talha Erdem, Vijay K. Sharma, Emre Unal, Subhendu K. Panda, Stephen G. Hickey, Nikolai Gaponik, *et al.* Large-area (over $50 \text{ cm} \times 50 \text{ cm}$) freestanding films of colloidal InP/ZnS quantum dots. *Nano Letters*, 12(8):3986–3993, 2012.
- [8] Kyungnam Kim, Sohee Jeong, Ju Yeon Woo, and Chang-Soo Han. Successive and large-scale synthesis of InP/ZnS quantum dots in a hybrid reactor and their application to white LEDs. *Nanotechnology*, 23(6):065602–065607, 2012.
- [9] Woo-Seuk Song, Jong-Hoon Kim, Jeong-Hoon Lee, Hye-Seung Lee, Young Rag Do, and Heesun Yang. Synthesis of color-tunable Cu–In–Ga–S solid solution quantum dots with high quantum yields for application to white light-emitting diodes. *Journal of Materials Chemistry*, 22(41):21901–21908, 2012.
- [10] Thomas Pons, Emilie Pic, Nicolas Lequeux, Elsa Cassette, Lina Bezdetsnaya, François Guillemin, Frédéric Marchal, and Benoit Dubertret. Cadmium-free CuInS₂/ZnS quantum dots for sentinel lymph node imaging with reduced toxicity. *ACS Nano*, 4(5):2531–2538, 2010.
- [11] Seung Jae Lee, Younggyu Kim, Jongjin Jung, Mi Ae Kim, Namdoo Kim, Seong Jin Lee, Seong Keun Kim, Yong-Rok Kim, and Joung Kyu Park. Rapid and facile synthesis of a (Zn_xAg_yIn_z)S₂ nanocrystal library via sono-combichem method and its characterization including single nanocrystal analysis. *Journal of Materials Chemistry*, 22(24):11957–11963, 2012.
- [12] S. Kumar, J. Aaron, and K. Sokolov. Directional conjugation of antibodies to nanoparticles for synthesis of multiplexed optical contrast agents with both delivery and targeting moieties. *Nature Protocols*, 3(2):314–320, 2008.
- [13] W. William Yu, Lianhua Qu, Wenzhuo Guo, and Xiaogang Peng. Experimental determination of the extinction coefficient of CdTe, CdSe, and CdS nanocrystals. *Chemistry of Materials*, 15(14):2854–2860, 2003.
- [14] Toshihiro Kuzuya, Yutaka Tai, Saeki Yamamuro, and Kenji Sumiyama. Size-focusing of ZnS nanocrystals observed by MALDI–TOF mass spectroscopy. *Chemical Physics Letters*, 407(4):460–463, 2005.
- [15] Elke Haustein and Petra Schwillle. Fluorescence correlation spectroscopy: novel variations of an established technique. *Annual Review of Biophysics and Biomolecular Structure*, 36:151–169, 2007.
- [16] Petra Schwillle. Fluorescence correlation spectroscopy and its potential for intracellular applications. *Cell Biochemistry and Biophysics*, 34(3):383–408, Jun 2001.

- [17] Sören Doose, James M. Tsay, Fabien Pinaud, and Shimon Weiss. Comparison of photophysical and colloidal properties of biocompatible semiconductor nanocrystals using fluorescence correlation spectroscopy. *Analytical Chemistry*, 77(7):2235–2242, 2005.
- [18] R. A. Sperling, T. Liedl, S. Duhr, Stefan Kuderka, M. Zanella, C.-A.J. Lin, W. H. Chang, D. Braun, and W. J. Parak. Size determination of (bio) conjugated water-soluble colloidal nanoparticles: a comparison of different techniques. *The Journal of Physical Chemistry C*, 111(31):11552–11559, 2007.
- [19] Pudun Zhang, Liang Li, Chaoqing Dong, Huifeng Qian, and Jicun Ren. Sizes of water-soluble luminescent quantum dots measured by fluorescence correlation spectroscopy. *Analytica Chimica Acta*, 546(1):46–51, 2005.
- [20] Chaoqing Dong, Rui Bi, Huifeng Qian, Liang Li, and Jicun Ren. Coupling fluorescence correlation spectroscopy with microchip electrophoresis to determine the effective surface charge of water-soluble quantum dots. *Small*, 2(4):534–538, 2006.
- [21] Jennifer A. Rochira, Manasa V. Gudheti, Travis J. Gould, Ryan R. Laughlin, Jay L. Nadeau, and Samuel T. Hess. Fluorescence intermittency limits brightness in CdSe/ZnS nanoparticles quantified by fluorescence correlation spectroscopy. *The Journal of Physical Chemistry C*, 111(4):1695–1708, 2007.
- [22] Chaoqing Dong and Jicun Ren. Measurements for molar extinction coefficients of aqueous quantum dots. *Analyst*, 135(6):1395–1399, 2010.
- [23] Kenneth S. Suslick. Sonochemistry. *Science*, 247(4949):1439–1446, 1990.
- [24] Nancy L. Thompson. *Fluorescence correlation spectroscopy*. Springer, 2002.
- [25] Joseph R. Lakowicz. *Principles of fluorescence spectroscopy*. 2006.
- [26] Bhubaneswari Parida, S. Iniyan, and Ranko Goic. A review of solar photovoltaic technologies. *Renewable and Sustainable Energy Reviews*, 15(3):1625–1636, 2011.
- [27] Krzysztof Palczewski. G protein-coupled receptor rhodopsin. *Annual Review of Biochemistry*, 75:743–767, 2006.
- [28] Meng Chen, Joanne Chory, and Christian Fankhauser. Light signal transduction in higher plants. *Annual Review Genetics*, 38:87–117, 2004.
- [29] Wolfgang Demtröder. *Laser spectroscopy*, volume 1. Springer, 2008.
- [30] Lief Fenno, Ofer Yizhar, and Karl Deisseroth. The development and application of optogenetics. *Annual Review of Neuroscience*, 34, 2011.

- [31] Wesley R. Browne and Ben L. Feringa. Making molecular machines work. *Nature Nanotechnology*, 1(1):25–35, 2006.
- [32] D. Jaque, L. Martinez Maestro, B. Del Rosal, P. Haro-Gonzalez, A. Benayas, J. L. Plaza, E. Martin Rodriguez, and J. Garcia Sole. Nanoparticles for photothermal therapies. *Nanoscale*, 6(16):9494–9530, 2014.
- [33] D. Mijatovic, J. C. T. Eijkel, and A. Van Den Berg. Technologies for nanofluidic systems: top-down vs. bottom-up—a review. *Lab on a Chip*, 5(5):492–500, 2005.
- [34] Aránzazu del Campo and Christian Greiner. Su-8: a photoresist for high-aspect-ratio and 3D submicron lithography. *Journal of Micromechanics and Microengineering*, 17(6):R81, 2007.
- [35] S. Bian, L. Li, J. Kumar, D. Y. Kim, J. Williams, and S. K. Tripathy. Single laser beam-induced surface deformation on azobenzene polymer films. *Applied Physics Letters*, 73(13):1817–1819, 1998.
- [36] Shaoping Bian, John M. Williams, Dong Yu Kim, Lian Li, Srinivasan Balasubramanian, Jayant Kumar, and Sukant Tripathy. Photoinduced surface deformations on azobenzene polymer films. *Journal of Applied Physics*, 86(8):4498–4508, 1999.
- [37] Antonio Ambrosio, Lorenzo Marrucci, Fabio Borbone, Antonio Roviello, and Pasqualino Maddalena. Light-induced spiral mass transport in azo-polymer films under vortex-beam illumination. *Nature Communications*, 3:989, 2012.
- [38] Seungwoo Lee, Hong Suk Kang, and Jung-Ki Park. Directional photofluidization lithography: micro/nanostructural evolution by photofluidic motions of azobenzene materials. *Advanced Materials*, 24(16):2069–2103, 2012.
- [39] Yi Zhang, Claire Gu, Adam M. Schwartzberg, Shaowei Chen, and Jin Z. Zhang. Optical trapping and light-induced agglomeration of gold nanoparticle aggregates. *Physical Review B*, 73(16):165405, 2006.
- [40] J. Tamayo and R. Garcia. Deformation, contact time, and phase contrast in tapping mode scanning force microscopy. *Langmuir*, 12(18):4430–4435, 1996.
- [41] Yu Wang and Lihong V. Wang. Förster resonance energy transfer photoacoustic microscopy. *Journal of Biomedical Optics*, 17(8):0860071–0860075, 2012.
- [42] R. R. Alfano, S. L. Shapiro, and W. Yu. Effect of soap on the fluorescent lifetime and quantum yield of rhodamine 6G in water. *Optics Communications*, 7(3):191–192, 1973.

- [43] V. V. Bryukhanov, S. A. Elistratova, and V. C. Laurinas. Spectral-luminescent properties of deposited rhodamine 6G films. *Journal of Applied Spectroscopy*, 70(3):450–455, 2003.
- [44] Aneta Lewkowicz, Piotr Bojarski, Anna Synak, Beata Grobelna, Irina Akopova, Ignacy Gryczyński, and Leszek Kulak. Concentration-dependent fluorescence properties of rhodamine 6G in titanium dioxide and silicon dioxide nanolayers. *The Journal of Physical Chemistry C*, 116(22):12304–12311, 2012.
- [45] V. Martínez Martínez, F. López Arbeloa, J. Bañuelos Prieto, and I. López Arbeloa. Characterization of rhodamine 6G aggregates intercalated in solid thin films of laponite clay. 1. Absorption spectroscopy. *The Journal of Physical Chemistry B*, 108(52):20030–20037, 2004.
- [46] V. Martínez Martínez, F. López Arbeloa, J. Bañuelos Prieto, and I. López Arbeloa. Characterization of rhodamine 6G aggregates intercalated in solid thin films of laponite clay. 2 fluorescence spectroscopy. *The Journal of Physical Chemistry B*, 109(15):7443–7450, 2005.
- [47] N. Ye Galich and V. A. Petrushchenkov. Numerical modeling of light-induced convection and thermo-optical interaction of a vertical radiation beam with liquids. *Journal of Engineering Physics and Thermophysics*, 66(5):481–489, 1994.
- [48] Klaus Zimmer. Analytical solution of the laser-induced temperature distribution across internal material interfaces. *International Journal of Heat and Mass Transfer*, 52(1):497–503, 2009.
- [49] Sang Hak Lee, Murat Baday, Marco Tjioe, Paul D. Simonson, Ruobing Zhang, En Cai, and Paul R. Selvin. Using fixed fiduciary markers for stage drift correction. *Optics Express*, 20(11):12177–12183, 2012.

초록

빛과 물질의 상호작용은 과학적으로 흥미로운 다양한 현상들을 일으킨다. 그 상호작용에 의해 신호의 변화를 탐지하고 분석하는 분광학은 양자 역학의 발전의 핵심이었을 뿐만 아니라 물리적 화학적 분석에 널리 사용되고 있다. 또한 그 신호를 공간적으로 형상화 하는 현미경 관찰법의 활용은 탐구대상의 구조나 화학적 조성에 대한 직접적 정보를 제공한다. 광학 분광기나 현미경은 살아있는 개체를 훼손하지 않고 실시간으로 관찰할 수 있다는 장점이 있다. 이러한 물리화학적 광학 기술을 활용해 기존에 해결할 수 없었던 생물학적 문제에 접근해보고자 했다.

빛의 고유한 회절 한계로 인해 광학 현미경으로는 아주 가까운 위치에 있는 두 물체를 구분할 수 없다. 회절 한계는 대략 파장의 절반 정도 (가시광선의 경우, 300 nm) 인데, 이는 생분자의 크기 (1-10 nm) 보다 훨씬 크다. 최근 분자의 광물리적 특성을 이용해 회절한계를 극복한 초고분해능 현미경들의 개발로 살아있는 세포 내의 세포 소기관, 단백질, 핵산 등의 생분자를 관찰할 수 있다. 우리는 STED (stimulated emission depletion) 초고분해능 현미경을 이용해 세포 내 류실 tRNA 합성효소의 정확한 위치를 확인할 수 있었다. 류실 tRNA 합성효소는 세포 증식, 단백질 합성 및 자가 영양을 포함한 생리 기능에 영향을 미치는 mechanistic target of rapamycin complex 1 (mTORC1) 이라는 단백질 복합체를 활성화시키는 역할도 한다는 보고가 있었다. 우리는 류신이 있을 때 LRS가 mTORC1 이 생성되는 리소솜으로 이동하는 것을 확인하고, STED 현미경을 사용해 LRS는 리소솜의 내부가 아닌 막에 존재한다는 사실도 밝혔다. 이는 LRS가 류신에 의해 mTORC1 을 활성화시킨다는 직접적인 이미지 증거로 류실 tRNA 합성 효소의 새로운 역할을 초고분해능 이미지로 확인했다.

단분자 형광 분광학은 형광 분자 각각의 물리화학적 현상을 관찰하는 방법으로 여러 분자를 동시에 관찰할 때는 평균에 가려져 볼 수 없었던 단일 분자의 거동을

관찰할 수 있다. 특히 생체 분자는 환경에 따라 균일하지 않은 상태로 존재하기 때문에 각각의 상태를 확인하기 위해서는 단분자를 관찰할 필요가 있다. 단분자 형광 분광학으로 단일 가닥 DNA 의 유연한 구조를 밝혔다. 단일 가닥 DNA 의 구조에 대한 이해는 세포의 유전 과정을 해석하는데 결정적이지만, 나노 미터 길이에서의 동적 변화 구조를 측정하는 것은 실험적으로 어려웠다. 교차 레이저 여기법을 적용한 단분자 형광 공명 에너지 전달(ALEX-FRET) 분광학을 이용해 단일 가닥 DNA의 구부러지는 정도를 확인했다. 다양한 길이의 단일 가닥 돌출부가 있는 이중 가닥 DNA 시스템을 설계하고, DNA의 특정 위치에 있는 두 형광단 사이의 형광 공명 에너지 전달 효율(FRET efficiency)을 측정해 단일 가닥 DNA의 유연성을 결정했다. 지속 길이보다 짧은 세 개 염기 서열을 가진 단일 가닥 DNA가 구부러진다는 사실을 발견했다.

공초점 현미경을 기반으로 하는 단분자 분광학에서도 회절 한계로 인해 분자를 하나씩 관찰하기 위해서는 농도를 아주 낮게 (50 pM) 유지해야 한다. 세포 안의 효소같은 생분자들은 그보다 100 배 높은 (5 nM) 수준에서 주로 작동한다. 우리는 STED 현미경법을 단분자 분광학에 적용해 광학 회절 한계보다 약 100 배 작은 부피에서 확산하는 단분자를 관찰했다. 이로써 전형적인 단일 분자 측정 조건보다 약 100배 높은 5 nM 농도에서도 단일 분자 검출이 가능했다. 이중 가닥 DNA 에 두 가지 형광 분자를 표지해 새로운 기술의 실현 가능성을 시연했다. 이 새로운 기술은 생체 내 확산하는 단일 생분자를 직접 관찰할 수 있는 기술로, 다양한 생화학적 문제를 해결하는 역할을 할 것으로 기대한다.

앞서 익히고 개발한 분광학 기술 등을 생분자 뿐 아니라 유기 광전소자에도 적용했다. 특히 전압을 받아 빛을 발생하는 유기 발광 다이오드(OLED)의 열화 과정을 시분해 분광학으로 분석함으로써 열화의 매커니즘을 실시간으로 관찰 및 분석할 수 있었다. 디스플레이의 수준을 넘어, 강한 빛을 내는 조명 등에 OLED를 활용하기 위해서는 짧은 소자 수명이 문제가 된다. 열화 발생 시 주변보다 상대적으로 에너지준위가 낮은 결함(defect)에 갇힌 전하 운반체는 여러 경로로 소자의 발광을 저해하는데, 그 중 전하 트랩은 실험적으로 관측이 어렵다. 우리는 시분해

전계발광(transient electroluminescence) 기술에 새로운 분석 방법을 접목해 열화 시 전하 트랩의 증가를 관찰하고, 그로 인한 발광 특성의 변화를 밝혔다. 전압이 들어간 순간부터 처음 빛이 발생할 때까지의 시간(t_0)은 소자가 열화될 때 감소한다. 유기층의 전하 트랩에 갇힌 전하 캐리어는 전극에서 주입된 전하 캐리어보다 먼저 마주치기 때문이다. 발광 수명(t_d)은 점점 증가했는데, 이것은 전하 트랩의 뒤늦은 결합으로 설명이 가능하다. t_0 의 감소와 t_d 의 증가로 전하 트랩의 존재를 확인했으며, 전하 트랩이 발광에 미치는 영향을 알 수 있었다. TREL 측정 기술에 새로운 분광학 분석 방법을 적용해 손쉽게 전하 트랩을 분석할 수 있는 방법을 개발했다. 이는 범용적으로 활용될 수 있는 발광/수광 소자의 실시간 전하 트랩 분석 기술로 소자의 열화 메커니즘 연구 및 새로운 특성 연구에 활용될 수 있다.

OLED 소자가 열화될 때 어느 층이 원인인지 알기 위해서는 화학적 분석이 필요하다. 광학 기술은 다른 화학적 분석 기술과 달리 형광의 세기와 수명 관측을 통해 광화학적 성질 비침습적으로 분석할 수 있다. 그러나 소자 내 유기층의 두께는 수 십 nm로 광학 회절 한계보다 얇아서 공간적으로 각 층을 구분하기 어렵다. 이 문제를 해결하기 위해 각 층을 밴드갭이 다른 물질들로 구성해 소자를 제작하는 방법을 선택했다. 광원은 모든 층을 동시에 여기시키지만 각 층에서 발생하는 빛은 각각 다른 파장을 갖기 때문에 이를 스펙트럼상에서 분리할 수 있다. OLED의 열화과정 동안 세 가지 물질을 광학적으로 분리해서 실시간으로 관측함으로써 TREL 기술의 실현 가능성을 보였다. 이는 분자의 광학적 특성을 분석해 화학적 변화를 알아낼 수 있는 간편한 기술로 다양한 다층 소자 연구에 적용할 수 있다.

주요어: 광물리현상, 초고분해능 현미경법, 단분자 형광 분광학, 시분해 분광학, 아미노아실 tRNA 합성효소, 단일 가닥 DNA, 유기발광 다이오드

학번: 2011-23213